ABSTRACT

EVAPORATING CROSSFLOW SPRAYS IN GAS-SOLID FLOWS

by
Guangliang Liu

Injection of evaporating sprays into gas-solid flows is encountered in many engineering processes such as energy production industry and chemical industry. The phenomenon involves phase change, three-phase interactions, heat and mass transfer. All of these characteristics control the process efficiency, pollutant production and product quality. However, very limited studies are available on the evaporating spray jets in gas-solid flows, especially on the spray evaporation rate within a gas-solid medium. A combined study of experiments and theoretical analysis has been carried out here to investigate the fundamental mechanism of evaporating Crossflow spray jets in gas-solid flows.

In this study, in addition to a laboratory scale circulating fluidized bed to provide a continuous gas-solid flows, a laser/lamp-light assisted visualization and image analysis system and a computer aided temperature measurement system have been developed which enables measurement of spray trajectories and temperature distributions of mixture phases in dilute/dense gas-solid flows. All the experiments have been performed in the circulating fluidized bed with a simple rectangular column, controllable solids load and flow conditions, and well-defined liquid nitrogen sprays. The spray trajectory, spray penetration length, and flow pattern are investigated. The geometric and operating parameters, such as nozzle size, nozzle type, injection angle, jetting velocity, and solids loading are studied in the experiments. The experimental study shows that the loading of solid particles in mainstream can significantly shorten the penetration length and alter the spray structure. It is also shown that the quick evaporation of spray droplets leads to the dilution of solids concentration in the evaporation region as well as the reduction of phase temperatures. In this study, a fundamental parametric model for applications of an evaporating liquid jet into a gas-solid flow, which takes into account the three-phase interactions as well as phase changes. The model is focused on the study of the effects of spray parameters on the mixing characteristics such as spray penetration length, temperature and velocity of each phase, trajectories, and the phase volume fraction distributions. The governing equations are based on the conservation principles of mass, momentum and energy of all three phases. The model predictions have also been found in good agreement with the experimental results.

Droplet evaporation rate is the most important factor to affect the phase interactions of the spray in gas-solid flows. The spray evaporation is dominated by the heat transfer through collisions between droplets and solid particles. Part of this study is focused on the Leidenfrost collisions between evaporating droplets and solid particles, which are involved in many multiphase flow applications, e.g., petroleum refinery, surface coating, and fire quenching. In this study, an analytical model has been developed to describe the Leidenfrost collision between a droplet and a hot solid sphere. The whole collision process, the maximum collision time, the maximum deformation area, and the evaporation rate are simulated. Effects of solid curvature and Weber number on the collision time and droplet evaporation rate are illustrated. Modeling predictions are validated by the available experimental results.

EVAPORATING CROSSFLOW SPRAYS IN GAS-SOLID FLOWS

by

Guangliang Liu

A Dissertation
Submitted to the Faculty of
New Jersey Institute of Technology
in Partial Fulfillment of the Requirements for the Degree of
Doctor of Philosophy in Mechanical Engineering

Department of Mechanical Engineering

January 2003

APPROVAL PAGE

EVAPORATING CROSSFLOW SPRAYS IN GAS-SOLID FLOWS

Guangliang Liu

Dr. Chao Zhu, Dissertation Advisor Date
Assistant Professor of Mechanical Engineering, NJIT

Dr. Robert Pfeffer, Dissertation Co-Advisor Date
Distinguished Professor of Chemical Engineering, NJIT

Dr. Rajesh Dave, Committee Member Date
Professor of Mechanical Engineering, NJIT

Dr. Edward Dreizin, Committee Member Date
Associate Professor of Mechanical Engineering, NJIT

Dr. Teh C. Ho, Committee Member Date
Senior Research Associate, ExxonMobil R&D Corporation, Annandale, NJ

BIOGRAPHICAL SKETCH

Author: Guangliang Liu

Degree: Doctor of Philosophy

Date: January 2003

Undergraduate and Graduate Education:

- Doctor of Philosophy in Mechanical Engineering,
  New Jersey Institute of Technology, Newark, NJ, 2003
- Doctor of Science in Fluid Mechanics,
  Tsinghua University, Beijing, P. R. China, 1999
- Master of Engineering in Vibration, Impact and Noise,
  Xian Jiaotong University, Xian, P. R. China, 1995
- Bachelor of Engineering in Engineering Mechanics,
  Xian Jiaotong University, Xian, P. R. China, 1992

Major: Mechanical Engineering

Presentations and Publications

Zhu C., Liu G., Wang X. and Fan L.-S., 2002, "A Parametric Model for Evaporating Liquid Jets in Gas-Solid Flow," *International Journal of Multiphase Flow*, **28**, 1479-1495.

Fan L.-S., Lau R., Zhu C., Vuong K., Warsito W., Wang X. and Liu G., 2001, "Evaporative Liquid Jets In Gas-Liquid-Solid Flow System," *Chemical Engineering Science*, **56**, 5871-5891.

Zhu C., Wang X., Liu G. and Fan L.-S., 2001, "A Similarity Model Of Evaporating Liquid Spray Jets in Concurrent Gas-solid Flows," *Powder Technology*, **119**, 292-297.

Zhu C. and Liu G., 2000, "Modeling of Ultrasonic Enhancement on Membrane Distillation", *Journal of Membrane Distillation*, **176**, 31-41.

Zhu C., Liu G. and Wang X., 2002, "Oblique Evaporating Sprays in Gas-Solid Suspensions," *ASME 2002 FED Summer Meeting*, July 14-18, Montreal, Quebec, Canada.

Zhu C., Wang X. and Liu G., 2002, "Numerical Simulation of Coaxial Evaporating Spray in Nozzle Region of Circulating Fluidized Reactor," *ASME 2002 FED Summer Meeting*, July 14-18, Montreal, Quebec, Canada.

Zhu C., Wang X. and Liu G., 2002, "Effect of Particle Loading on Liquid Nitrogen Jet Mixing in a FCC Riser," *CFB7: 7th International Conference on Circulating Fluidized Beds*, May 5-8, Niagara Falls, Canada, 7, 881-888.

Liu G. and Zhu C., 2001, "Droplet-particle Collision over Leidenfrost Temperature," *Proceeding of 2001 AIChE Annual Meeting*, November 4-9, Reno, Nevada, 148k.

Zhu C., Lam K., Chu H.-H., Tang X. and Liu G., 2001, "Direct Measurements and Numerical Computations of Drag Forces of Interacting Spheres in Power-law Fluid Flows", *Proceeding of 2001 AIChE Annual Meeting*, November 4-9, Reno, Nevada.

Zhu C., Liu G. and Wang X., 2001, "Evaporative Cross-flow Jets in Gas-Solid Suspension Flows," *4th International Conference on Multiphase Flow ICMF'2001*, May 27 – June 1, New Orleans, LA, 117.

Zhu C., Wang X. and Liu G., 2000, "Evaporative Liquid Jets in Concurrent Gas-Solid Pipe Flows," *Proceeding of NHTC'00 34th National Heat Transfer Conference*, August 20-22, Pittsburgh, Pennsylvania, 12143.

Liu G., Wang C. and Zhu C., 2000, "Heat and Mass Transfer in Ultrasonic Enhanced Membrane Distillation," *AIChE 2000 Spring National Meeting*, March5~9, Atlanta, GA, 18e.

Wang X., Liu G. and Zhu C., 2000, "Experimental Study of Evaporative Liquid Jets in Vertical Gas-solid Pipe Flows," *AIChE 2000 Spring National Meeting*, March 5-9, Atlanta, GA, 18b.

This dissertation is dedicated to my wife, Haining and my son, William.

ACKNOWLEDGMENT

I wish to express my sincere appreciation to my advisors, Dr. Chao Zhu and Dr. Robert Pfeffer, for their remarkable guidance, constant supervision, friendship and moral support throughout this research. Without their guidance, it would have been impossible to finish this program so smoothly. Special thanks are given to Dr. Teh C. Ho, Dr. Rajesh Dave, Dr. Edward Dreizin, for their active participation in my dissertation committee. I am also thankful to Dr. L.-S. Fan at Ohio State University for his valuable suggestions in this study.

I am grateful to the supports from Graduate Office and Separately Budget Research Program of New Jersey Institute of Technology for RA Scholarships, from New Jersey Commission of Science and Technology (PPRC Program) for Summer RA scholarships, and from ExxonMobil R&D Incorporation and Petroleum Research Fund for the research fund. I appreciate the friendship and cooperation of Dr. Xiaohua Wang and Mr. Tong Lee during this study.

I would like to express my endless gratitude to my parents, Jiashan Liu and Futao Yuan, who have always supported my academic pursuit and helped me in every possible ways. Last, I want to thank my lovely wife, Haining Xu, and my adorable son, William, for their love and encouragement throughout these years.

TABLE OF CONTENTS

TABLE OF CONTENTS
(Continued)

TABLE OF CONTENTS
(Continued)

LIST OF TABLES

LIST OF FIGURES

LIST OF FIGURES
(Continued)

LIST OF FIGURES
(Continued)

LIST OF FIGURES
(Continued)

LIST OF SYMBOLS

Symbols	**Meaning**
a	undisturbed jet radius
A	area
c_d	drag coefficient of a particle or droplet
c_p	thermal capacity
C	heat capacity
C_D	drag coefficient
C_g	permeability correction factor
C_m	partition factor
d	droplet diameter
d_0	initial droplet diameter
d_p	particle diameter
E	energy
f_{dp}	solids-drops collision frequency
h_{fg}	latent heat
k	decay constant
l	perimeter
L	latent heat
$\dot{m}$	mass generation rate
n	number density
Nu	Nusselt number

LIST OF SYMBOLS
(Continued)

Symbols	**Meaning**
N_u^*	effective Nusselt number
p	pressure
Pr	Prandtl number
q	heat flux
R	universal gas constant
r	radial coordinate
Re	Renolds number $[=d_d \rho_g v_{dg}/\mu_g]$
t	time
T	temperature
u	velocity
U	velocity
v	velocity or vapor
We	Weber number $[=\rho_d d_d v_d^2/\sigma]$
x	axial coordinate
Y	species mass fraction

Greeks

α	thermal diffusivity
α	volume fraction
δ	vapor thickness

LIST OF SYMBOLS
(Continued)

Symbols	**Meaning**
χ	radius ratio
η	traverse coordinate in trajectory system
μ	viscosity
θ	centerline trajectory bending angle, angle
ρ	density
σ	surface tension
ξ	axial coordinate in trajectory system
τ	time
Γ	droplet evaporation rate
Subscript	
0	inlet (at x=0) or free stream
c	centerline or axis
d	droplet
e	entrainment/evaporation
g	gas
m	gas-vapor mixture
p	particle
s	solid
∞	ambient

CHAPTER 1

INTRODUCTION

Injection of evaporating liquid sprays into gas-solid flows involves strong three-phase interactions with momentum, heat and mass transfer across phase boundaries. The rapid evaporation of liquid droplets in a gas-solid flow can have significant effects on the gas-solid mixing near the spray nozzle region. Typical effects of evaporating sprays on gas-solid dynamics include the increase of velocity of both gas and solid phases, the dilution of solid concentration, temperature reduction of all phases, and particle agglomeration or clustering. On the other hand, the particle loading in the gas-solid flow will also considerably change the spray structures such as spray evaporation region, evaporation rate, and collision frequency among droplets and solids.

Applications of evaporating crossflow spray jets into gas-solid flows are constantly encountered in chemical processing industry, petroleum industry, power generation industry and other engineering fields. For example, fluidized catalytic cracking (FCC) process for petroleum refinery, condensed mode operation of polyethylene synthesis, and wet scrubbing systems for pollution controls of the suspended particulate as well as the industrial processes of particle nucleation, agglomeration, and coating.

Fluidized catalytic cracking is very important in the production of gasoline. In fact, over 50% of the gasoline that is produced in the United States is produced by catalytic cracking (Ted, 1998). A schematic diagram of a FCC unit is shown in Figure 1.1. In FCC units, crude oil is heated and injected into through the feed nozzle and evaporates immediately. The oil feed and catalyst mixture travel vertically up the reactor riser pipe and into the FCC reactor. The oil feed and catalysts have a contact time of approximately 2 – 4 seconds. The cracking takes place when the oil vapors come into contact with the catalyst and occurs at a reaction temperature of 520 – 540°C (968° – 1004°F). The spray jet structure, catalytic particle concentration, and local temperature distribution are crucial to the determination of efficiency and quality of FCC processes and products.

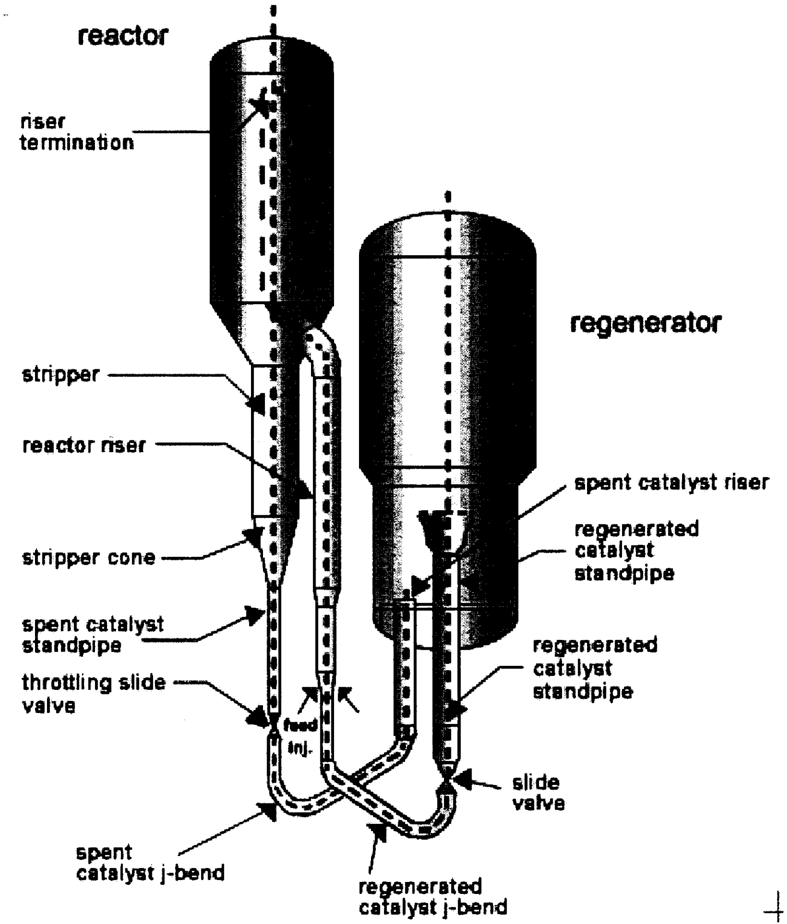

Figure 1.1 Riser cracking FCC unit.
(www.ExxonMobil.com)

Rapid cooling is another consequence of the introduction of spray jets into a gas-solid system. For instance, during a polymerization reaction process illustrated in Figure 1.2, large amount of heat is generated over a short period of time during the reaction process and the operating temperatures are usually maintained close to the sintering temperature of the monomer. Consequently, particle agglomeration, hot spot formation, or clogging of the gas distributor leads to frequent shutdowns and extensive cleaning of the reactor. Operating in such a manner is inefficient, costly, and time consuming. The primary limitation on reaction rate in this unit is the rate at which heat can be removed from the polymerization zone. Hence, injection of an evaporating liquid (monomer or inert liquid hydrocarbon) with a boiling point lower than the operating temperature becomes a common practice to quickly relieve the excess heat. Consequently, the polymerization reactor is cooled significantly as the evaporating fluid absorbs energy to account for its latent heat of evaporation.

The sudden expansion of the evaporated liquid results in alteration in both gas and solid dynamics such as phase velocity, solid concentration, and solid agglomeration or clustering. Inversely, the introduction of solid particles represents large heat sinks promoting evaporation and altering liquid-solid interactions. The liquid condensation and entrainment within the gas-solid flows further complicates the dynamics into three-phase interaction behavior. Overall, the gas-solid flow behavior is severely inter-affected by these localized liquid jet disturbances, which deserves to be systematically investigated. A thorough review of works published in this field will be presented in Chapter 2.

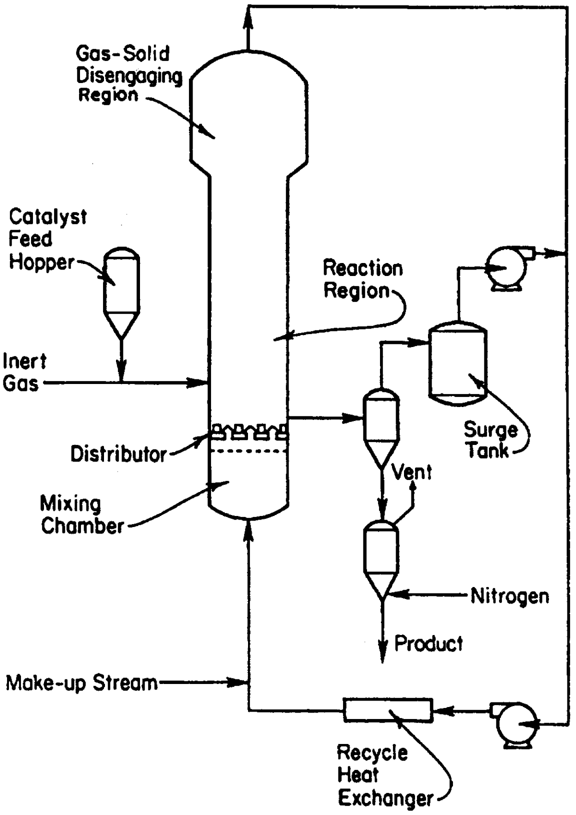

Figure 1.2 Condensed mode of operation for polymerization process. (Jenkins *et al.*, 1986)

Droplet evaporation rate is the most important factor to affect the phase interactions of the spray in gas solid flow. In applications of evaporating spray injected into gas-solid flows, the main heat energy for droplet evaporation comes from collisions between droplets and particles. Hence, the study of droplet-particle collisions is not only necessary but also critical. Evaporation regimes of droplets impinging upon a hot solid surface can be classified, in the increasing order of solid surface temperature, as (1) film evaporation regime, (2) nucleate boiling regime, (3) transition regime, (4) film boiling regime or Leidenfrost regime (Leidenfrost, 1756; Tamura and Tanasawa, 1959), as shown in Figure 1.3. While heat transfer mechanisms and evaporation rates in the film evaporation regime and nucleation regime are relatively well known, the heat transfer mechanisms and parametric characteristics in the Leidenfrost regime are still unclear.

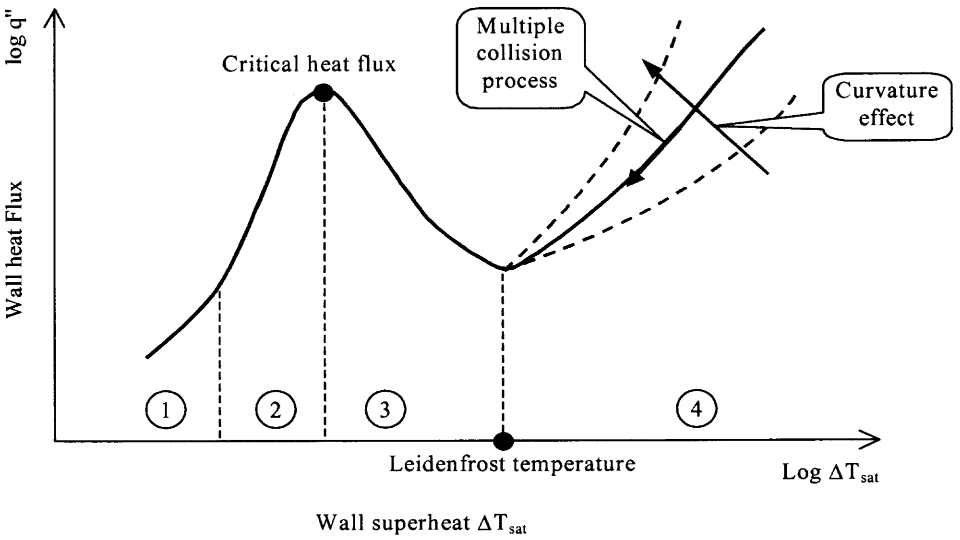

Figure 1.3 Evaporation regimes.

In all evaporation regimes, a maximum of evaporation rate is reached at the end of the nucleate boiling regime, however, the minimum occurs at the Leidenfrost temperature that marks the beginning of the Leidenfrost regime. In the Leidenfrost regime, the evaporating droplet is completely separated from the hot solid surface by a thin layer of vapor, which also violently pushes the droplet for rebounding and even breakup. Droplet-solid collisions in the Leidenfrost regime have many practical applications, such as spray quenching of metal alloys or firewall, spray quenching of melting debris from explosion, and chemical spray into hot catalyst solids. Different from the heat transfer mechanisms in other regimes where the evaporation depends strongly on both the solid surface temperature and impact energy, in the Leidenfrost regime the interaction is governed by the impact energy, whereas the influence of the surface temperature on the interaction phenomenon is negligible (Yao and Cai, 1988). The impact and breakup of a liquid droplet impact on a flat solid surface in the Leidenfrost regime is found to be mainly dependent upon the droplet Weber number (We), which is defined as the ratio of droplet inertia forces to surface tension forces.

$$\mathrm{We} = \frac{\rho u_0^2 d_0}{\sigma} \tag{1.1}$$

where, ρ and σ are the density and surface tension of the liquid, respectively; and u_0 and d_0 are the initial collision velocity and diameter of the droplet, respectively.

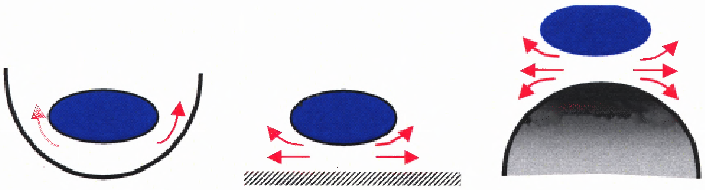
(a) concave (b) flat (c) convex

Figure 1.4 Effects of solid curvature.

However, heat and mass transfer of evaporation by collisions between droplets and solid particles can be significantly different from that between droplets and flat solid surface, due to the effects of particle curvature and thermal capacity. As shown in Figure 1.4, the curvature of a hot solid surface may have a significant effect on the formation and shape of the boiling film, and hence on the heat transfer and droplet evaporation. Successive or multiple collision of droplets with a solid of a limited thermal capacity, in the Leidenfrost regime, will lead to a reduced heat transfer rate, as indicated in Figure 1.3.

The collision characteristics of an evaporating droplet impinging on a solid surface can be extremely complicated if the effects of solid surface curvature and thermal capacity are addressed. Despite a number of reported studies on droplets impinging on a large flat solid surface with an infinitely large thermal capacity, no research has been reported on the effects of solid surface curvature or limited thermal capacity of solids for the Leidenfrost collisions. Detailed knowledge of the fundamental physical phenomena employed droplet impingement on solid surface with limited surface size and thermal capacity is crucial to many industrial applications.

One of the main objectives of this study is to investigate the fundamental characteristics of the evaporating spray jets in gas-solid flows. Both experimental study and theoretical model are performed to study the most unique characteristics of the evaporating sprays. The experimental study in Chapter 3 and Chapter 4 focuses on identification of the effects of operating parameters, such as spray injection angle, solid concentration and jetting or main stream velocity, on the spray jet characteristics. For the convenience of experimental study, a test loop with an operational mode in circulating fluidized bed (CFB) has been set up, in which the liquid nitrogen is used as the jetting liquid and the solids are fluidized catalytic cracking (FCC) particles. A laser/lamplight-assisted visualization system and a thermocouple matrix measurement system are implemented to determine the spray structure in a gas-solid flow. The objective of the theoretical model in Chapter 5 is to develop a general parametric model for applications of an evaporating liquid sprays into a gas-solid flow, which takes into account of the three-phase interactions as well as phase changes. The model is focused on the study the effects of jet parameters on the mixing characteristics such as droplet evaporation length, temperature and velocity of each phases, spray trajectories, and the phase volume fraction distributions. The governing equations are based on the conservation principles of mass, momentum and energy of all three phases.

The study of droplet-particle collision can be very important to understand the phase interaction during multiphase flows, especially in spray jet injecting into gas-solid flows. It is apparent from the literature review in Chapter 2 that the reported studies have only provided insightful fundamental results. They do not yet constitute a comprehensive basis for a closure model even on droplet-wall collision. Therefore, in this study, an analytical model has been developed in Chapter 6 to describe the Leidenfrost collision between a droplet and a hot solid sphere. The whole collision process, the maximum collision time, the maximum deformation area, and the evaporation rate are simulated in this model. Effects of solid curvature and Weber number are illustrated. Modeling predictions are validated by the comparison with available experimental results. Finally, Chapter 7 summaries the major contributions and findings in this study, as well as proposes some new ideas for future studies.

CHAPTER 2

LITERATURE REVIEW

The literature review in this study is divided into two parts: evaporating spray jets in gas-solid flows and evaporating liquid droplet impacting on a hot solid surface. The topic of evaporating spray jet in gas-solid flows is an open area, since very limited researches are both experimentally and theoretically performed in the literature. However, significant progress has been made on either gas-solid jet or spray jet flows. The literature survey of droplet impacting on solid surfaces mainly focus on the topics of droplet-wall collision in Leidenfrost regime.

This chapter will provide a review of some relevant work describing the characteristics of two-phase jets or sprays in single or multiphase flows, as well as droplet hot solid collision. Two-phase jets and sprays will be described in Section 2.1, while droplet hot solid collision will be described in Section 2.2.

2.1 Evaporating Spray Jets in Gas-Solid Flows

Studies on the gas-particle jets in gas flows can be dated back to early 1960s. Many researches have been performed on the effect of particle laden on gas entrainment. Field (1963) performed an extensive study of effects of particles on the entrainment of gas into a free lycopodium/air jets. They found that the presence of particles could increase, decrease, or keep the rate of gas entrainment, depending on the properties of the particle, the gas flow rate, and diameter of the initial jet. Tatterson *et al.* (1987) attributed the particle effect on free jet entrainment to a ratio of particle stopping distance to nozzle diameter. They suggested that, when the ratio is less than 3, the gas entrainment increase due to the presence of particles, while for the ratio between 3 and 65, the entrainment decrease. For ratios over 65, the presence of particles in the jet has no effect on the gas entrainment.

Tsuji *et al.* (1988) performed an experimental study of the air jet laden with coarse solids. They attributed the jet mixing to significant particle diffusion. Subramanian and associates (1982a; 1982b; 1983; 1984a; 1984b; 1985) studied concentric air/sand jet mixing in a gas flow and calculated the jet entrainment from assumed distributions of phase velocity, particle concentration and phase temperature. Measurements on entrainment velocities or velocity distributions of phases of two-phase jets have also been conducted (Memmot & Smoot, 1978; Shinichi Yuu *et al.*, 1978; Levy and Lockwood, 1981; Wall *et al.*, 1982; Filla *et al.*, 1983).

Many experimental studies on other characteristics of gas-particle jet flows have been reported. Edelman *et al.* (1971) used the photographic method to study the particle trajectories when graphite particle of 1-5 μm in diameter were injected into a supersonic flow at a mass-loading ratio (particle over carried gas) up to 0.7. They showed that the centerlines of the particles and of the carrier gas nearly coincide with each other. Rudinger (1975) used a laser-Doppler system to study the flow behaviors of gas-solid jets in a cross-flow. The jet was a mixture of nitrogen and 33-μm glass beads with a mass-loading ratio between 2.3 and 25. The injection velocity of the particles was found to lie between 45% and 65% of the gas velocity at the jet exit. Measurements indicated that the particles are transported by carrier gas to an effective injection point where they separate from the carrier gas and then continue to move under the influence of their inertia and the viscous drag exerted by the crossflow.

Salzman and Schwartz (1978) used 15 μm silicate particles in air jet at mass-loading ratios between 11 and 23 to study the jet trajectory and solid particle distribution. They defined the centerline as the locus of maximum particle concentration, which was determined by isokinetic sampling. Han and Chung (1992a; 1992b) studied a particle-laden gas jet injected into a uniform or non-uniform free stream. They found that the penetration of a two-phase jet is greater than that of a single-phase jet in a crossflow. The penetration of the particles increases with the increasing particle size, particle loading ratio, and the carrier gas-to-free stream velocity ratio at the jet exit. It is also found that when the injection angle is increased, the deviation of the particle trajectory from that of the pure gas becomes larger.

Many studies on evaporating spray jets focused on particle free environment. Peter *et al.* (1994) experimentally investigated the flashing and shattering phenomena of superheated liquid jets injected into a flashing chamber. It was shown that a flashing liquid jet could either shatter or remain in the form of an irregular continuous column after being released from the nozzle. Exponential temperature distributions of the liquid jet along the axial direction were correlated. Chen *et al.* (1994) developed a multifunction, multipurpose PIV system to study the droplet motion of a liquid jet in a high-speed cross-flow environment. Bazile and Stepowski (1994) used dying visualization and image technique to study the atomization and vaporization dynamics of liquid methanol in a burning spray jet. Local vaporization dynamics was observed and reduction in droplet diameter was correlated. Lasheras *et al.* (1998) visualized the breakup and atomization of a round water jet by a high-speed annular air jet. The specific flux of kinetic energy supplied by the gas to the spray jet was found to be the primary parameter determining the secondary break-up and coalescence of droplets in the far field.

Kouremenous *et al.* (1995) developed a model to illustrate of the phase change process of evaporation, in which the fuel spray is divided into three regimes, namely the sheet portion, the break up portion, and the droplet portion. Silverman and Sirignano (1994) studied the effect of multi-droplet interactions on evaporation and droplet motion of a dense spray in a hot gas environment. Gavalses *et al.* (1995) used the phase Doppler method to evaluate the effect of droplet collisions on spray mixing.

Wu *et al.* (1998) investigated the structure of spray plumes from 0.5-mm water jets into a subsonic cross-flow. It was found that the liquid mass distribution depends on the liquid/air momentum flux ratio. More large droplets are distributed toward the upper portion of the spray plume for large liquid/air momentum flux ratios, while for small momentum flux ratios, the large droplets are found in the central portion of the spray plume. They also suggested that the spray evaporation, spray width and evaporation-to-width ratio also increase with the momentum flux ratio.

Zuev and Lepeshinskii (1995) proposed a mathematical model of a gas-droplet non-isothermal multi-component poly-disperse turbulent jet based on a multi-fluid concept by solving Eulerian governing equations. Chen and Pereira (1995, 1996) applied the Eulerian-Lagrangian stochastic method to the dilute evaporating spray in a co-flowing, turbulent heated air stream. The model showed that the droplet mass fluxes persistently accumulate near the centerline region. Sirignano (1999) addressed the spray and droplet behavior in terms of fluid dynamics and transport phenomena with both theoretical and computational aspects. Ibrahim and Marshall (2000) studied the instability of a liquid jet of parabolic velocity profile. The results indicate that the closer the profile to uniform the more pronounced the instability. In the jet atomization regime, increasing Weber number and/or gas to liquid density ratio promote instability.

There is very limited literature (Gu, 1995; Skouby, 1998; Newton, 1998; Warsito and Fan, 2001) reported on evaporating liquid spray in gas-solid flows. In an attempt to simulate the hydrodynamic and heat transfer characteristics of a riser reactor, Gu (1995) modeled the evaporation rate of liquid nitrogen spray in the riser. However, due to the underestimation of phase-interactions, the estimated evaporation rate is much less than that of experimental results. Skouby (1998) used sampling probe measurements to investigate the effect of nozzle characteristics on the flow mixing in a preliminary industry-scaled study of liquid nitrogen spray in FCC risers. They found that the nozzle design is a key point to affect the spray mixing. Newton (1998) illustrated an x-ray imaging technique to visualize the flow patterns of liquid nitrogen spray inside a large-scaled fluidized bed, which showed a significant difference between the spray in the open space and the one in a fluidized bed.

Warsito and Fan (2001) developed an electrical capacitance tomography (ECT) system to capture images of evaporating liquid nitrogen jet into a dense phase gas-solid fluidized bed. Using an image reconstruction algorithm, the cross-sectional images of the multiphase flow system could be obtained from the measured capacitance values. Chang *et al.* (1996, 1998) performed the full field numerical simulation of oil spray in FCC reactors. The hydrodynamic processes of heat transfer, droplet evaporation, and mixing were investigated. However, in his study, the effects of particle-droplet collisions on droplet evaporation were ignored.

Studies on parametric models of jet flows have also been actively pursued. However, most parametric models are restricted to the discussion of single-phase jet characteristics. Extensive reviews on single-phase jets were summarized by Abramovich (1963) and Rajaratnam (1976), respectively. Platten and Keffer (1968) suggested a parametric model on cross-flow jet in single-phase flows. In their model, it was assumed that the momentum of the jet perpendicular to the cross-stream is preserved while the momentum of the jet along the cross-stream is increased by the momentum from the fluid entrainment. Campbell and Schetz (1973) investigated the cross-flow jet mixing of non-isothermal flows and further proposed a trajectory model to account for the effects of drag force, axial pressure gradient, entrainment, and heat losses of the jet flow. D'Souza and Forney (1990) studied the effect of chemical reaction on the mixing of a turbulent jet in a laminar cross-flow. Li *et al.* (1990) proposed a simple analysis to estimate the liquid jet-breakup location in a supersonic flow.

Han and Chung (1992a) developed a parametric model on a premixed gas-solid suspension jet into a cross flow of gas. Effect of the particle-to-gas velocity ratio at jet exit on the jet mixing is investigated. Han and Chung (1992b) further extended their model to investigate the jet mixing of a hot gas-solid jet into a cold cross-flow. Based on the model, effects of the non-uniformity in cross-flow velocity and heat transfer characteristics are revealed. Zhu *et al.* (2001) developed a parametrical model to estimate the droplet evaporation region, considering three phases interactions. The gas-droplet trajectory, particle loading, droplet evaporation, injecting angle, temperature distribution, droplet–particle collision, *etc* were investigated.

While significant progress has been made both in gas-solid jet and spray jet injecting into airflow, no model exists to date which describes the fundamental mechanism of evaporating sprays in gas-solid flows. The key to accurate the modeling of evaporating spray jets in gas-solid flows is the interaction between droplets and solid particles. The following section discusses the development of droplet hot solid surface collision.

2.2 Droplet-Solid Collision

The collision dynamics of a liquid droplet impinging on a hot surface have been investigated extensively and mainly focused on droplet-wall collision. In experimental aspect, many researchers presented a sequence of sharply observable photographs showing the deformation process of liquid droplets impacting on a hot flat surface.

Wachters and Westerling (1966) investigated the deformation process of a saturated water droplet of about 2.3 mm in diameter impinging on a polished gold surface heated to 400°C. It was observed that the impact and breakup of water droplets could be classified into three general categories depending upon the droplet Weber number. In $We \leq 30$ regime, the droplet spreaded out radially upon impingement into a flat disk. After extending itself fully, the liquid regrouped under the action of surface tension forces into a globule and rebounded off the heated surface. In $30 < We < 80$ regime, the droplet underwent similar behavior as the lower Weber number case except that, upon shrinking and rebounding, the droplet split into a large globule and a small spherical satellite droplet. Finally, in *We*≥80 regime, upon impact, the droplet first began to spread out radially into a flat disk, the rim of which broke into several small droplets. The flat disk itself broke up violently into many small droplets. Therefore, the Weber number is the key parameter to determine the hydrodynamic and heat transfer characteristics of droplet-solid collisions. In fact, the critical Weber number, whether or not the droplet breaks up into many small parts on the hot surface, is scattering in the range of 50 - 90 according to the experimental conditions (Bolle and Moureau, 1976; Ueda, 1979; Akao *et al.*, 1980; Hatta *et al.*, 1995).

Using flashing photography, Chandra and Avedisian (1991) measured the time history of an n-heptane droplet impacting a stainless steel surface in the temperature range from 24°C to 250°C keeping the Weber number constant, *We* = 43. It was found that all these impact characteristics were highly temperature dependent within their experimental temperature range. Also, they examined the deformation process of the droplet on a porous ceramic surface (Chandra and Avedisian, 1992). Xiong and Yuen (1991) measured the time history of a heptane droplet impinging on a stainless steel surface in the temperature range from 63°C to 605°C. Anders *et al.* (1993) investigated the rebounding phenomenon of ethanol droplets impacting obliquely on a smooth chromium-plated copper surface at 500°C.

Chen and Hsu (1995) studied the phenomena of transient boiling heat transfer during liquid contact on superheated surfaces. They developed a micro thermocouple probe to detect transient surface temperature with a response time better than 1 ms. It was found that the instantaneous surface heat flux varied by orders of magnitude during the milliseconds of liquid residence at the hot surface. The average heat flux during liquid contact was found to range from 10^5 to 10^7 W/m^2 for water at atmospheric pressure, as wall superheat was varied from 50 to 450°C.

Hatta *et al.* (1997) investigated the collision dynamics of water droplets of 300 - 700 μm in diameter impinging on a hot rough surface heated to 500°C. They found that the droplet configuration is not axially symmetric around the initial impact point even at an early stage immediately after collision and that the irregularity of the droplet configuration is amplified as the droplet deformation proceeds. With increasing Weber number, the irregularity is more remarkable in the later stage and finally the droplet breaks up into some parts. They also found that the critical Weber number to specify whether or not the droplet is disintegrated on the rough surface becomes small compared with the smooth surface case.

Recently, using still and high-speed photographic techniques, Bernardin *et al.* (1997) studied the impact behavior of water droplets on a hot aluminum surface with surface temperature ranging from 100 to 280°C and Weber number of 20, 60, and 220. It was found that the temperature corresponding to the critical heat flux and the Leidenfrost point showed little sensitivity to both droplet velocity and impact frequency.

Karl and Frohn (2000) investigated experimentally the interaction processes of small liquid droplets with hot walls well above the Leidenfrost temperature. The loss of momentum of the droplets, the droplet deformation, and the onset of droplet disintegration were investigated. A minimum impinging angle for droplet disintegration was reported. Below this impinging angle no droplet disintegration is observed.

Wang *et al.* (2000) tried to find the critical temperature of dry impact, which has no direct liquid-solid-contact during the impact. They found that the critical temperature is much lower than the Leidenfrost temperature. Extensive observations of single droplet evaporation on hot solid surface are available in the literature (Pedersen, 1970; Shoji *et al.*, 1984; Inada *et al.*, 1985; Makino and Michiyoshi, 1987; Naber and Farrell, 1993; Wang, 1997).

Droplet deformation areas time dependence as well as the droplet residence time, which is defined as the time elapsed between the droplet's attainment of and detachment from the surface, are crucial to model droplet hydrodynamic and heat transfer behavior. Bolle and Moureau (1976) built a theoretical model showing that the droplet spreading film radius related to contact time on two orders. Makino and Michiyoshi (1984) also investigated the contact period and deformation areas of water droplets. For low velocity water droplets (0.3m/s) with a diameter of 2.54 - 4.50 mm and surface temperature from 150 to 360°C, they found that the droplet spreads out into a thin film before boiling. They also found that the deformation area had a linear relation with the contact time.

Wachters and Westerling (1966) used the first order period of a freely oscillating droplet to describe the residence time. Lee *et al.* (1985) gave indications that the duration of individual liquid contacts in transition boiling was of the order of 10 to 100 ms. Akao *et al.* (1980) and Senda *et al.* (1988) found this relation did not hold well under experimental conditions. Akao *et al.* (1980) presented a film boiling regime correlation for the droplet residence time. Senda *et al.* (1988) showed graphically the experimental residence time for water droplets impinging on a heated surface (150°C $\leq T_w \leq$ 400°C) is about half of the first-order period of a freely oscillating droplet.

Numerical efforts in the collision phenomenon are to address the fluid dynamics of the droplet impingement process. Fujimoto and Hatta (1996) investigated numerically the deformation and rebounding processes of a water droplet on a hot surface above the Leidenfrost temperature in a low Weber number range. They found that the recoiling and rebounding of droplet occur owing to the surface tension effect. Also, the numerical results were found to be in fairly good agreement with the experimental data. However, it is impossible to analyze numerically the droplet deformation process for higher Weber number cases, because the droplet breaks up into small parts on the surface during the deformation. Karl, *et al.* (1996) studied numerically the interaction between liquid droplets and a hot wall for wall temperatures well above the Leidenfrost temperature. Numerical calculations with new simulation codes for two incompressible and non-viscous fluids including surface tension effects are compared with experimental results. The vapor cushion between the droplet and hot wall is simulated with special boundary conditions. Many researchers contributed on the isothermal droplet collision processes (Harlow and Shannon, 1967; Tsurutani *et al.*, 1990; Hatta *et al.*, 1993; Fukai *et al.*, 1993; Hatta *et al.*, 1995).

Very little information has been reported on droplets hitting on hot surfaces with finite dimensions, which are comparable to the sizes of the droplets. A relevant work in this area was performed by Yao *et al.* (1988). They studied the phenomena of droplets impacting on thin rectangular strips, which were heated beyond the Leidenfrost temperature. They showed that when the droplet diameter and the strip thickness were comparable, the impacting phenomena included a combination of splashing and cutting. Recently, Liu *et al.* (1994) performed a numerical study to examine the spreading behavior and consolidation of molted droplets impinging on a waved target surface. They concluded that when the droplet impacted on a waved surface, it spread out laterally and maintained a relatively good adhesive contact with the waved surface. Based on these preliminary studies, it is expected that the geometry and size of the impacted surface would play a significant role in the droplet impacting phenomena.

All of the models mentioned above have only been able to predict the behavior of droplets impinging on a flat hot surface. However, the effects of both solid surface curvature and limited thermal capacity on droplet evaporation rate are very important in multiphase flows. So far, no studies have been conducted in this area.

CHAPTER 3

EXPERIMENTAL STUDY

3.1 Introduction

In the development of fundamental hydrodynamic models of an evaporating spray in gas-solid flows, one of the most crucial steps is the validation of these models with experimental data. Therefore, in addition to a circulating fluidized bed, a laser/lamplight-assisted visualization and image analysis system and a computer aided temperature measurement system have been developed, which enables measurements of spray trajectories and temperature distributions of mixture phases in dilute/dense gas-solid flows. The development and calibration of these systems are discussed in detail here. The visualization system captures the spray trajectory accurately at dilute gas-solid flow conditions, while under denser conditions the temperature matrix measurement system can reasonably determine the spray trajectories. Experiments have been carried out with industrial FCC particles, with known averaged density and size. All the experiments were performed in a laboratory-scaled circulating fluidized bed with a simple rectangular geometry and controllable gas-solid inflow conditions, as well as a liquid nitrogen spray system.

As discussed in Chapter 2, the behavior of horizontal gas jets in 2-D fluidized beds and associated various parametric effects were extensively studied. However, the understanding of jetting behavior, penetration length of liquid spray into 3-D gas-solid flow is very limited. Most current activities in the development of novel investigative techniques for evaporating spray in gas-solid flows focus on the use of tomographic methods to provide cross-sectional and three-dimensional images of the multiphase flow behavior (Skouby, 1998; Newton, 1998). The majority of the work focuses on radiation absorption methods (X-ray absorption tomography) and electrical capacitance methods. However, major disadvantages of these techniques are the poor spatial resolution and/or long scan times. Further the relative high capital investment and radiation hazards do not favour widespread application of these techniques. So far, most authors only reported cross-sectional and three-dimensional images and hardly any information can be found on the temperature distribution and penetration length.

Combined measurements of visualization and temperature distribution in a circulating fluidized bed with well-defined liquid spray system are not yet available. However, for quantitative validation of fundamental hydrodynamic models, this kind of information is required. Thus, in this study, a combined measurement using temperature measurement technique as well as laser/lamplight-assisted visualization has been developed to study spray mixtures behavior near nozzle region in a dilute (optically transparent) circulating fluidized bed. The experimental set-up, which includes the circulating fluidized bed and the liquid nitrogen spray system, the laser/lamplight-assisted visualization techniques and the outline of the temperature measurement, is presented in this Chapter, respectively.

3.2 Circulating Fluidized Bed

The circulating fluidized bed, which is built for establishing a continuous gas-solid flow as well as the determination of the operating parameters such as gas velocity and solid concentration, is described in this section.

3.2.1 Circulating Fluidized Bed Loop

In order to investigate the liquid spray jets in gas-solid flows, a circulating fluidized bed (CFB), as shown in Figure 3.1 and Figure 3.2, was built to simulate the continuous gas-solid flow. The major parts of the CFB include a riser, a cyclone separator, a downcomer, and an induced fan. All of the experiments were carried out in the CFB risers, which are constructed of 11.5 inches wide, 8 feet high, and 1 or 2 inch deep channel made of transparent plastic material. The high collection efficiency cyclone (6″ I.D., PE-06, RSG) was used to separate and collect solid particles from gas-solid flows that come from the CFB riser. As shown in Figure 3.1, the induced fan provides the needed power of the channel flow while a bypass valve adjusts the gas flow rate.

The fluidizing gas is introduced into the system through a stainless steel porous gas distributor located at the bottom of the riser. The three-millimeter thick distributor with an average pore size of 20 micron can provide homogeneous gas distribution over the whole bottom of the bed and protect the leakage of solid particles. The fine particle laden gas from the cyclone exit is further filtered through the vacuum filter of the induced fan before it is discharged to the building ventilation system. Since the pressure inside the loop is kept lower than that of the ambient air, there is no out-leaking particulate pollution.

Feed of solid particles into the riser is crucial in the experiments and needs special precaution, as controllable particle feed rate need to be achieved. A continuous system has been developed to feed a recycled amount particles, see Figure 3.3. The feeding system includes a particle container which collects the particles from the cyclone, a butterfly valve, located under the container, which is used to shut off the supply of particle to downcomer pipes, as well as one part of devices to measure the solid volume fraction, and a ball valve near the feed inlet, which functions as a feed control valve to adjust the particle flow rate. The particles are fed into the riser 15 cm above the distributor and carried upward by the fluidizing gas. The solid particles are, then, separated in the cyclone and fed again into the riser to generate a continuous gas-solid flow. The solid particle used in the fluidized bed is FCC particles with a bulk density of 1480 kg/m^3 and the average particle size of 70 micron, calibrated by AeroSizer, as shown in Figure 3.4.

To prevent electrostatic charging in the fluidized bed, the whole setup is grounded. Moreover, in all regular tests Larostat 519 (dimethylethyl ammonium ethosulfate supported on silica, PPG/Mazer Chemicals, kindly supplied by ExxonMobil) as anti-static agent has been used. Due to the small particle size of the powder, some anti-static agent leaves the solid particle circulation loop. In order to remain the anti-static effect, a small amount of Larostat should be regularly added into the system.

The test section is located at 1.2 meter above the distributor, where a fully developed gas-solid suspension is achieved. An oblique liquid nitrogen spray, which will be discussed in Section 3.3, is introduced in the test region and both the laser/lamplight-assisted visualization to be discussed in Section 3.4 and the temperature measurement to be discussed in Section 3.5 are used to study the spray jet characteristics.

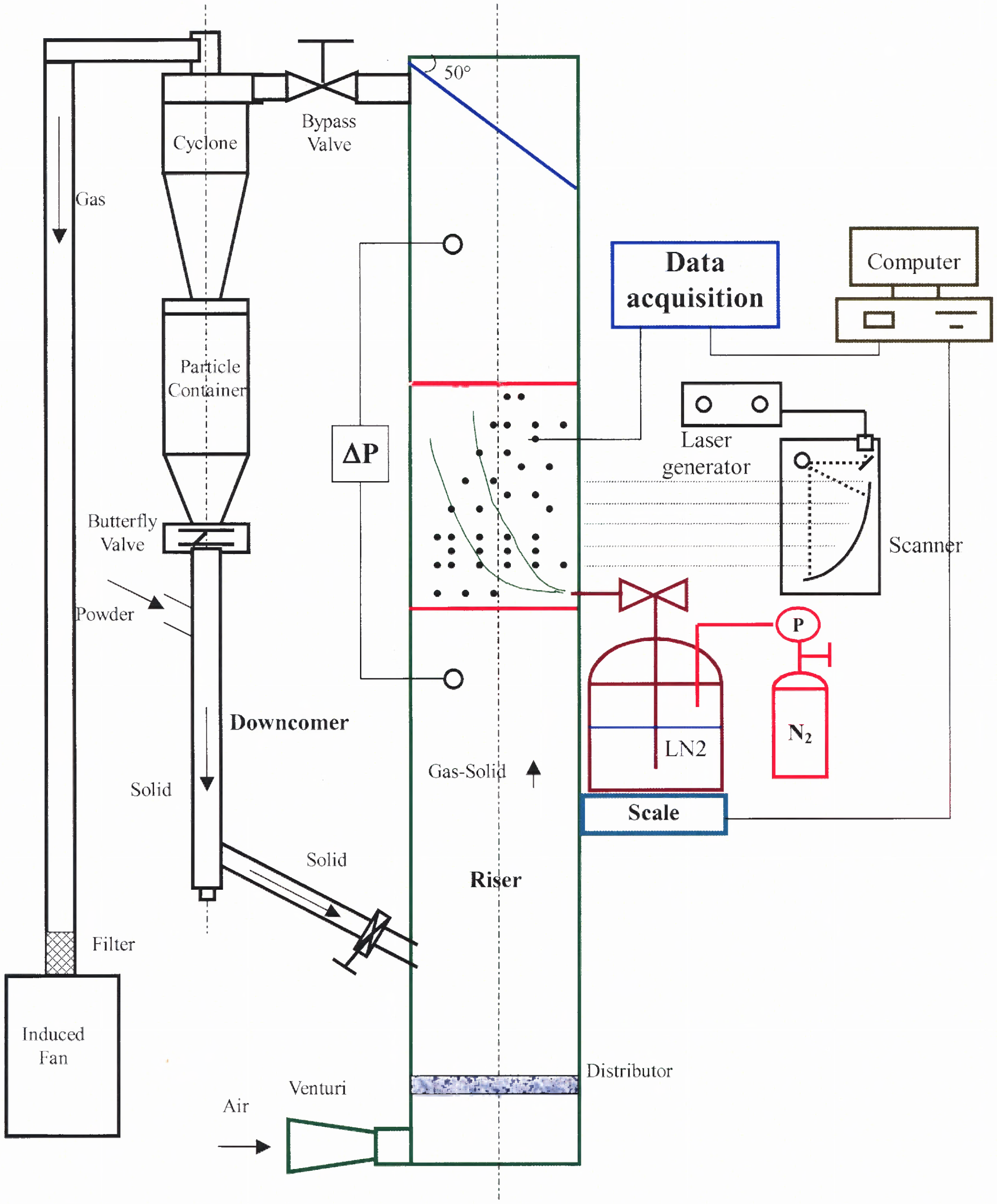

Figure 3.1 Schematic diagram of experimental system.

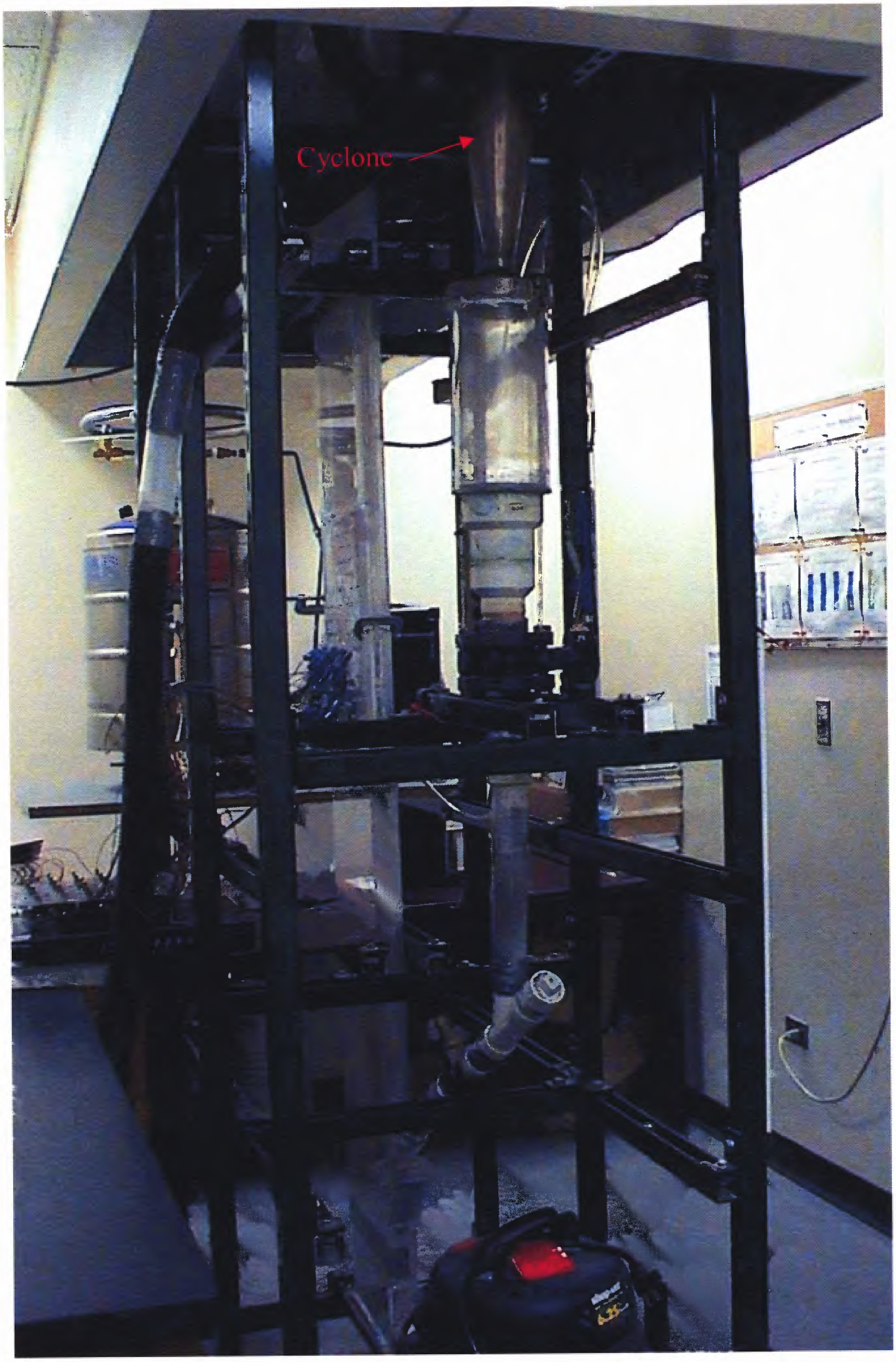

Figure 3.2 Photograph of experimental system.

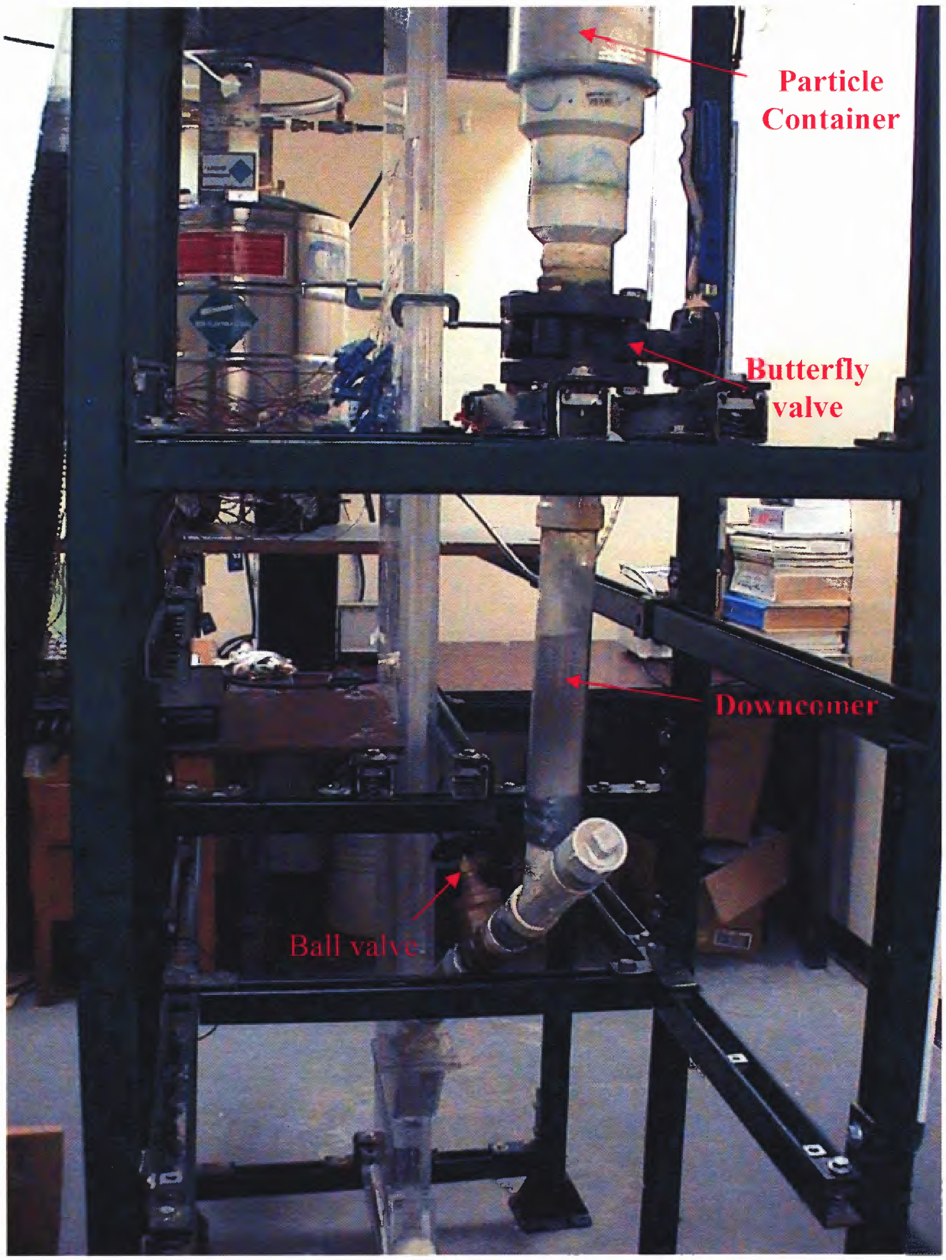

Figure 3.3 Photograph of the solid feeding system.

Figure 3.4 Photograph of AeroSizer system.

3.2.2 Operating Parameters

The key operating parameters in the circulating fluidized bed are the gas velocity and solid concentration in the riser. The gas velocity in the test section is derived from the gas velocity at the inlet of the CFB riser, which is measured by a Ventruri. A U-tube manometer filled with water gives the reading of the pressure difference. Finally, the gas flow rate can be adjusted by the bypass valve. In the experimental study, the maximum gas velocity can reach 1.2 m/s in the test section.

The solid concentration in the test section can be calculated by

$$\alpha_s = \frac{\rho_w \Delta h_w}{\rho_s \Delta h_s} \tag{3.1}$$

where Δh_w is the water reading of a U-tube along the test section; Δh_s represents the distance between the two sampling points in the test section. Thus, the solid volume fraction, α_s, presents the average solid concentration in the test section.

Since the temperature of solid particle will gradually decrease due the cooling effect of liquid nitrogen evaporation during the experiments, a thermocouple is inserted into the downcomer pipe and used to monitor the temperature variation of the solids. Additionally, the gas temperature is measured by another thermocouple installed in the gas inlet.

3.3 Liquid Nitrogen Spray System

Liquid nitrogen spray system is one of the most important subsystems in the experimental setup. There are two kinds of spray systems used in the experimental study. One is a self-controlled (or heat transfer-controlled) spray system, which will be described in Section 3.3.1, while the other is a pressure-controlled spray system to be described in Section 3.3.2. In this section, the liquid nitrogen spray systems and their calibrations with different nozzles will be presented. The calibration of the system includes the determination of the spray mass flow rate, spray jetting velocity, and liquid droplet volumetric fraction under different operation conditions and with different types of nozzles. Four nozzles with different shape and openness, as shown in Table 3.1 and Figure 3.5, have been used in this study. The Flat and Circle-1 nozzles are utilized with the self-controlled spray system, while Circle-2 and Circle-3 with the pressure-controlled spray system.

Table 3.1 List of Nozzles

Nozzle type	Flat	Circle-1	Circle-2	Circle-3
Openness (mm)	5.10×0.47 (L1×L2)	0.6 (d)	1 (d)	1.5 (d)
Length (mm)	150	150	250	250

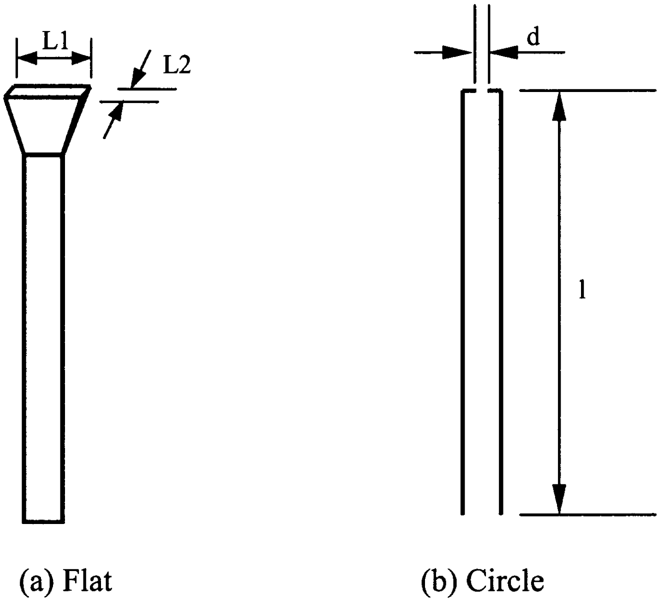

(a) Flat (b) Circle

Figure 3.5 Schematic diagram of nozzle geometry.

3.3.1 Self-controlled Liquid Nitrogen Spray System and Calibration

The self-controlled spray system with a 5-liter dewar (Brymill Cryogenic) is shown in Figure 3.6. The spray mechanism of this system is shown in Figure 3.7. With the aid of partial evaporation via a heat transfer coil, the liquid nitrogen is pressurized in the dewar. Driven by the pressure difference between the dewar and the test section, a liquid nitrogen spray jet can be generated.

Figure 3.6 Self-controlled liquid nitrogen spray system.

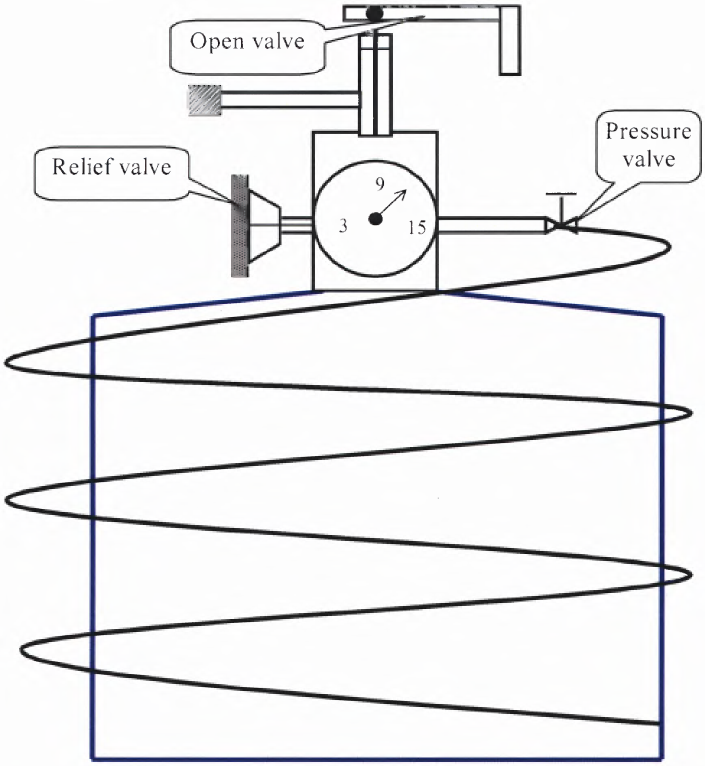

Figure 3.7 Schematic diagram of self-controlled nitrogen spray system.

The spray mass flow rate of different nozzles was directly measured by an electronic balance (SV-30, Acculab) with 30 kg capacity and 0.005 kg readability. For example, Figure 3.8 illustrates the relation between liquid nitrogen weight and time with the flat nozzle. At the beginning of injecting, the mass flow rate is low due to the strong heat transfer on the nozzle tube that causes high vapor volume fraction in the nozzle tube. With the decrease of heat exchange, the nozzle mass flow rate reaches its maximum about 3.2 g/s. However, along with the decrease of the liquid level in the tank, the pressure, which pushes liquid nitrogen out, will gradually decrease. Consequently, the mass flow rate decreases slowly and the lowest rate is about 1.9 g/s. This disadvantage of self-controlled spray system is overcome in the pressure-controlled spray system.

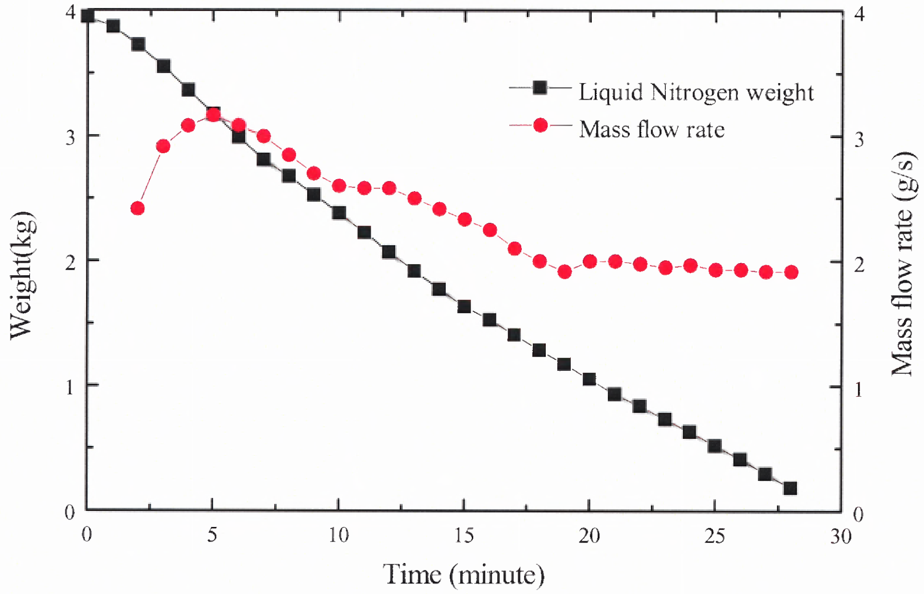

Figure 3.8 Calibration of mass flow rate of flat nozzle.

The droplet velocity at the exit of nozzles has been calibrated using a Laser Doppler Anemometry (LDA) measurement system (1-D FlowLite w/BSA F60, with 10 mW He-Ne Laser, DANTEC). Figure 3.9 gives the histogram of velocity distribution of the flat nozzle with 20,000 sampling points, which indicates that the velocities are Gaussian distributed. The averaged velocity is about 24 m/s with 7.5 m/s in standard deviation for the exit velocity. Similarly, the histogram of the velocity distribution of Circle-1 nozzle is shown in Figure 3.10. The averaged velocity of Circle-1 is 30 m/s with 9.3 m/s in standard deviation.

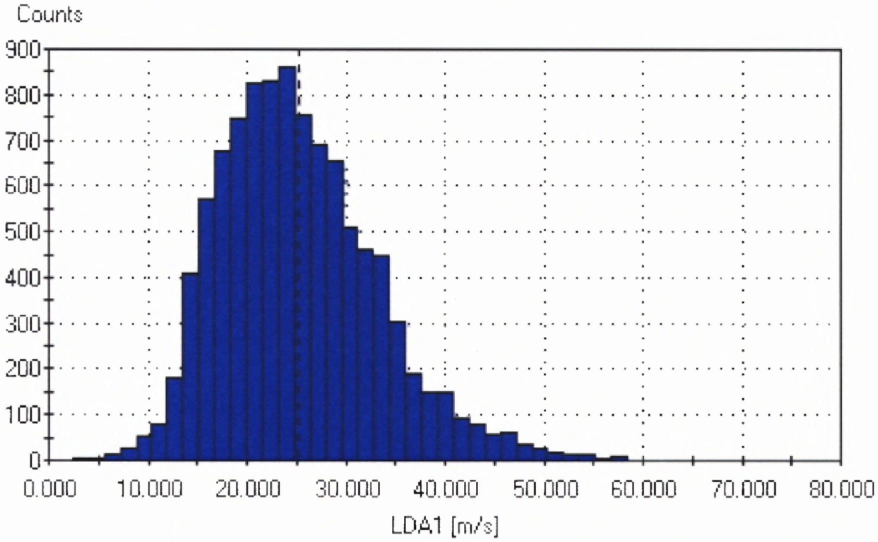

Figure 3.9 Velocity distribution of Flat nozzle.

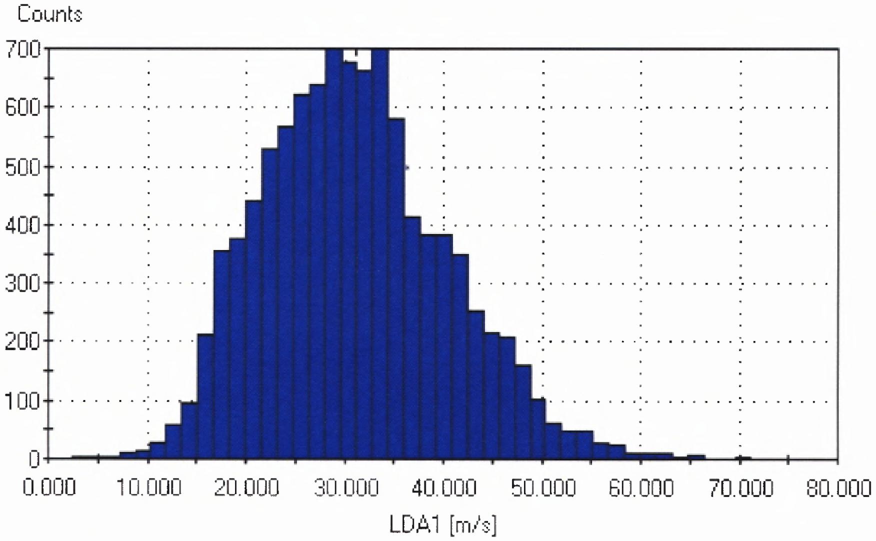

Figure 3.10 Velocity distribution of Circle-1 nozzle.

Under the assumption of no velocity slip between the vapor and droplets at the nozzle exit, the vapor volume fraction in the initial vapor-liquid mixture could be estimated from liquid mass flow rate and droplet velocity by

$$\alpha_g = \frac{1}{\rho_d - \rho_g}(\rho_d - \frac{M_j}{\pi r_j^2 v_d}) \tag{3.2}$$

Finally, The average mass flow rate, mean velocity, standard deviation, and liquid droplet volume fraction of the flat nozzle and Circle-1 nozzle with self-controlled spray system are listed in Table 3.2.

Table 3.2 Calibration Result of Flat and Circle-1 Nozzles

Nozzle	Mass flow rate (g/s)	Mean Velocity (m/s)	σ (m/s)	Liquid volume fraction (%)
Flat	2.33	24	7.5	5
Circle-1	0.67	30	9.3	5.4

3.3.2 Pressure-controlled Spray System

As mentioned in the foregoing section, the disadvantage of self-controlled spray system is the instability of mass flow rate combined with injecting velocity. Moreover, the tank capacity of 5 liters is not large enough to keep running the experiment for a needed time at a higher mass flow rate. Therefore a more accurate spray system, the pressure-controlled spray system with 25 liters capacity, as shown in Figure 3.11, was developed and utilized in most of this study. Comparing with the self-controlled spray system, the stable pressure cylinder tank, as shown in Figure 3.12, can keep a constant pressure in the liquid nitrogen container and results in a stable spray jetting velocity. In addition, the spray mass flow rate can be adjusted by regulating the container pressure.

Figure 3.11 Pressure-controlled nitrogen spray system.

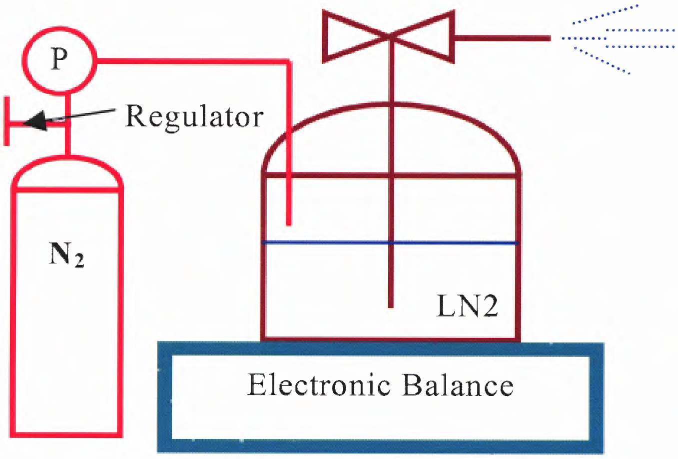

Figure 3.12 Schematic diagram of pressure-controlled spray system.

Figure 3.13 Calibration of pressure-controlled spray system.

Calibration of Circle-2 and Circle-3 nozzles with pressure-controlled spray system was also performed using the Laser Doppler Anemometry (LDA) measurement system. The calibration setup is shown in Figure 3.13. Information on 1-D spray velocities from various nozzles under different pressures is obtained. For example, Figure 3.14 gives the histogram of the velocity distribution of Circle-2 nozzle at different pressures.

The mass flow rate, mean velocity, standard deviation, and liquid volume fraction are listed in Table 3.3.

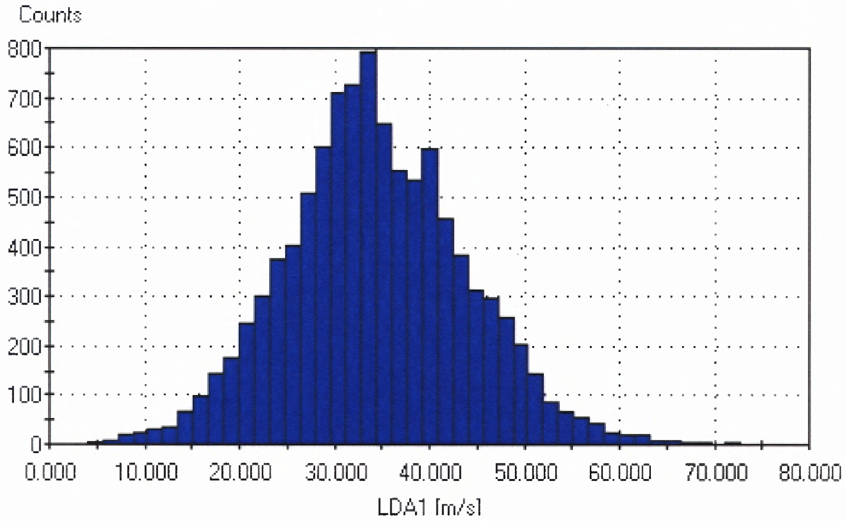

(a) 14 psi

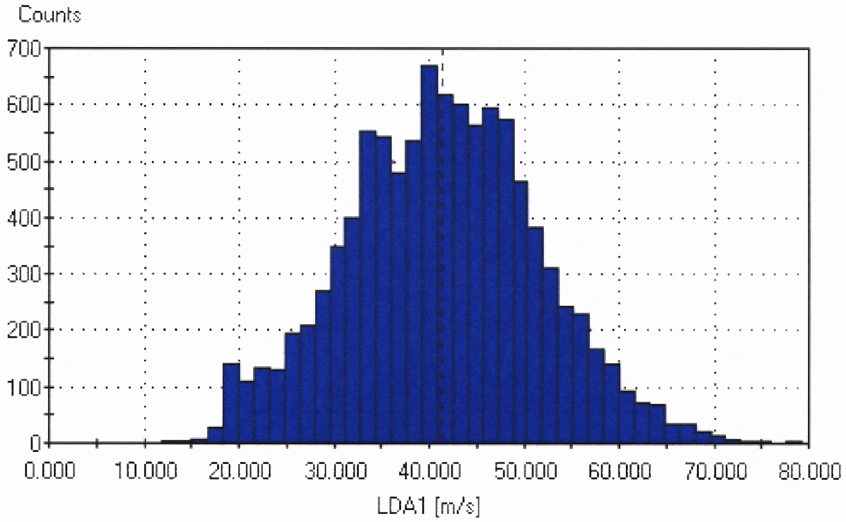

(b) 20 psi

Figure 3.14 Velocity distribution of Circle-2 nozzle.

Table 3.3 Calibration of Circle-2 and Circle-3

Nozzle	Pressure (psi)	Mass flow rate (g/s)	Mean velocity (m/s)	σ (m/s)	Volume fraction
Circle-2	14	1.2	33	4.2	5.7%
	20	3.0	41	6.0	9.9%
Circle-3	14	3.75	17	2.1	8.6%
	20	6.0	32	1.5	7.3%

3.4 Visualization System

The key objective in the experimental study is to determine the spray jet structural characteristics such as spray trajectory and penetration length. Using a laser and/or lamplight assisted visualization system, this information can be obtained by the analysis of the images captured by a CCD camera, which connects to a computer. However, for the dense gas-solid flows the temperature measurement system should be counted on to acquire the needed information.

There are two optical measurement systems have been developed to visualize the spray jet structure in dilute gas solid flows. This section will present the laser-assisted visualization system and the lamplight-assisted visualization system, respectively.

3.4.1 Laser-assisted Visualization System

The laser-assisted visualization is composed of an argon ion laser generator (Reliant 1000M, LaserPhysics) with a 3-watt power, a laser beam scanner (Optical Flow Systems), a CCD camera (Kodak Megaplus ES-310, Kodak), and a computer (Intel 500 MHz Pentium III, Gateway) with image analysis software (XCAP, EPIX Co.) as shown in Figure 3.15. A laser beam is generated by the laser generator, as shown in Figure 3.16, and is sent to the scanner, seeing Figure 3.17, by an optical fiber. Then a 500mm length laser sheet is generated by the scanner and is applied to illustrate the test section. The scanning speed of the scaner can be adjusted from 0.5 ms to 12.7 ms. The CCD camera captures the spray flow pattern and the images are sent to the computer and analyzed by the EPIX digital analysis system.

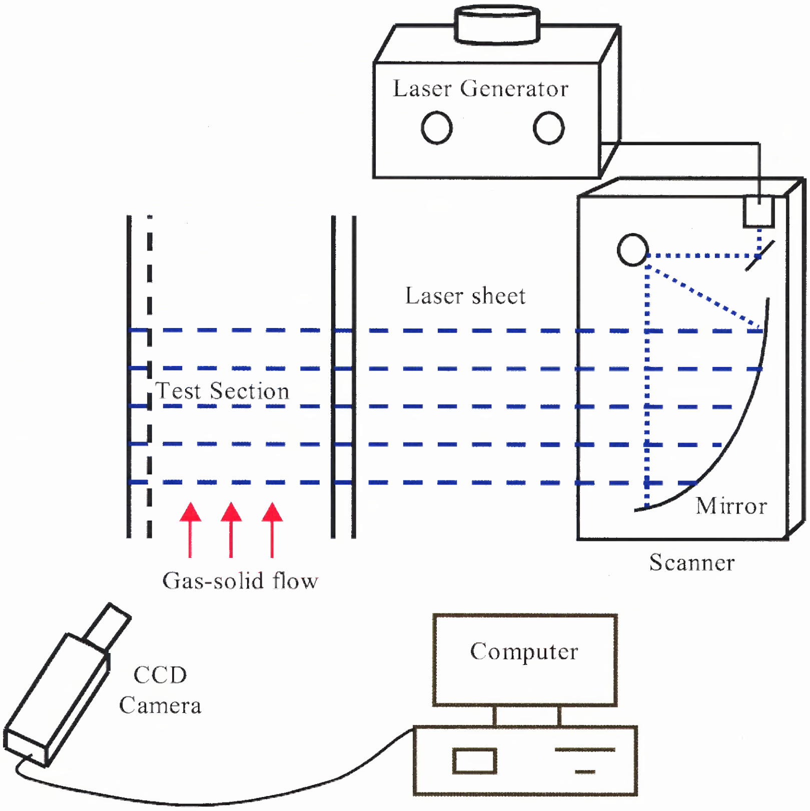

Figure 3.15 Schematic diagram of laser-assisted visualization system.

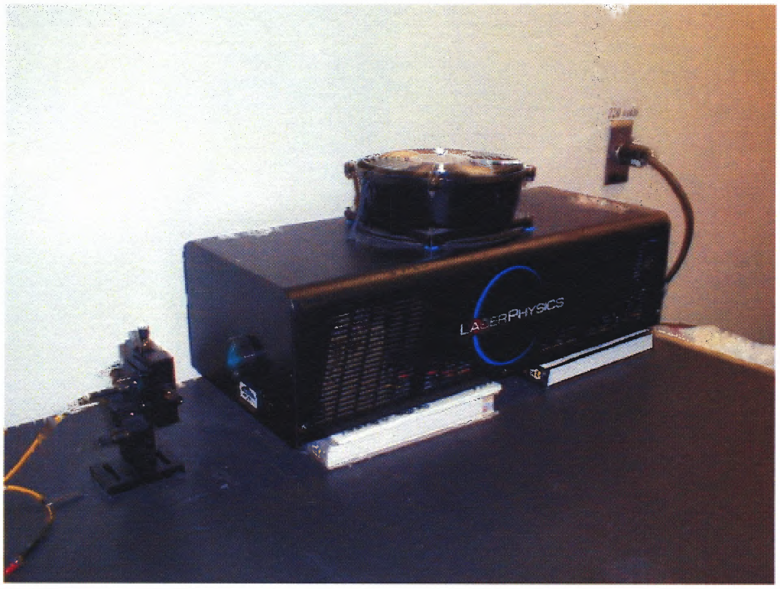

Figure 3.16 Argon Ion laser generator.

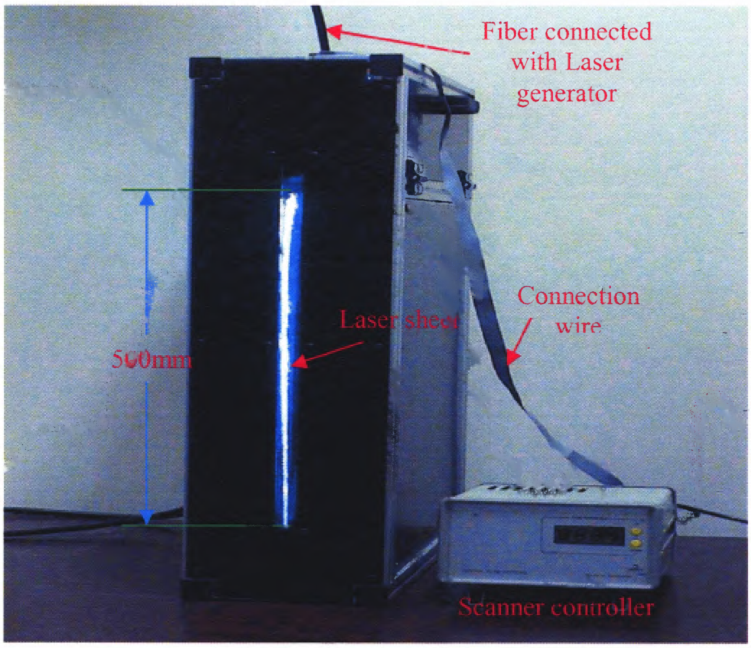

Figure 3.17 500 mm scanning beam box and scanner controller.

The high-speed, real time, and progressive scan digital CCD camera with 648 × 484 pixels can take images at a rate up to 85 frames per second. The exposure time of the camera is from 94 micro-second to 12 milli-second in the continuous mode. By adjusting the camera exposure time and the laser scanning rate, many different imaging modes can be achieved, such as one exposure per frame, or multiple exposures per frame.

Since the test section is too wide, about 11.5 inch, for the laser sheet to penetrate, the laser-assisted visualization system can only illustrate the test section for very dilute gas-solid flows, about 0.1% solid volume fraction. Hence, the other visualization method, lamp-light-assisted system, is developed to visualize the denser gas-solid flows, which will be discussed in the following section.

3.4.2 Lamplight-assisted Visualization System

The lamplight-assisted visualization system is constituted of an Illuminator (150 SX, Illumination Technologies, Inc.) and a Camcorder (Digital ZOOM DCR-TRV730, SONY), as shown in Figure 3.18. There are two strong light point sources with 5 mm diameter in the Illuminator. The illumination zone can be adjusted by moving the two metal beams, as shown in Figure 3.19. This system can get the spray structure on much higher solid volume fraction flows.

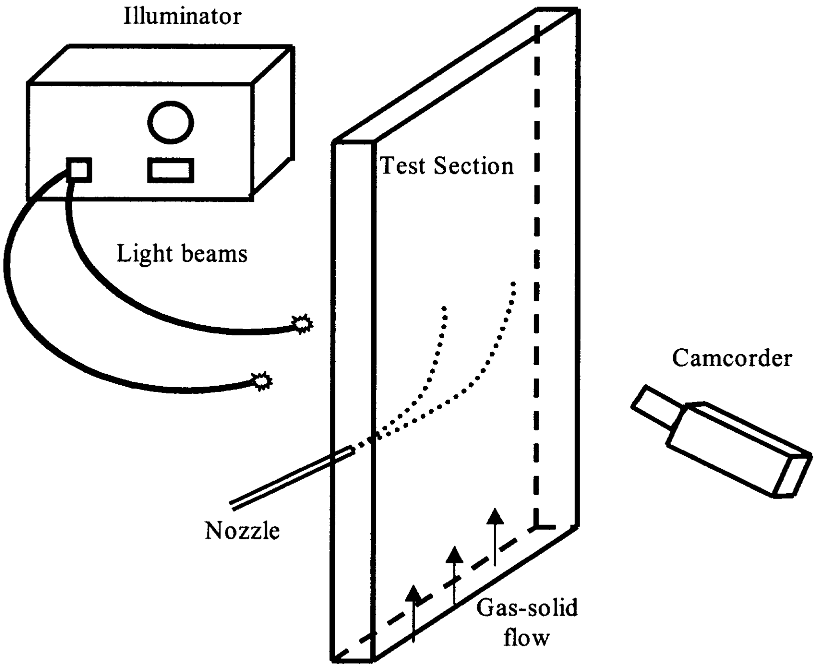

Figure 3.18 Schematic diagram of lamplight-assisted visualization system.

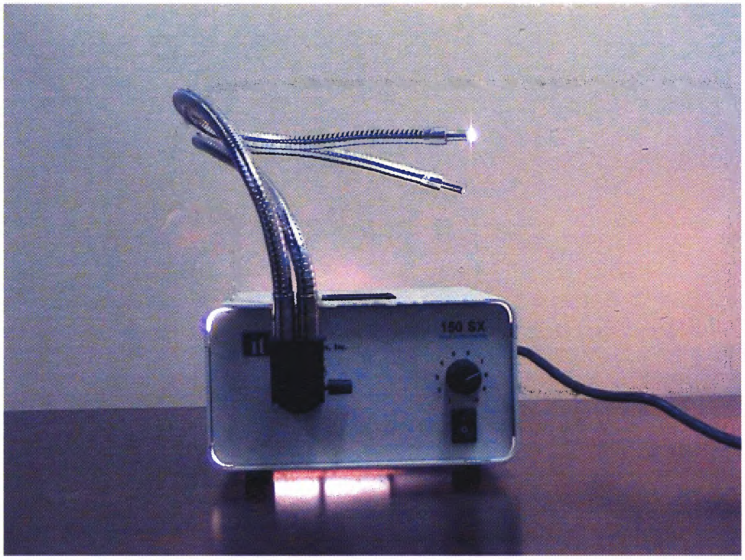

Figure 3.19 Illuminator.

Although the lamplight-assisted visualization system can obtain the spray information at a little higher solid concentration, the illuminated zone is very small. Furthermore, for much denser gas-solid flows, the light from the Illuminator is not strong enough to penetrate the fluidized bed and illuminate the spray. In addition, the local information in the spray region, such as spray expansion width, cannot be obtained by visualization methodology. Therefore the temperature measurement systems have been developed to acquire the spray information at any solid concentrations.

3.5 Temperature Measurement System

Even visulization method can provide some important information of the spray structure in dilute gas-solid flows, it is impossible to get the structure information in dense gas-solid flows. By measuring the temperature distribution in the spray region, the characteristics of spray jet, for instance, spray trajectory, spray penetration, droplet evaporation rate can be obtained directly and/or indirectly. In this section, two different thermocouple measurement systems, 10-thermocouple profile system and 48-thermocouple matrix system, will be introduced respectively.

3.5.1 10-Thermocouple System

For the wider test section (11.5" wideness and 2" thickness), a 10-thermocouple measurement system has been used to measure the temperature profile near nozzle region, as shown in Figure 3.20. The 10-thermocouple probe with 1 cm diameter (Point Profile Probe, PP10-36-T-G-18, Omega Engineering Inc.) that connected to a 10-channel thermometer (MONOGRAM BENCHTOP Meter-10CH, Omega Engineering Inc.) is installed 1" above the nozzle hole for normal injection or 2" above the nozzle hole for oblique injection. Figure 3.21 shows the 10-thermocouple profile probe and the 10-channel thermometer. The distance between two points of 10-thermocouple is 1.25". The distance of the probe in or out of the riser can be adjusted by a Coordinator to obtain more temperature information along the profile.

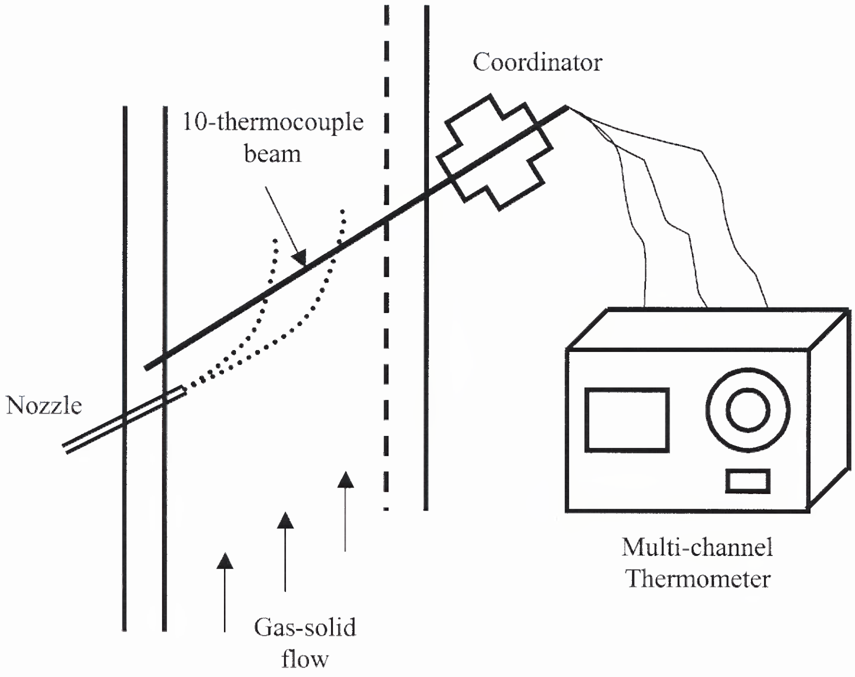

Figure 3.20 10-thermocouple measurement system.

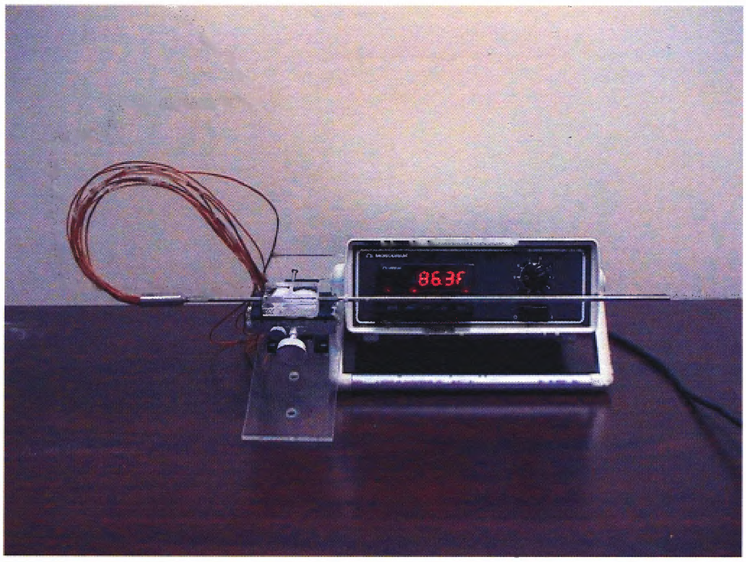

Figure 3.21 10-thermocouple probe and multi-channel thermometer.

3.5.2 48-Thermocouple Matrix System

The 10-thermocouple profile system can only give 1-D temperature distribution of the 3-phase mixture, which is not enough to determine the spray trajectory in the riser. Furthermore, the 1 cm diameter of the probe, which compares to 2″ thickness of the riser, certainly will affect the flow pattern of the mixture phase. In addition, in order to get higher gas velocity in the riser, the thickness of the riser channel has been reduced to only 1″ in many experiments. Hence, a 2-D 48-thermocouple matrix system has been built up to measure a temperature distribution near the spray regime. Figure 3.22 illustrates the mechanism of the measurement system. 48 thermocouples (HTMQSS-020U-6, Omega), which are divided to two groups (each one has 24 thermocouples) and are connected with a 24-switch device (TOGGLE SWITCH, GRAINGER), inserted half inch into the riser and reached to the middle of the riser channel. There are more than 100 small holes (#94) in the plastic plate for different thermocouple distribution styles. The 24-switch device is connected to isolated data acquisition system (OMB-MultiScan-1200, Omega), which has 24 channels and maximum 8000 Hz sampling frequency, and control which group is measured. Pentium III computer with ChartView32 (Omega) is used to connect with the data acquisition system and get the temperatures real time. In the experiments, the sampling time is 50 seconds and the sampling frequency is 4 Hz or 8 Hz. Figure 3.23 shows the 48-thermocouple matrix measurement system. Figure 3.24 shows a typical distribution of thermocouples. The distribution of thermocouples is strongly dependent of the nozzle injection angle. The integrated system of 24-switch device and OMB-MultiScan 1200 is shown in Figure 3.25. In order to prevent thermocouples from picking up static charges, all thermocouples are ungrounded by connecting to a tap water pipe.

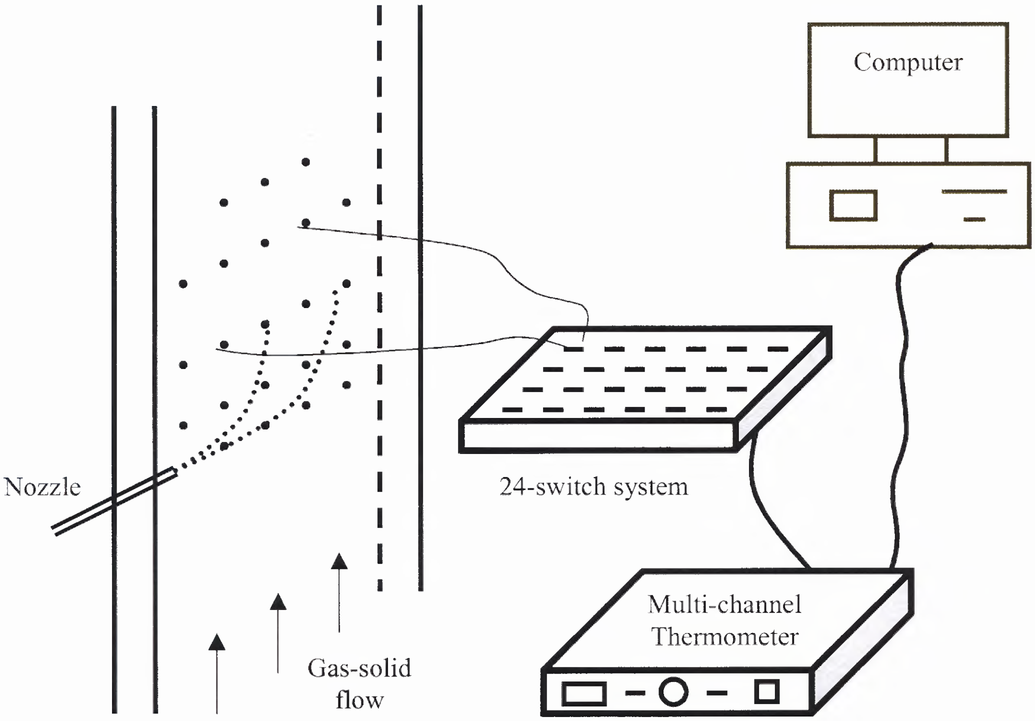

Figure 3.22 48-thermocouple matrix system.

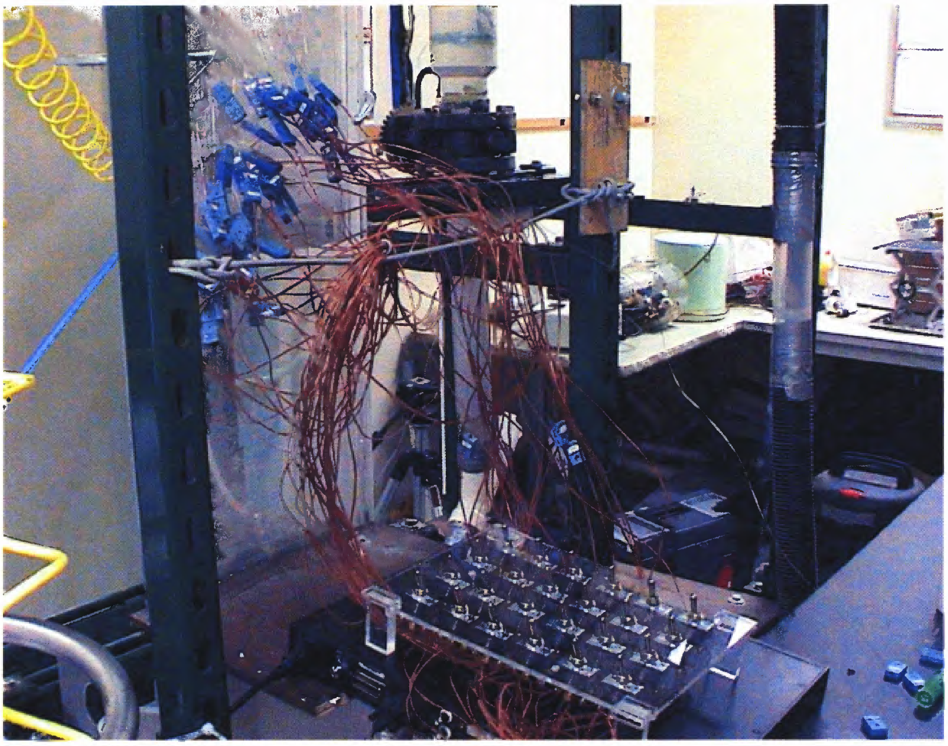

Figure 3.23 Photograph of 48-thermocouple matrix measurement system.

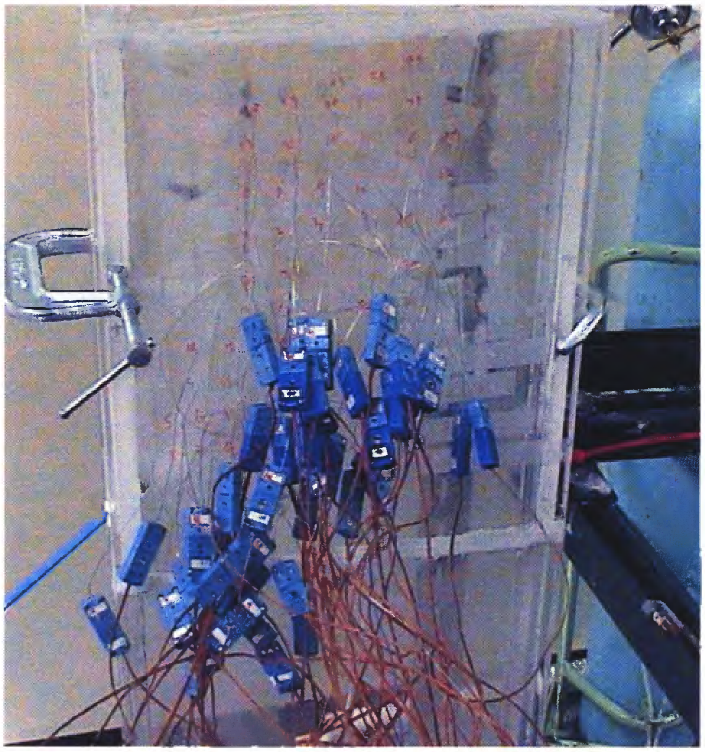

Figure 3.24 Thermocouple distribution.

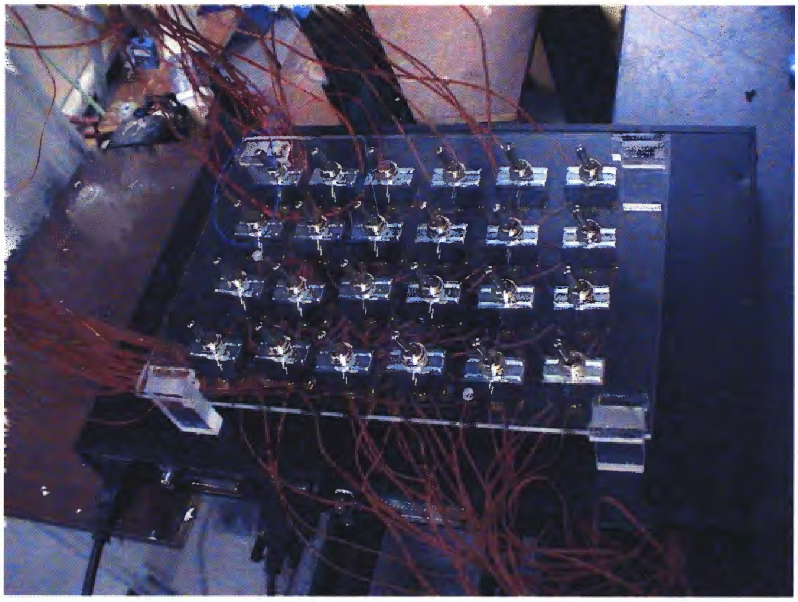

Figure 3.25 24-switch device and OMB-MultiScan 1200 system.

3.6 Experimental Procedure

Two kinds of experimental methods, visualization and temperature measurement, have been used in the experimental study. For a typical case, the experimental procedure is given as follows:

(1) Turn on the Laser Generator and set the required scan frequency in the scanner control.

(2) Set and calibrate the CCD Camera and the EPIX software in the computer.

(3) Set and calibrate the temperature acquisition system and run the ChartView32 software in the computer.

(4) Run the pure gas-phase flow, record the data including the temperature and two U-tubes readings.

(5) Inject the liquid nitrogen into the riser at the deserved setting and wait the spray stable.

(6) Take the spray image and record the data.

(7) Switch the temperature acquisition system to the other 24 thermocouples and record the data.

(8) Turn on the particle control valve and repeat (6), (7) several times for different particles loadings.

(9) Stop spray jetting and keep gas-particle flow for a few minutes.

(10) Stop the run.

Finally, the temperature of the recycling particles may change significantly during the operations. In order to keep the comparability of the results, it is important to maintain the initial temperature of solids as constant as possible.

CHAPTER 4

EXPERIMENTAL RESULTS AND DISCUSSION

4.1 Introduction

For the quantitative validation of fundamental hydrodynamic models of liquid spray jets in gas-solid flows, the experimental setup and methodologies have been developed and discussed in Chapter 3. It should be noted that all of the experimental results could be divided into two parts: one is the visualization result that can give the qualitative validation of the fundamental models; the other is the temperature measurement that can validate the models quantitatively. The presentation of the experimental results in this chapter will focus on the major findings such as the shortening effect of the solid loading and the dilution of the solid concentration. The visualization results are described in Section 4.2, while the temperature measurement is presented in Section 4.3. Some critical comparison between visualization results and temperature measurement is also performed in Section 4.3. Finally, Section 4.4 concludes the most important findings in the experimental study.

4.2 Visualization Results

The visualization images of two kinds of visualization methods, laser-assisted visualization for dilute solids concentration and lamplight-assisted visualization for dense solids concentration, are presented in this section. Effects of solids loading on spray penetration as well as effects of spray on solid concentration are discussed.

4.2.1 Solid Loading Effects on Spray Structure

(a) No solid

(b) 0.05% solid volume fraction

Figure 4.1 Comparison of spray structure (CCD images).

One of the major findings of the experiments is that the solid loading can significantly shorten the spray penetration length. The CCD image comparison of laser-assisted visualization between no solid loading case and very dilute solid loading case, 0.05% solid volume fraction, is shown in Figure 4.1.

Figure 4.1 verified the shortening effect of solid loading on spray structure and penetration length qualitatively. The added solid particles bring huge thermal energy. When the liquid droplets collide with the solid particles, the heat transfer from the particle to the droplets is greater than that from the gas phase to the droplets. Therefore, the evaporation rate of the liquid droplets has been enhanced very much, which shortens the spray penetration length. Even for very dilute cases, the droplet evaporation rate is dominated by the heat transfer through droplet-solid collisions. For this reason, the exact heat transfer from the solid particles to the liquid droplets is very important for developing the macro scale hydrodynamic models of spray jets in gas-solid flows. The collision model between a solid particle and a droplet will be discussed in Chapter 6.

As mentioned before, for a denser solid loading, the lamplight-assisted visualization system was used to illuminate the spray regime and the spray structure was captured by a camcorder. Figure 4.2 shows the images taken at 0.68% and 6.5% solid volume fraction, respectively. From Figure 4.2, it can be concluded that the more solid loading the shorter of the spray penetration length. The dilution effect of solid concentration can also be found in the images taken by the lamplight-assisted visualization. The images shown in Figure 4.3 are the negative color images shown in Figure 4.2.

(a) 0.68% solid volume fraction

(b) 6.5% solid volume fraction

Figure 4.2 Comparison of spray structure (Camcorder images).

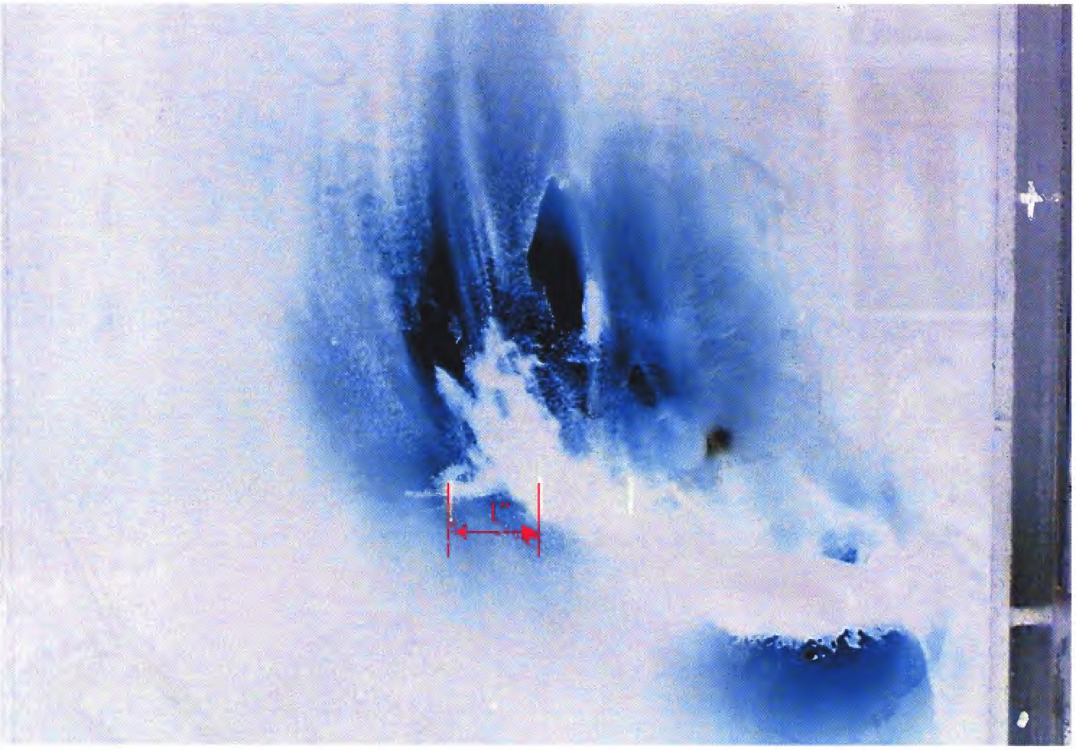

(a) 0.68% solid volume fraction

(b) 6.5% solid volume fraction

Figure 4.3 Comparison of spray structure in negative color (Camcorder images).

In Figure 4.3, the black holes present no or less particle existence in this zone, which confirms the dilution effect of spray jets on solid concentration. It was well known that with the increase of the density of the injecting, the entrainment of the bulk into the jet decreases (Abramovich, 1963), which causes the scarce of solid particles in the spray zone. For the study of spray jets in gas-solid flows, the interaction between the sprays and the gas-solid mixture phase is extremely strong. Both effects should be considered in the study of fundamental hydrodynamic model.

4.2.2 Injection Angle Effect on Spray Structure

The effect of injection angle on the spray structure can be found in Figure 4.4. Figure 4.4 (a) is the Circle-1 nozzle injecting into pure gas flow at about 40 degree, while Figure 4.4 (b) 0.5% solid volume fraction. Figure 4.5 shows the results of injection angle, -30 degree. All experimental results shown in Figure 4.4 and Figure 4.5 illustrate the same influence of angle on the spray penetration length. At different injection angles the entrainment of gas and particle into the spray region is totally different. As the injection angle increases the entrainment of gas-particle mixture decreases and the lowest entrainment is reached in the concurrent mode.

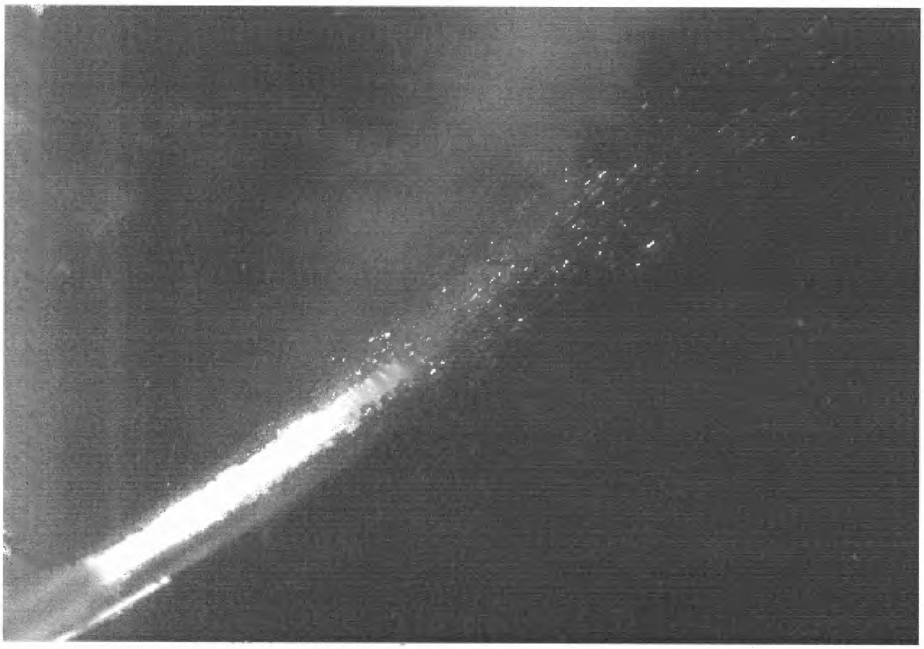

(a) No solid

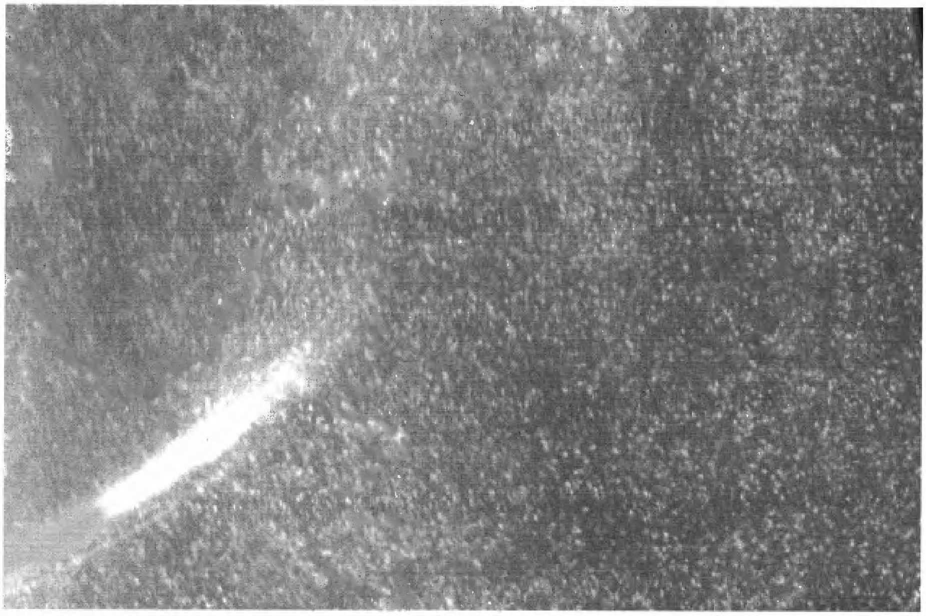

(b) With solid

Figure 4.4 Spray comparison of 30° injection (CCD image).

(a) No solid

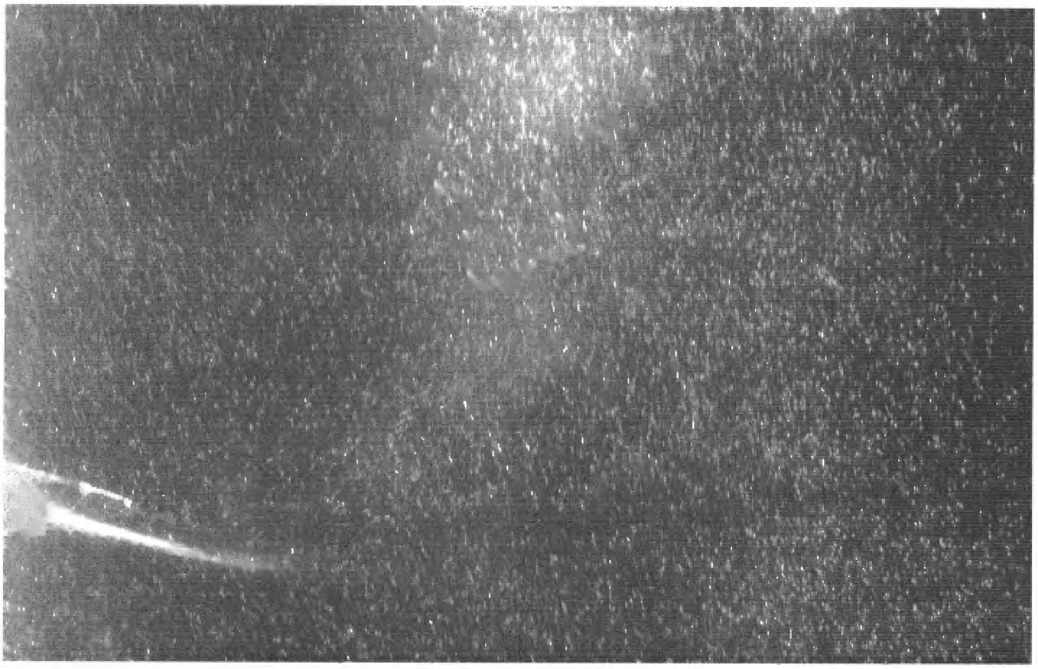

(b) With solid

Figure 4.5 Comparison of spray structure with –30° injection.

4. 3 Temperature Measurement Results

As indicated in Chapter 3, when the solid concentration increases to a limited value, the laser sheet beam cannot penetrate the test section, and the lamplight can only illuminate a very limited zone and give some rough estimation of the spray structure. Therefore, the results of temperature measurement become extremely important in the study of the characteristics of evaporating spray in dense gas-solid flows. In this section, the temperature distributions of two different measurement methods are presented.

4.3.1 10-thermocouple Measurement Results

For the experiments of 10-thermocouple measurement, 22 cases have been performed, and the nozzle type, the injection angle and other operating parameters are shown in Table 4.1.

From the results of temperature measurement, the shortening effect of solids loading is still apparent. For example, Figure 4.6 shows the temperature distribution of cases 1-3 along the riser cross section 1″ above the nozzle. Noted that there are two thermocouples out of function (points 1 & 9). With the increase of solid loading, the minimum temperature point shifts slowly to the spray nozzle since the spray bends more due to the high solid loading. In addition to the temperature measurement, the visualization results are also presented in Figure 4.6, where the blue line represents the no solid condition and the red line presents the low solid loading condition. It should be noted that there is not visualization result for the dense case 3, by the limitation of the visualization. The visualization result is compliant with the temperature measurement result. This consistence further validates the possibility of temperature measurement for predicting the spray structure.

Table 4.1 List of Experimental Cases of 10-Thermocouple Measurement System

Nozzle	Injection Angle	Velocity of air (m/s)	Solid volume fraction %	Case no.
Flat	0°	0.85	0	1
		0.85	0.68	2
		0.85	6.30	3
		0.6	0.68	4
		0.4	6.60	5
		1.5	0	6
		1.4	0.68	7
		1.33	6.50	8
	20°	1.1	0	9
		1.1	0.80	10
		1.1	5.40	11
	36°	0.6	0	12
		0.6	0.68	13
		0.4	6.50	14
Circle-1	0°	0.85	0	15
		0.85	0.68	16
		0.85	6.50	17
		0.56	0.60	18
		0.45	7.00	19
	40°	0.6	0	20
		0.6	0.75	21
		0.4	6.10	22

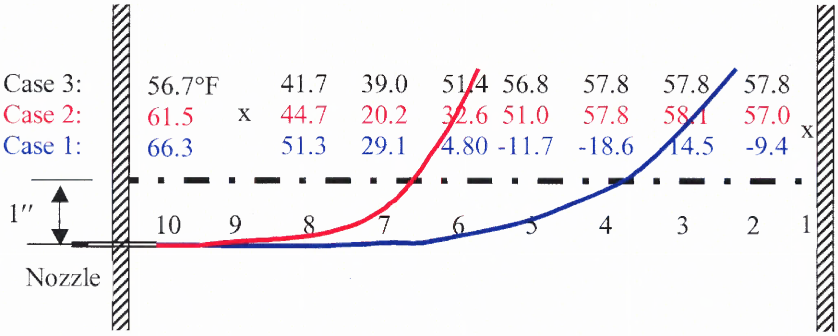

Figure 4.6 Temperature distribution of flat nozzle at 0° injection.

The results of cases 15-17 is shown in Figure 4.7, which illustrates the same effect of solid loadings on the spray structure in different nozzle types.

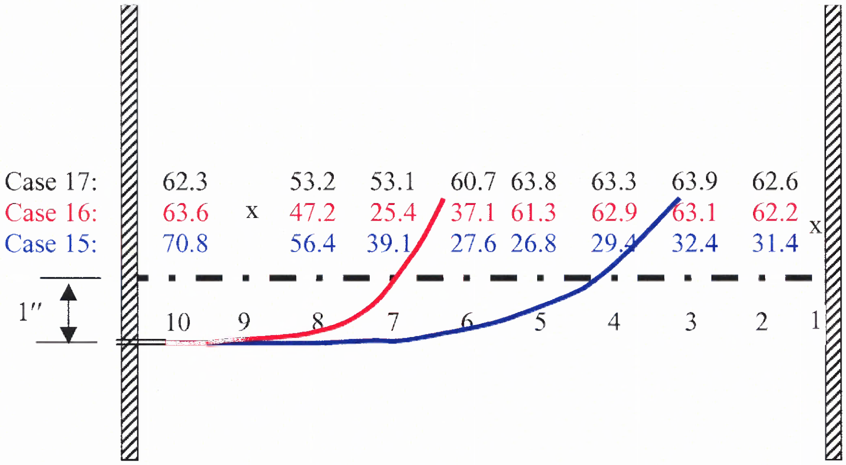

Figure 4.7 Temperature distribution of Circle-1 nozzle at 0° injection.

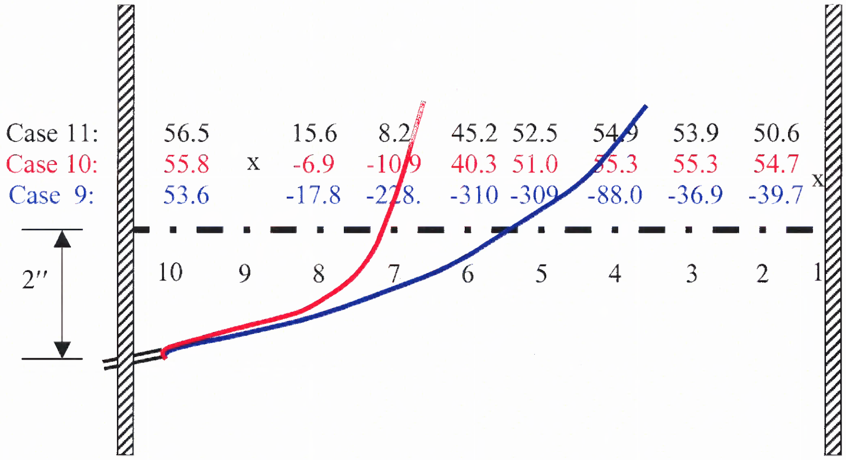

Figure 4.8 Temperature distribution of flat nozzle at 20° injection.

The injection angle effect on the spray structure is shown in Figure 4.8. It is the results of cases 9-11, with injection angle 20° and air velocity 1.1 m/s. At the condition of no solid loading (blue one), the temperature of some points almost reaches the temperature of liquid nitrogen. However, only 0.8% volume fraction of solids (red one) can totally changes the spray structure. The mechanism of solids concentration effect on spray structure will be studied in Chapter 5.

4.3.2 48-thermocouple Matrix Measurement Results

The information of temperature distribution in the spray region is more important than that of only one-section. In this section, the experimental results of 48-thermocouple matrix system are presented in detail. Hundreds of cases of experiments have been carried out in this experimental study. Table 4.2 lists the changes of nozzle, injection angle, and solid volume fraction.

Table 4.2 Lists of Nozzles, Injection Angle, and Solid Volume Fraction

Nozzle type	Injection angle	Solid volume fraction
Circle-1, Circle-2	0°, 25°, 37°, 55°, -30°	0%-3.7%

In order to simplify the explanation, only small part of the experimental results is presented here to emphasize both the effects of solid loading and injection angle on spray evaporation structure, such as spray evaporate rate and spray penetration length. For example, temperature distributions of circle-2 nozzle normal injecting into 0%, 0.5% and 1.3% solid volume fraction in the gas-solid flows at 33 m/s are shown in Figure 4.9, Figure 4.10, and Figure 4.11, respectively. All the temperatures shown in these figures are the averaged value of 200 or 500 measured temperature data.

With the change of spray injection angle, the riser region affected by the spray definitely changes. Therefore, the position of thermocouples also was adjusted according to the injection angle. The results of 20° injection with 0%, 0.5%, 1.3%, 2.5%, and 3.7% solid loading are shown in Appendix A, while these of -30° injection with 0%, 0.5%, 1.3%, and 2.5% solid loading are shown in Appendix B.

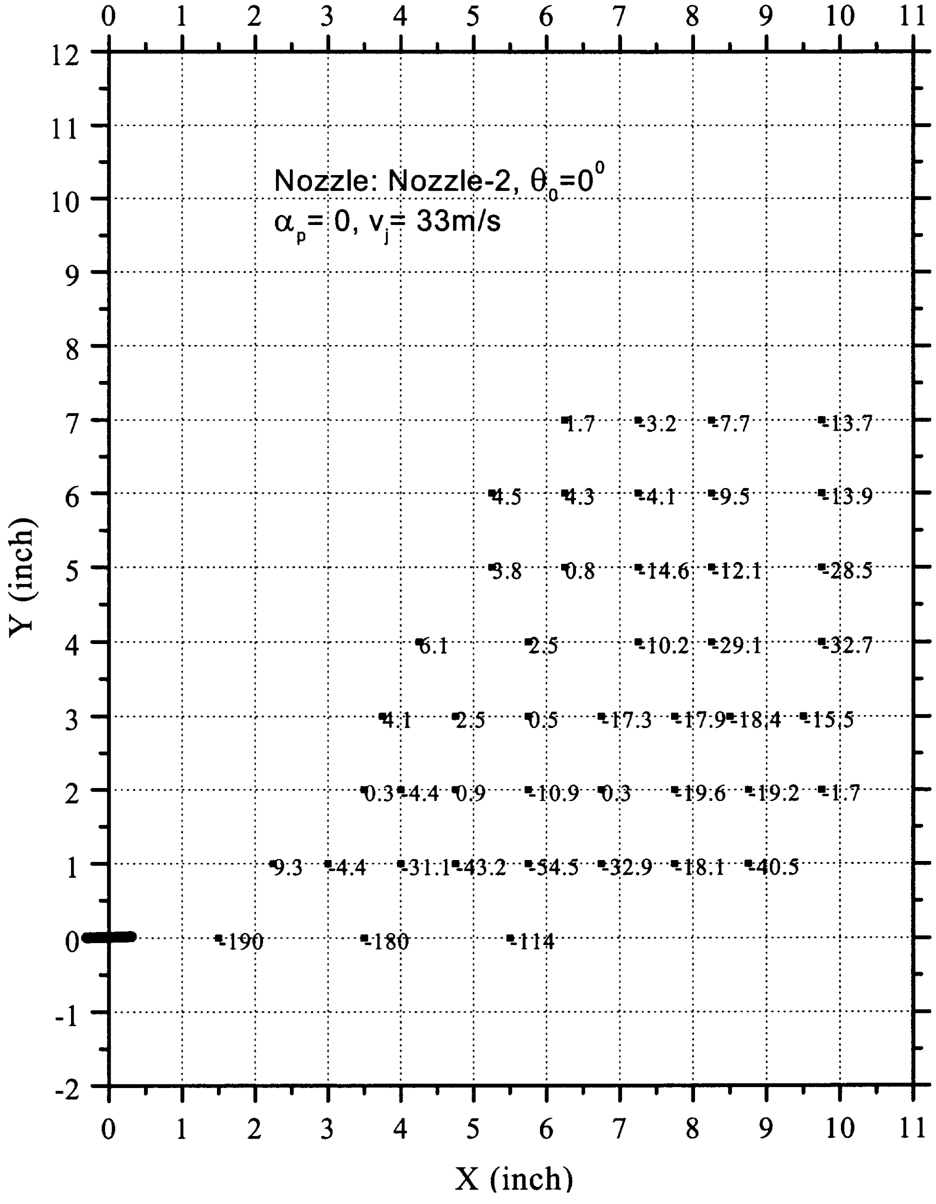

Figure 4.9 Temperature distribution of circle-2 nozzle at 0° and 0% solid volume fraction.

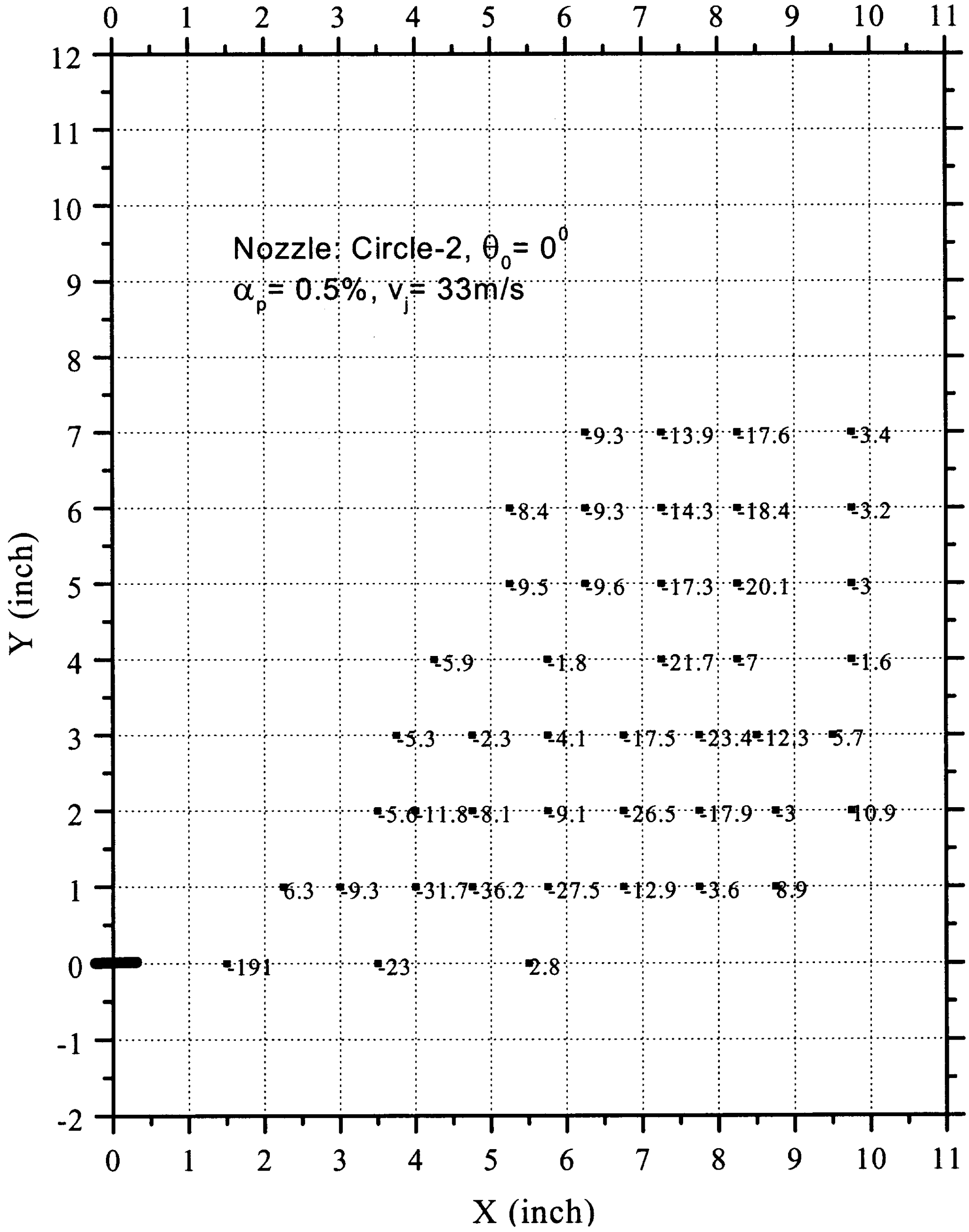

Figure 4.10 Temperature distribution of circle-2 nozzle at 0° and 0.5% solid volume fraction.

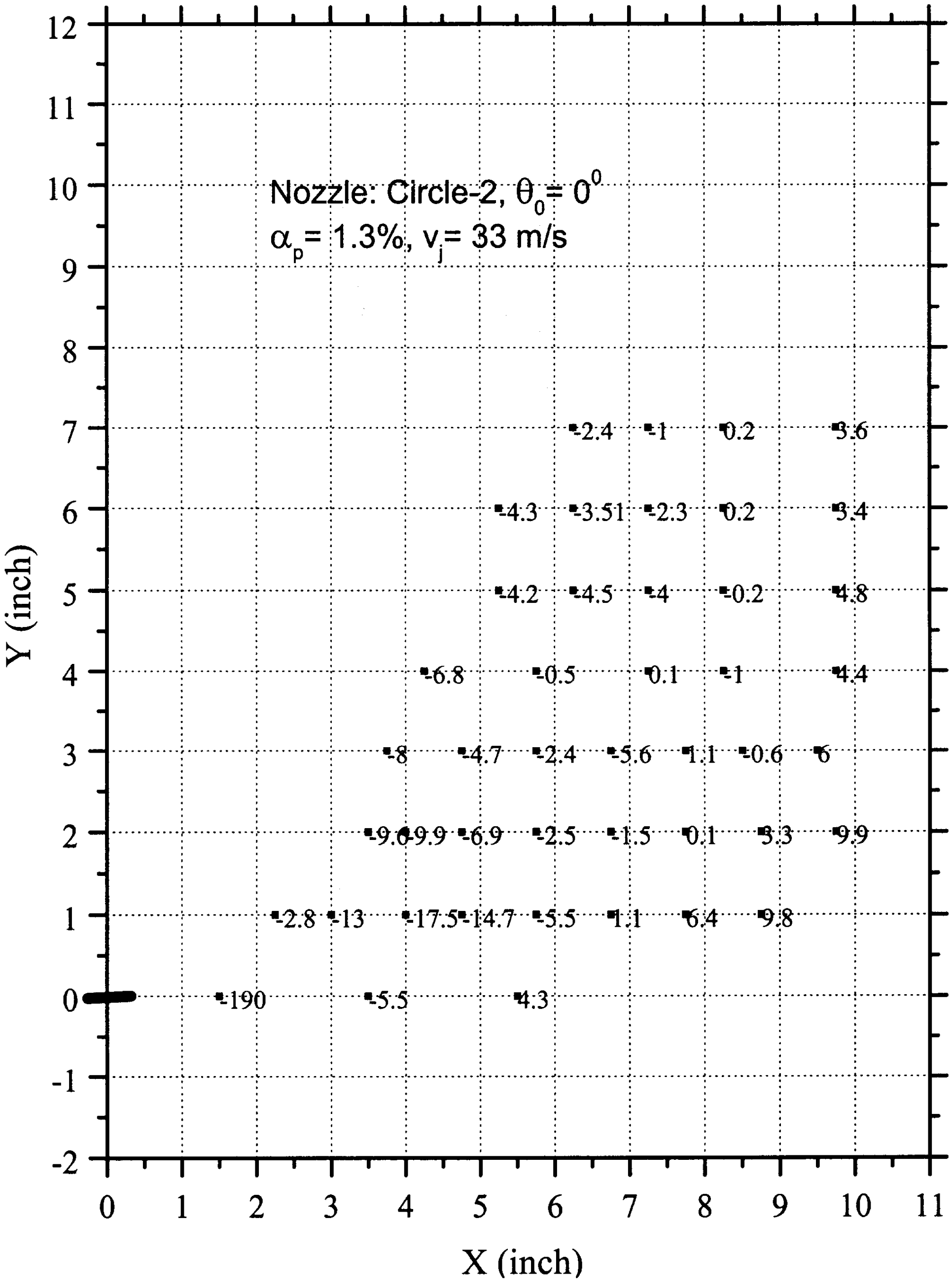

Figure 4.11 Temperature distribution of circle-2 nozzle at 0° and 1.3% solid volume fraction.

4.4 Conclusions

In summary, through visualization and temperature measurements, the major contributions and findings of the experimental studies include:

(1) Successful visualization of the behavior of evaporating spray jets in gas-solid flows.

(2) Successfully measured the temperature distribution of three-phase mixture near the spray region, which is exceptionally important for the validation of the fundamental model of spray jets in gas-solid flows.

(3) Solids loading can significantly affect the hydrodynamics of the spray, which includes the shortening effect on spray penetration length and the speeding effect on spray evaporation rate.

(4) Gas-solid field in the riser also is tremendously affected by the spray injection. The effects include the dilution of solid concentration and the lowing of the temperature of both gas and particle.

(5) The comparison between the visualizations and the temperature measurement gives a good agreement.

CHAPTER 5

PARAMETRIC STUDY OF EVAPORATING SPRAYS IN GAS-SOLID FLOWS

5.1 Introduction

The objective of this chapter is to develop a general parametric model for applications of an evaporating spray jet into a gas-solid flow, which takes into account the phase interactions with phase changes in all three phases. The model is focused on the study of the effects of jet parameters on the mixing characteristics such as droplet penetration length, temperature and velocity of each phase, trajectories, and the phase volume fraction distributions. The governing equations are based on the conservation principles of mass, momentum and energy of all three phases.

As mentioned in Chapter 2, evaporating sprays in gas-solid flows are completely different from a single-phase jet in gas-solid flows or a spray jet in gas flows. First, spray evaporation dominates the flow behavior. Due to the huge difference in densities of liquid and vapor, the evaporation of, say, only 1% (by volume) droplets could produce about 10 times the volume of vapor, which will significantly affect the jet flow behavior that is entirely different from no evaporation cases. Second, the evaporation mechanism of spray in gas-solid flows is quite different from that without solids. Since the thermal capacity of solid particles is much stronger than that of gases, the evaporation of droplets is dominated by the collisions between droplets and particles in sprays in gas-solid flows, which is fully different with the spays in gas flows where the evaporation rate is dominated by convective heat transfer. So far, no analytical models or even experiments have been published in the study of evaporating sprays in gas-solid flows. Therefore, it is regretful that no reported models or experiments could be directly used to validate the theoretical model developed in this chapter.

In this study, it was found that the penetration length is shortened in the presence of particles in a spray jet of any injection angles. The penetration length decreases with the increase of solids loading as well as the increase of injection angle from co-current to counter-current. Comparison of spray penetration length between experimental results discussed in Chapter 4 and modeling predictions is presented in Section 5.3.

5.2 Parametric Modeling Approach

First, consider a case where a cold vapor-droplets jet is mixed with a hot gas-solid suspension flow at an injection angle of θ_0, as shown in Figure 5.1. Major parameters of interest include ambient velocities and temperature of gas and solids, solid particle diameter, ambient volume fraction of solids, ambient pressure, injection velocities of vapor and droplets, injection angle, initial droplet size and droplet volume fraction, initial spray temperature, nozzle diameter, and physical properties of phases, such as specific heat and density.

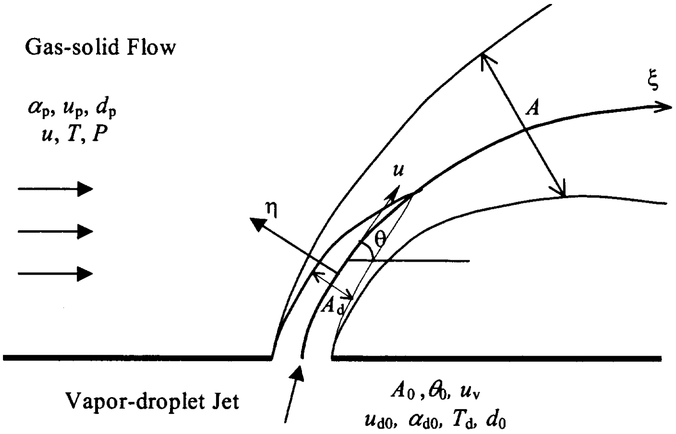

Figure 5.1 Vapor-droplet spray jets in a uniform gas-solid flow.

It is assumed that a thermal equilibrium has been maintained between solids and carrying gas in the ambient gas-solid flow, and an initial thermal equilibrium is reached between vapor and droplets before the injection. In the jet region, the gas-vapor phase is perfectly mixed and behaves like an ideal gas. The centerline trajectory of gas-vapor mixture always coincides with the centerline of the liquid spray, which is true when the sizes of droplets and solids are small and particle loading is light. In addition, all phases are assumed to be symmetric to this centerline trajectory. To further simplify the analysis, the effects of gravity, surface wall, thermal radiation, chemical reaction of phases, as well as size distributions of solids and droplets are excluded. Heat transfer between gas and solids follows the lumped heat capacity model, while heat transfer among solids and droplets occurs only by solids-droplet collisions, where solids are assumed to be trapped inside droplets upon collision.

5.2.1 Differential-Integral Governing Equations

Governing equations of the flow mixing involves dynamic interactions among gas-solid-liquid three phases via the strong coupling of momentum, heat and mass transfer. The phase trajectory and mixing characteristics in the spray region can be readily described using the deterministic Lagrangian trajectory approach in a coordinate system (ξ, η) attached to the centerline of the jet, as shown in Figure 5.1. All phases are assumed to be moving along the ξ direction only within the spray mixing region while the ambient gas and solids are engulfed into the mixing stream by jet entrainment. The spray mixing region is bent due to the convective as well as the collision momentum transfer from flowing round gas-solid flow.

Based on the mass, momentum, and energy balance over a control volume in the (ξ, η) coordinates, as shown in Figure 5.2, general governing equations of each phase can be constructed in differential-integral forms. It is noted that, due to the assumption of the identical flow centerline of each phase in the mixing region, only one momentum equation in the η direction is independent. The most representative η-momentum equation should be selected from the phase whose inertia effect is the minimum among the three phases. Hence, in the following, the η-momentum equation of gas-vapor mixture is used to define the bending of the centerline.

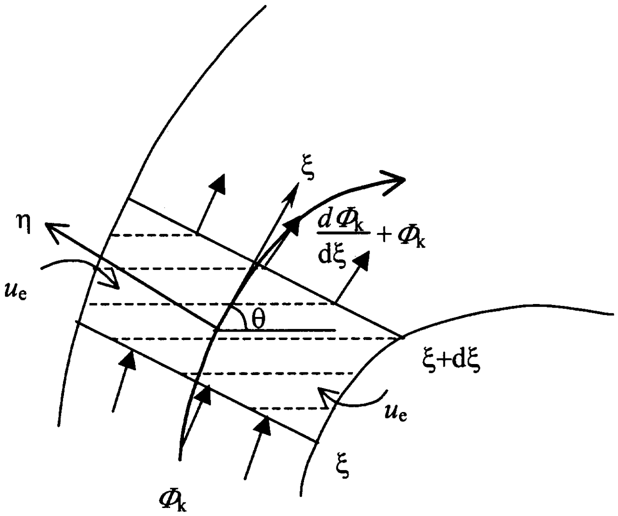

Figure 5.2 Schematic diagram of control volume.

(1) Gas-vapor mixture phase

The continuity equation is derived based on a mass balance among the increased rate of mass flow along ξ, gas entrainment rate across the jet boundary, and vapor generation rate by droplet evaporation, which yields

$$\frac{d}{d\xi}\left[\int_A \rho_m u dA\right] = \alpha_\infty \rho_\infty u_e \ell + \int_{A_d} n_d \dot{m}_e dA \tag{5.1}$$

where the first term on the right is the contribution of entrainment and ρ_m and ρ_∞ are the density of gas-vapor mixture phase and density of ambient gas, respectively; u is the velocity of gas-vapor mixture phase while u_e is the gas entrainment velocity; A is the cross-sectional area of gas-vapor spray; α_∞ is the volume fraction of ambient gas; l is the spray perimeter; n_d denotes the droplet number density; and $\dot{m}_e$ stands for the mass generation rate per droplet.

The ξ-component momentum equation is obtained based on a ξ-component momentum balance among the increase rate of momentum flow, momentum entrainment carried by the gas entrainment across the jet boundary, momentum generation due to droplet evaporation, and interfacial momentum transfer between the mixture and droplets as well as between the mixture and solids. For simplicity, we may consider the Stokesian drag forces of individual droplets and solids are the only forces responsible for the interfacial momentum transfer between the mixture and other two phases. Hence the ξ-component momentum equation is given by

$$\begin{aligned}\frac{d}{d\xi}\left[\int_A \rho_m u u dA\right] &= \alpha_\infty \rho_\infty u_e u_\infty \ell \cos\theta + \int_{A_d} n_d \dot{m}_e u_d dA \\ &\quad + \int_{A_d} \mathrm{n}_d c_{dd} \frac{\pi}{8} d_d^2 \rho_m (u_d - u)^2 dA + \int_A n_p c_{dp} \frac{\pi}{8} d_p^2 \rho_m (u_p - u)^2 dA\end{aligned} \tag{5.2}$$

where u_d and u_p stand for the velocity of droplets along with the jet trajectory and the velocity of particles, respectively; d_d is the diameter of a droplet; n_p is the particle number density; c_{dd} and c_{dp} represent respectively the drag coefficient of a droplet and the drag coefficient of a particle, which can be estimated by

$$c_{dd} = \left(\frac{24}{\mathrm{Re_d}}\right)\left(1+\frac{1}{6}\mathrm{Re_d^{2/3}}\right), \qquad c_{dp} = \left(\frac{24}{\mathrm{Re_p}}\right)\left(1+\frac{1}{6}\mathrm{Re_p^{2/3}}\right) \tag{5.2a}$$

as suggested by Putnam (1961).

The η-component momentum equation is developed based on a η-component momentum balance among the change rate of momentum, momentum entrainment carried by the gas entrainment, and drag forces from the gas-solid flow around the jet, which is expressed by

$$\begin{aligned}\frac{d\theta}{d\xi}\left[\int_A \rho_m uudA\right] = -\alpha_\infty \rho_\infty u_e u_\infty \ell \sin\theta - C_g C_D \sqrt{\frac{A}{\pi}}\alpha_\infty \rho_\infty u_\infty^2 \sin^2\theta \\ - C_m(1-\alpha_\infty)\rho_p u_e \ell u_{p\infty} \sin\theta\end{aligned} \tag{5.3}$$

where C_D denotes the drag coefficient, which is estimated from a flow around a circular cylinder; C_g is a permeability correction factor of drag force for flow around the bent jet tube, which is approximated by the ratio of droplet mass flow rate to total jet mass flow rate; while C_m is a partition factor for momentum transfer by solids entrainment to the gas mixture. In this study,

$$C_\mathrm{D} = \begin{cases} 10 - 9\times 10^{-3}\,\mathrm{Re} & 1 \le \mathrm{Re} \le 10^3 \\ 1 & 10^3 \le \mathrm{Re} \le 10^4 \end{cases}, \quad C_g = \left(\frac{\rho_\mathrm{d} A_\mathrm{d}}{\rho A + \rho_\mathrm{d} A_\mathrm{d}}\right)^{0.25} \tag{5.3a}$$

The conservation of thermal energy is obtained based on the energy balance among the increase rate of flow enthalpy, the energy entrainment from the ambient gas stream, heat generation due to phase change, heat transfer between droplets and the mixture as well as the heat transfer between solids and the mixture, which is given by

$$\begin{aligned}\frac{d}{d\xi}\left[\int_A \rho_m u c_p T dA\right] = \alpha_\infty \rho_\infty u_e c_p T_\infty \ell + \int_{A_d} n_d \dot{m}_e (L + h_{do}) dA \\ + \int_{A_d} n_d \pi d_d^2 h_d (T_d - T) dA + \int_A (n_p - f_{dp}) \pi d_p^2 h_p (T_p - T) dA\end{aligned} \tag{5.4}$$

where c_p is the thermal capacity of gas-vapor mixture; T, T_d, and T_p represent respectively temperatures of the gas-vapor mixing phase, droplets and particles; h_d and h_p stand for the heat transfer coefficients of a single droplet and a single particle, respectively; and f_{dp} is the solids-droplets collision frequency. In the last term of right hand side of Equation (5.4), solids that collide with droplets are excluded from the heat transfer process between solids and the mixture of gas and vapor. In this study, the effective heat transfer coefficient of a single droplet can be obtained from the effective Nusselt number, which is determined by Dwyer (1985).

$$\mathrm{Nu}_d = \frac{2 + 0.6\mathrm{Re}_d^{*\,0.5}\mathrm{Pr}^{0.333}}{\left[1 + \dfrac{C_p(T - T_d)}{L}\right]^{0.7}} \tag{5.4a}$$

where the relative Reynolds number of droplets in a gas-solids mixture is defined by

$$\mathrm{Re}_d^* = \frac{(\rho_d \alpha_d + \rho_m)(u_d - u)d_d}{\mu} \tag{5.4b}$$

The Nusselt number for the heat transfer coefficient of a single particle can be expressed by the Ranz-Marshall equation

$$\mathrm{Nu}_p = 2 + 0.6\mathrm{Re}_p^{0.5}\mathrm{Pr}^{0.333} \tag{5.4c}$$

(2) Droplet phase

Spray of fast evaporating liquids typically evaporates within the spray mixing region. The spray evaporation region is thus bounded within the jet mixing boundary. It was assumed that only droplets on the outer boundary of the spray can get evaporated and the amount of droplets evaporated only depends on the amount of energy transferred into the spray region. For further simplicity, the sprays are considered straight without spray divergence. The continuity equation is based on the fact that the decrease rate of mass flow along ξ is due to the droplet evaporation, which gives

$$\frac{d}{d\xi}\left[\int_{A_d} \alpha_d \rho_d u_d dA\right] = -\int_{A_d} n_d \dot{m}_e dA \tag{5.5}$$

where A_d is the cross-sectional area of droplets jet; α_d is the volume fraction of droplets; and ρ_d stands for the density of droplets.

The ξ-component momentum equation is generated from a ξ-component momentum balance among the increase rate of droplet momentum flow, interfacial forces between droplets and the gaseous mixture, solids-droplets collision, and the momentum transfer due to droplet evaporation, which leads to

$$\frac{d}{d\xi}\left[\int_{A_d} \alpha_d \rho_d u_d u_d dA\right] = -\int_{A_d} \mathrm{n}_d c_{dd} \frac{\pi}{8} d_d^2 \rho_m (u_d - u)^2 dA + \int_{A_d} f_{dp} \frac{\pi}{6} d_p^3 \rho_p (u_p - u_d) dA - \int_{A_d} n_d \dot{m}_e u_d dA \tag{5.6}$$

where ρ_p is the density of solid particles and u_p is the velocity of solid particles along with the trajectory.

The η-component momentum equation can be obtained based on a η-component momentum balance among the change rate of momentum and the momentum entrainment due to the solids entrainment, which gives

$$\frac{d\theta}{d\xi}\left[\int_{A_d} \alpha_d \rho_d u_d u_d dA\right] = -(1 - C_m)(1 - \alpha_\infty)\rho_p u_e \ell u_{p\infty} \sin\theta \tag{5.7}$$

It is noted that Equations (5.7) and (5.3) are not independent from each other due to the previous assumption on the same centerline of all phases. Nevertheless, by solving the derivative term from Equation (5.3), Equation (5.7) can be regarded as an equation to estimate the partition factor C_m.

An energy balance is established among the increase rate of flow enthalpy of droplets, heat convection from the gaseous mixture, heat transfer from solids by collision, and the latent heat transfer due to droplet evaporation. Thus the energy equation of droplets is obtained by

$$\begin{aligned}\frac{d}{d\xi}\left[\int_{A_d} \alpha_d \rho_d u_d c_{pd} T_d dA\right] &= \int_{A_d} \pi n_d d_d^2 h_d (T - T_d) dA - \int_{A_d} n_d \dot{m}_e (L + h_{do}) dA \\ &+ \int_{A_d} f_{dp} \frac{\pi}{6} d_p^3 \rho_p c_{pp} (T_p - T_d) dA\end{aligned} \tag{5.8}$$

where c_{pd} is the thermal capacity of liquid droplets while c_{pp} is the thermal capacity of solid particles.

(3) Solids phase

It is assumed that solids enter the mixing region only by jet entrainment and all entrained solids flow along the ξ-direction only. Once solids collide with a droplet, they remain trapped until the host droplet is completely evaporated. The effect of the solids reoccurrence from evaporated droplets is neglected. Thus the mass balance equations is obtained by

$$\frac{d}{d\xi}\left[\int_A \alpha_p \rho_p u_p dA\right] = (1 - \alpha_\infty) \rho_p u_{ep} \ell \tag{5.9}$$

where u_{ep} represents the entrainment velocity of solid particle.

The momentum equation is obtained based a momentum balance among the increase rate of solids momentum flow, momentum transfer by solids entrainment, interfacial forces from the gaseous mixture, and momentum changes due to solids-droplets collision, which is expressed by

$$\begin{aligned}\frac{d}{d\xi}\left[\int_A \alpha_p \rho_p u_p u_p dA\right] &= (1-\alpha_\infty)\rho_p u_{ep} \ell u_{p\infty} \cos\theta - \int_{A_d} f_{dp} \frac{\pi}{6} d_p^3 \rho_p \left(u_p - u_d\right) dA \\ &\quad - \int_A n_p c_{dp} \frac{\pi}{8} d_p^2 \rho_m \left(u_p - u\right)^2 dA\end{aligned} \tag{5.10}$$

In this modeling approach, it was assumed that all entrained solids flow along the ξ-direction only and the η-component entrained momentum from the solids entrainment has been partitioned to the gas-mixture via interfacial forces and to the droplet phase via collision. Therefore, there is no η-component momentum equation for the solids phase. The energy equation of solids phase is based on an energy balance among the increase rate of flow enthalpy of solids, heat transfer from the solids entrainment, heat transfer by droplets-solids collision, and heat transfer between solids and gaseous mixture, which gives

$$\begin{aligned}\frac{d}{d\xi}\left[\int_A \alpha_p \rho_p u_p c_{pp} T_p dA\right] &= \alpha_{p\infty} \rho_p u_{e\,p} c_{pp} T_{p\infty} \ell - \int_{A_d} f_{dp} \frac{\pi}{6} d_p^3 \rho_p c_{pp} \left(T_p - T_d\right) dA \\ &\quad - \int_A (n_p - f_{dp}) \pi d_p^2 h_p \left(T_p - T\right) dA\end{aligned} \tag{5.11}$$

Up to now, the whole system governing equations is built. If these variable distributions on the cross-section are available, the governing equations could be solved with integral technique. Since determining these distributions is very difficult, the cross-sectional averages are defined as follows to simplify the governing equations,

$$\Gamma_d = \int_{A_d} n_d \dot{m}_e dA \; ; \qquad \int_A \rho_m u dA = A\overline{\dot{m}} \; ; \qquad \int_A \rho_m uu dA = A\overline{\dot{m}}\,\overline{u} \; ; \qquad \int_A \rho_m uT dA = A\overline{\dot{m}}\,\overline{T}$$

$$\int_{A_d} \alpha_d \rho_d u_d dA = A_d \overline{\dot{m}}_d \; ; \qquad \int_{A_d} \alpha_d \rho_d u_d u_d dA = A_d \overline{\dot{m}}_d \overline{u}_d \; ; \qquad \int_{A_d} \alpha_d \rho_d u_d T_d dA = A_d \overline{\dot{m}}_d T_d$$

$$\int_A \alpha_p \rho_p u_p dA = \overline{\alpha}_p \rho_p \overline{u}_p A ; \quad \int_A \alpha_p \rho_p u_p u_p dA = \overline{\alpha}_p \rho_p \overline{u}_p^2 A ; \quad \int_A \alpha_p \rho_p u_p T_p dA = \overline{\alpha}_p \rho_p \overline{u}_p \overline{T}_p A \tag{5.12}$$

Substituting Equation (5.12) into Equations (5.1)-(5.11), the final form of governing equations for vapor, droplet and particle phases are obtained as

$$\frac{d}{d\xi}\left(\overline{\dot{m}}A\right) = \alpha_\infty \rho_\infty u_e l + \Gamma_d \tag{5.13}$$

$$\begin{aligned} \frac{d}{d\xi}(\overline{\dot{m}}\,\overline{u}A) &= \alpha_\infty \rho_\infty u_e u_\infty l \cos\theta + \Gamma_d \overline{u}_d \\ &\quad + \frac{\pi}{8} \mathrm{n_d} c_{dd} d_d^2 \rho_m \left(\overline{u}_d - \overline{u}\right)^2 A_d + \frac{\pi}{8} \mu n_p c_{dp} d_p^2 \left(\overline{u}_p - \overline{u}\right)^2 A \end{aligned} \tag{5.14}$$

$$\begin{aligned} (\overline{\dot{m}}\,\overline{u}A)\frac{d\theta}{d\xi} &= -\alpha_\infty \rho_\infty u_e u_\infty l \sin\theta - C_g C_D \sqrt{\frac{A}{\pi}} \alpha_\infty \rho_\infty u_\infty^2 \sin^2\theta \\ &\quad - C_m (1-\alpha_\infty) \rho_p u_e l u_{p\infty} \sin\theta \end{aligned} \tag{5.15}$$

$$\begin{aligned} \frac{d}{d\xi}\left(\overline{\dot{m}} c_p \overline{T} A\right) &= \alpha_\infty \rho_\infty u_e c_p T_\infty l + \Gamma_d \left(L + h_{d0}\right) \\ &\quad + \pi n_d d_d^2 h_d \left(T_d - \overline{T}\right) A_d \end{aligned} \tag{5.16}$$

$$\frac{d}{d\xi}\left(\overline{\dot{m}}_d A_d\right) = -\Gamma_d \tag{5.17}$$

$$\begin{aligned} \frac{d}{d\xi}(\overline{\dot{m}}_d \overline{u}_d A_d) &= -\frac{\pi}{8} n_d c_{dd} d_d^2 \rho_m \left(\overline{u} - \overline{u}_d\right)^2 A_d \\ &\quad + f_{dp} \frac{\pi}{6} d_p^3 \rho_p \left(\overline{u}_p - \overline{u}_d\right) A_d - \Gamma_d \overline{u}_d \end{aligned} \tag{5.18}$$

$$(\overline{\dot{m}}_d u_d A_d)\frac{d\theta}{d\xi} = -(1 - C_m)(1-\alpha_\infty) \rho_p u_e l u_{p\infty} \sin\theta \tag{5.19}$$

$$\frac{d}{d\xi}\left(\overline{\dot{m}}_d c_{pd} T_d A_d\right) = \pi \mu n_d d_d^2 h_d \left(\overline{T} - T_d\right) A_d + f_{dp} \frac{\pi}{6} d_p^3 \rho_p c_{pp} \left(T_{p\infty} - T_d\right) A_d - \Gamma_d \left(L + h_{d0}\right) \tag{5.20}$$

$$\frac{d}{d\xi}(\overline{\alpha}_p \rho_p \overline{u}_p A) = (1 - \alpha_\infty) \rho_p u_{ep} l \tag{5.21}$$

$$\frac{d}{d\xi}(\overline{\alpha}_p \rho_p \overline{u}_p^2 A) = (1 - \alpha_\infty) \rho_p u_e l u_{p\infty} \cos\theta - f_{dp} \frac{\pi}{6} d_p^3 \rho_p \left(\overline{u}_p - \overline{u}_d\right) A_d - \frac{\pi}{8} n_p c_{dp} d_p^2 \rho_m (\overline{u}_p - \overline{u})^2 A \tag{5.22}$$

$$\frac{d}{d\xi}(\overline{\alpha}_p \rho_p \overline{u}_p^2 c_{pp} \overline{T}_p A) = (1 - \alpha_\infty) \rho_p u_{ep} c_{pp} T_{p\infty} l - f_{dp} \frac{\pi}{6} d_p^3 \rho_p c_{pp} \left(\overline{T}_p - T_d\right) A_d - \pi (n_p - f_{dp}) d_p^2 h_p (\overline{T}_p - \overline{T}) A \tag{5.23}$$

(4) Problem closure

An additional equation is needed to closure the problem. The equation of state of ideal gas to the gas-vapor mixture was applied to yield

$$\overline{\dot{m}} = (1 - \overline{\alpha}_p - \alpha_d) \frac{P \overline{u}}{R \overline{T}} \tag{5.24}$$

So far there are 11 coupled independent equations (from Equations (5.13) to (5.24), except for (5.19)) for solving 11 independent variables (A, A_d, θ, $\overline{\dot{m}}$, $\overline{\alpha}_p$, Γ_d, $\overline{u}$, $\overline{u}_d$, $\overline{u}_p$, $\overline{T}$, $\overline{T}_p$). The problem in principle is closed. Hence, with the given or presumed cross-sectional distributions for variables of interest, the coupled differential equations become solvable.

5.2.2 Intrinsic Correlation

In order to solve the governing equations, additional intrinsic correlations on the flow entrainment velocity, particle collision frequency and collision efficiency must be provided. Although the presence of particles and droplets in the jet flow does affect the flow entrainment, there is no simple correlation to quantify this effect. The equation of jet entrainment velocity in single-phase flows was used in this model, which was proposed by Platten and Keffer (1968), as the first-order approximation. Hence, the flow entrainment velocity is estimated by

$$u_e = 0.06(u - u_\infty \cos\theta) + 0.3u_\infty(\cos\theta - \cos\theta_0) \qquad (5.25a)$$

A similar equation is extended to estimate the jet entrainment of particle phase so that

$$u_{ep} = 0.06(u_p - u_{p\infty} \cos\theta) + 0.3u_{p\infty}(\cos\theta - \cos\theta_0) \qquad (5.25b)$$

Although the above entrainment velocity was originally obtained from the study of oblique jets, the extension of this equation to a co-current case reveals a close resembling of the equations directly derived from co-current jet studies, for example, $u_e = 0.026(u - u_\infty)$ from Rajaratnam (1976). For simplicity and generality of the mechanistic modeling, Equation (5.25) was adopted as a general one to cover all injection angles.

Collision frequency among droplets and solid particles can be calculated by Fan and Zhu (1998)

$$f_{dp} = \eta_{co} n_d n_p \frac{\pi (d_p + d_d)^2}{4} |u_p - u_d| \qquad (5.26)$$

where the collision efficiency, η_{co}, is given from an analytical approximation, which is derived based on the rigid sphere collisions in Stokesian flows (Zhu, 2000)

$$\eta_{co} = \left(1 + 34 \frac{d_d}{d_p} \frac{\rho}{\rho_p} \frac{1}{\mathrm{Re}_{pd}}\right)^{-2} \tag{5.27}$$

where Re_{pd} is the particle Reynolds number based on the relative velocity of particle and droplet.

5.3 Results and Discussion

First, a comparison with the experimental result is analyzed to assess the present parametric model, which is presented in Section 5.3.1. Based on the proposed parametric model, various parametric effects such as particle volume fraction on spray penetration and effect of injection angle on jet trajectory have been investigated in Section 5.3.2.

5.3.1 Comparison with Experimental Results

The spray location can also be identified from the temperature profile measurements. Figure 5.3 illustrates a typical comparison on crossflow spray trajectory, which shows a good agreement among the parametric model predictions, visualization, and the temperature detection of 10-thermocouple measurement. The lowest temperature point implies the location of spray trajectory in this section. The theoretical interpretation of temperature measurements is available in Wang and Zhu (2002).

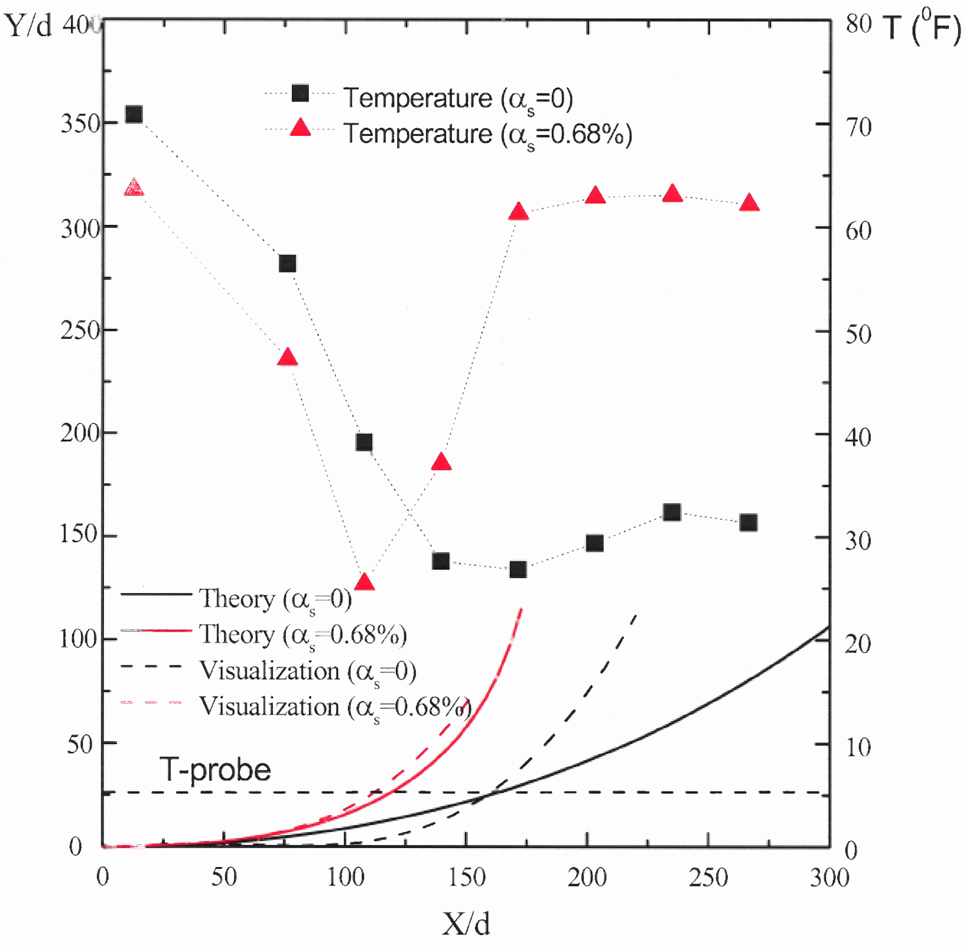

Figure 5.3 Comparison between experimental results and theoretical study (Circle-1, 0° injection).

The comparison of oblique (40°) spray trajectory is shown in Figure 5.4, which also shows a good agreement. Note that the parametric model is derived based on the circular nozzle assumption. If it was applied for flat nozzle, the hydraulic diameter of the flat should be used. However, it could not be utilized for the flat nozzle used in this experimental study in Chapter 3 and Chapter 4, since the aspect ratio of the openness of this flat nozzle is too large, more than 10.

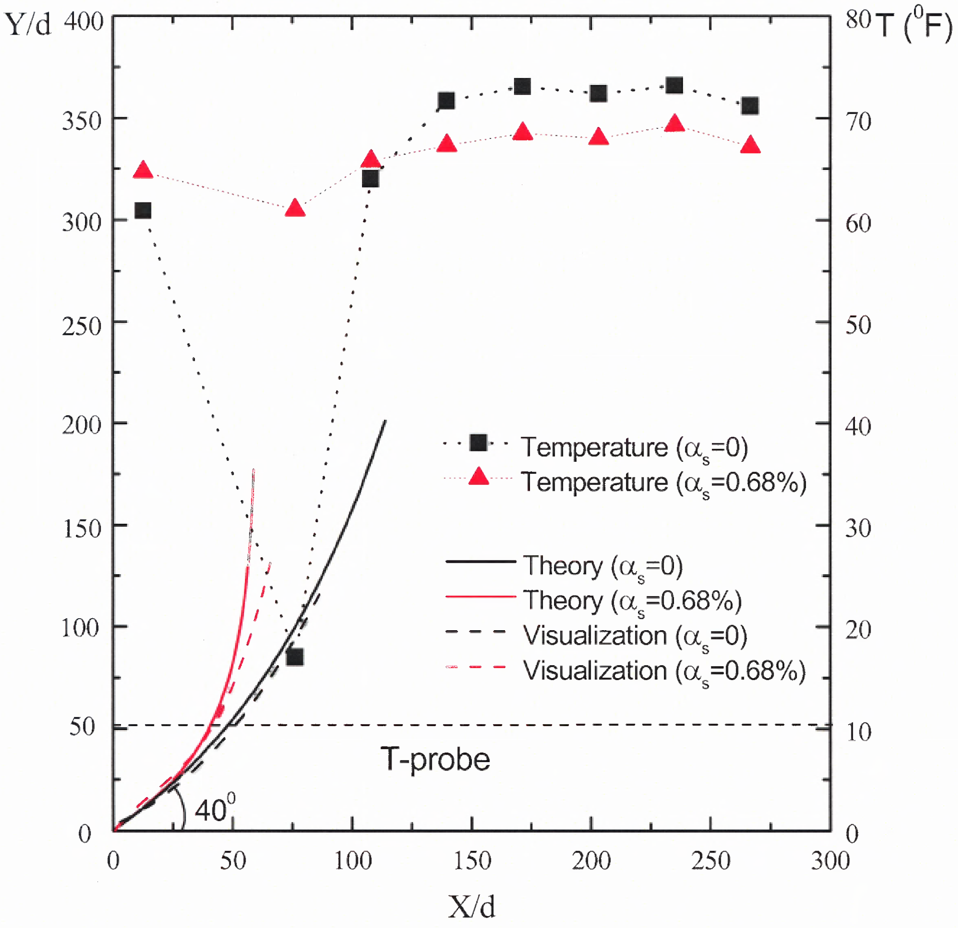

Figure 5.4 Comparison between experimental results and theoretical study (Circle-1, 40° injection).

The estimation of the parametric model has also been found to be in good agreement with the experimental results of 48-thermocouple measurement system, as shown in Figure 5.5. Comparing to the experimental results, the theoretical model overestimated the spray bending angle, as seen in Figure 5.5. This is because in this model the particle entrainment velocity was treated as the same one of the gas entrainment. However, there always exists a slip phenomenon, i.e., the entrainment velocity of particle is always smaller than that of the gas. With the increase of the initial solid volume fraction, the slip velocity increases. Therefore, the erroneousness of prediction of the parametric model will increase along with the increase of solid volume fraction.

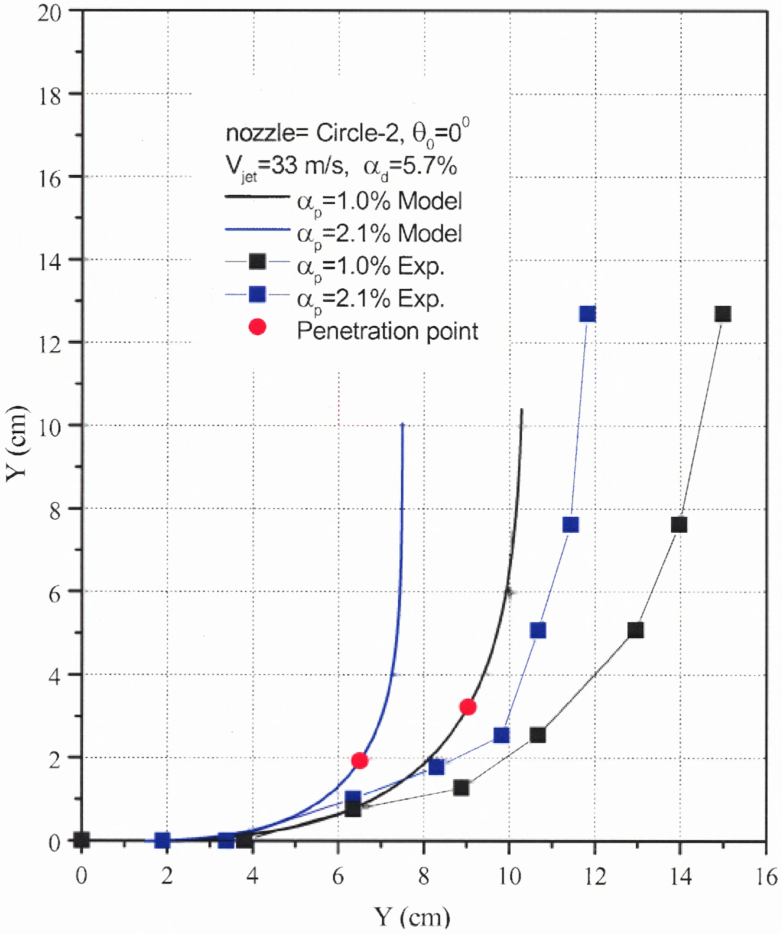

Figure 5.5 Comparison between experimental results and theoretical study (Circle-2, 0° injection, 33 m/s jetting velocity).

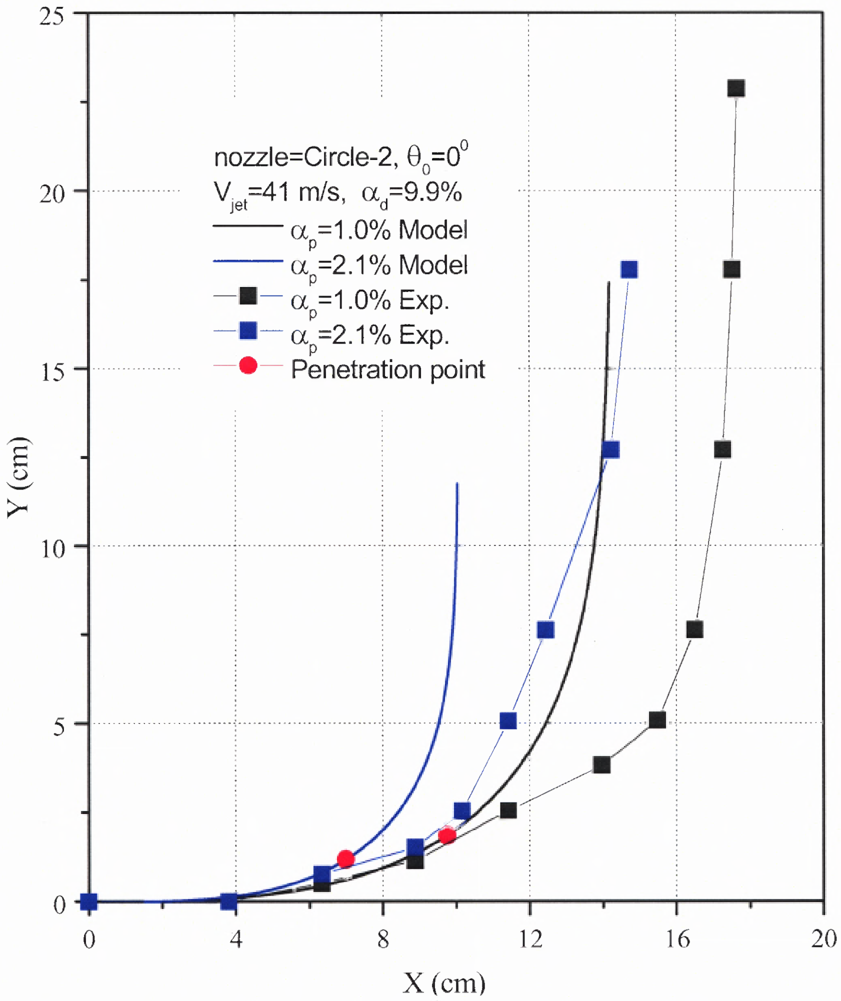

Figure 5.6 Comparison between experimental results and theoretical study (Circle-2, 0° injection, 41 m/s jetting velocity).

With the increase of spray jetting velocity, the spray penetration length increases, as shown in Figure 5.6. Both experimental results and theoretical estimations yield this conclusion, which could be explained that with the increase of spray momentum, the spray droplet can travel longer. Figure 5.7 presents the comparison result of oblique spray.

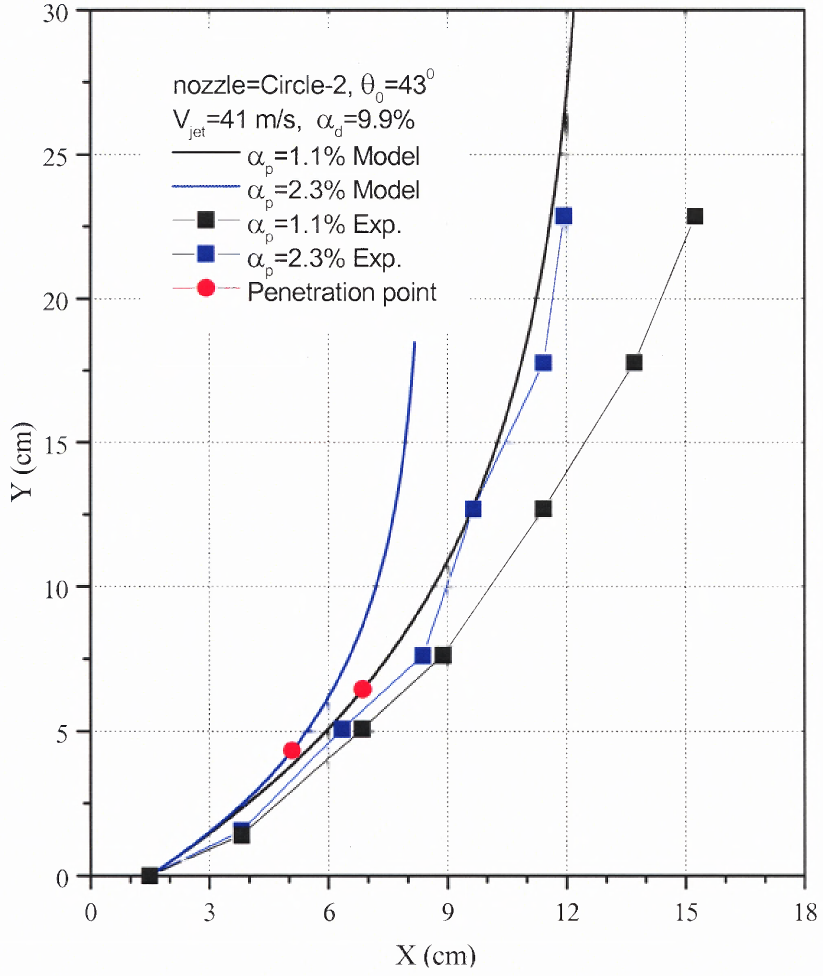

Figure 5.7 Comparison between experimental results and theoretical study (Circle-2, 43° injection, 41 m/s jetting velocity).

Figure 5.8 shows the results of Circle-3 nozzle, with 43° injecting angle, at 1.1% solid volume fraction. Although the jetting velocity of Circle-3 is less than that of Circle-2, the penetration length is much farther than that of Circle-2. This is due to the mass flow rate of Circle-3 larger than that of Circle-2. Due to the high mass flow rate in Circle-3, in order to protect the test plastic chamber from cracking, no experiment of normal injecting was performed using Circle-3. The phenomenon of plastic cracking has been observed in some experiments in this study, which is due to the direct contact of liquid nitrogen and chamber surface.

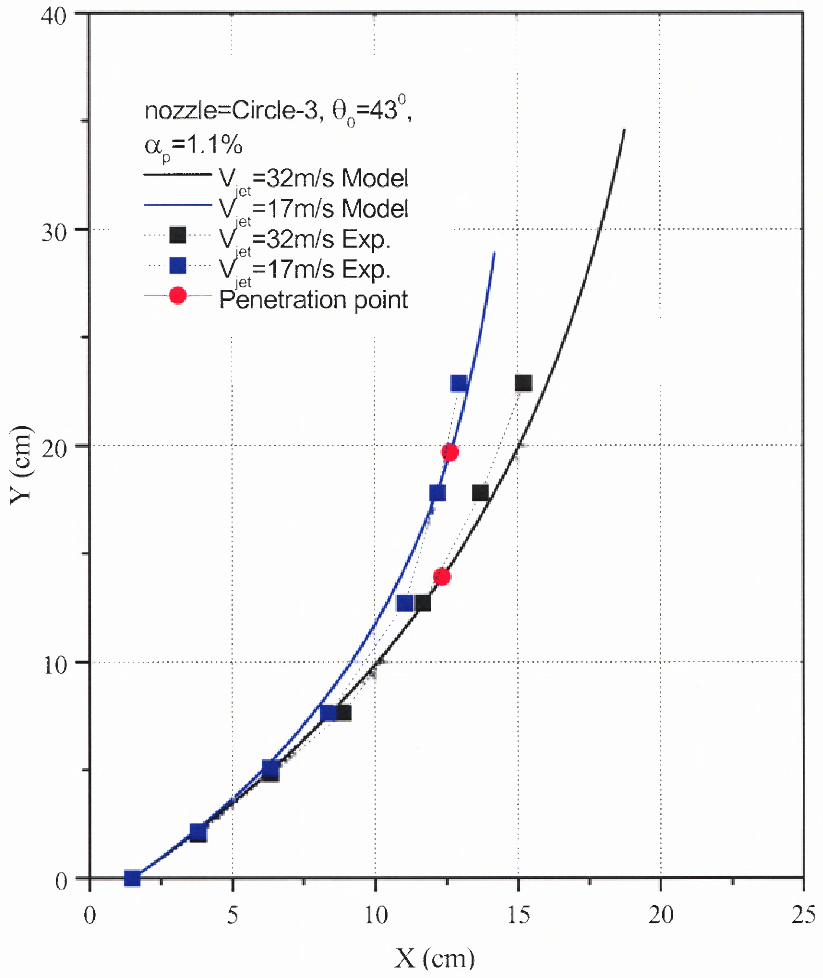

Figure 5.8 Comparison between experimental results and theoretical study (Circle-3, 43° injection, 1.1% solid volume fraction).

5.3.2 Parametric Study

(1) Effects of solids loading on spray penetration

The experimental study in Chapter 4 showed that the presence of solid particles could significantly reduce the jet penetration length in a gas-solid flow. Figure 5.9 illustrates the effect of solid loading on spray penetration length for crossflow spray jet, which shows that the jet penetration lengths are significantly shortened. It is interesting to note that, with the increase of solids loading, the penetration length decreases asymptotically. In this example, significant reductions of evaporation lengths occur within a solids volumetric loading of 0.2 %.

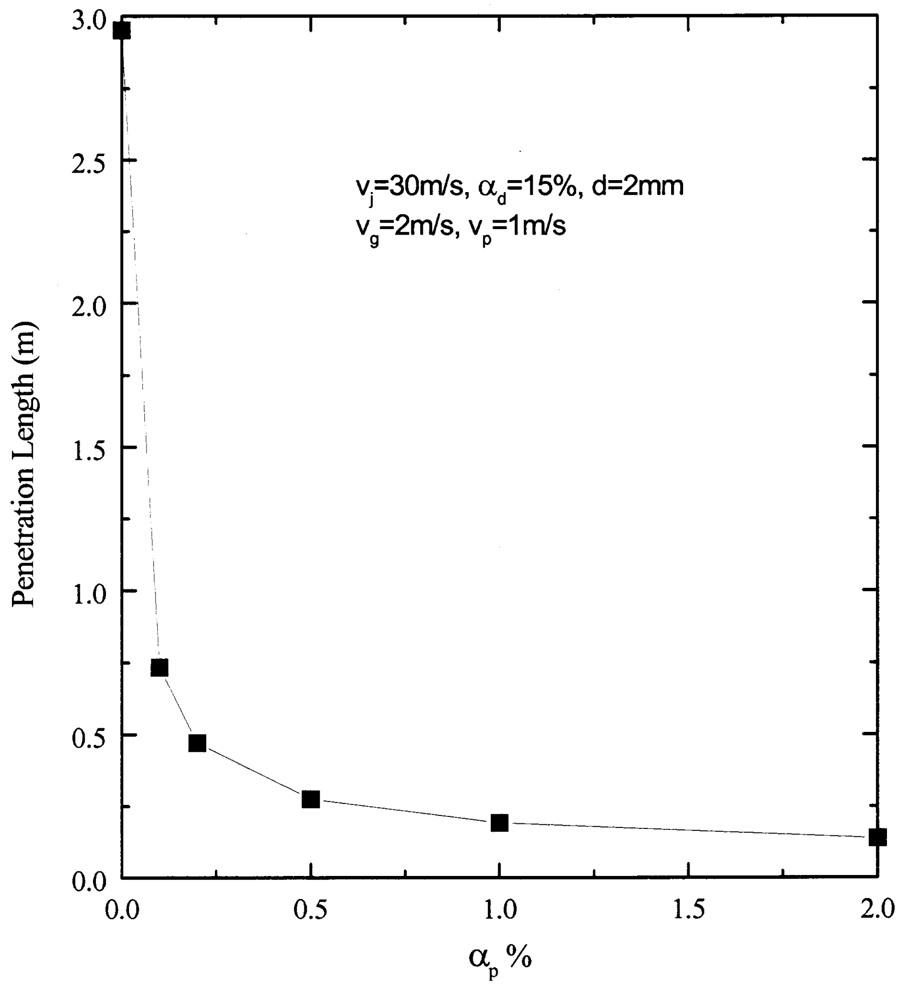

Figure 5.9 Effect of solid loading on spray penetration.

The effect of solids on spray penetration length can be expected because, in the presence of solid particles, the liquid spray jets acquire much more heat through the collision between particles and droplets, and hence the droplets evaporate quicker than that in particle-free flows. However, as mentioned before, this parametric model might somewhat overestimate the effect of solids loading on spray penetration by the assumption of non-slip velocity between gas and particle.

(2) Effect of injection angle on spray trajectory

As indicated in Chapter 4 as well as Section 5.3.1, spray injection angle can have a strong influence on spray trajectory and evaporation rate. This is because the spray trajectory is heavily dependent on the drag forces from the air stream and the collision forces from the solids phase, which varies at different spray injection angles under otherwise the same conditions. The heat transfer, a vital factor for the droplet evaporation, is dominated by heat convection of gas flowing around droplets and heat conduction upon solids-droplet collisions. Both heat transfer mechanisms are injection angle dependent. Figure 5.10 shows a typical effect of injection angle on spray trajectory and evaporation length, which indicates a longer evaporation length at a bigger injection angle towards the co-current jet spray. This is due to the fact that, with the decrease of jet injection angle, the entrainment amount of both solid particles and air gas increases, and, at the same time, the convection effect becomes increasingly important, which leads to more heat transfer to liquid droplets and accelerates the evaporation of droplets. Note that the evaporation length and penetration length have different meaning. Evaporation length is the distance along with the spray trajectory, while penetration length is the distance penetrated by sprays in the x-direction.

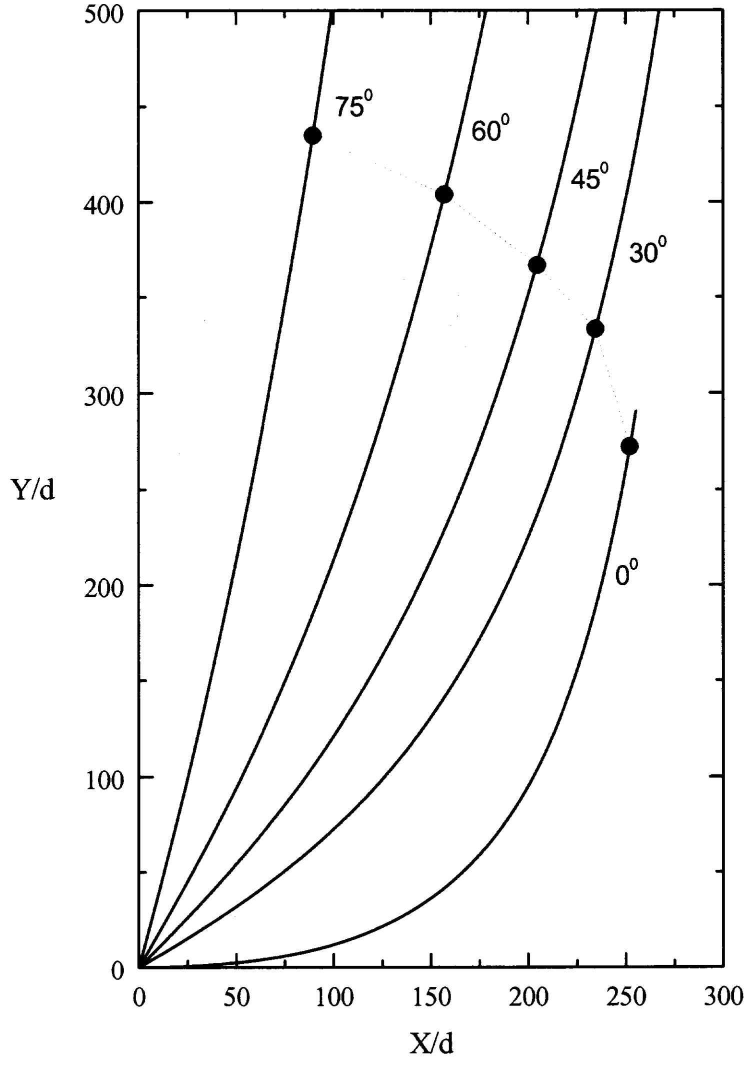

Figure 5.10 Effect of injection angle on spray trajectory and penetration.

(3) Effect of spray nozzle size on spray trajectory

The increase in spray nozzle diameter results in a significant increase in the spray jet penetration length as well as deeply affects the spray trajectory, as illustrated in Figure 5.11. This phenomenon is similar to those in the single-phase jet analysis (Abramovich, 1963) where a linear relationship between jet diameter and jet penetration is derived.

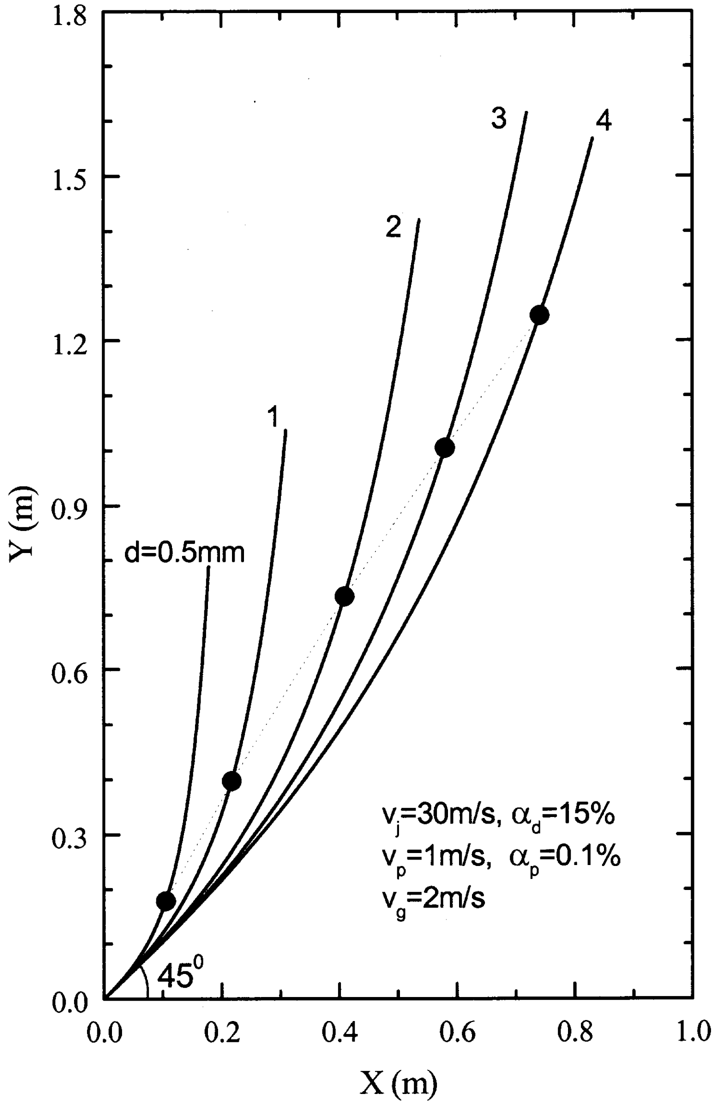

Figure 5.11 Effect of diameter of nozzle on spray trajectory.

(4) Effect of liquid volume fraction on spray trajectory

Figure 5.12 shows the effect of liquid volume fraction at nozzle tip on the spray trajectory. The higher the liquid volume fraction, the less deflection and deeper penetrates.

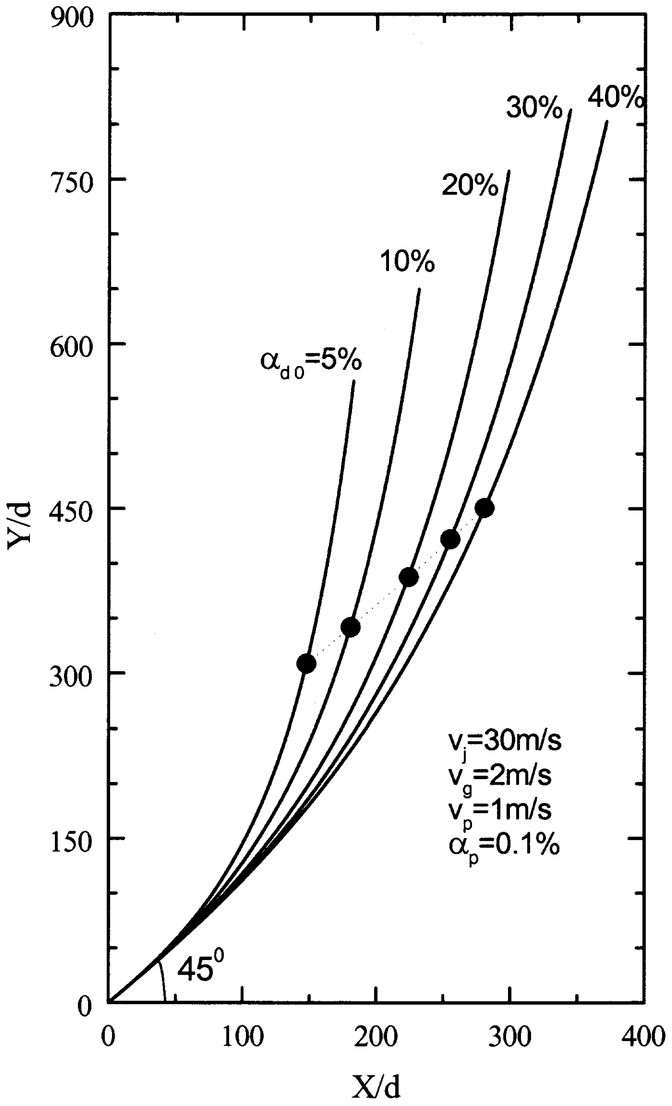

Figure 5.12 Effect of liquid volume fraction on spray trajectory.

(5) Dilution effects by evaporation

Droplet evaporation in gas-solid flows leads to the dilution effects on solids concentration as well as temperature reduction of all phases in the spray evaporation region. Figure 5.13 shows a velocity distribution of the gas-vapor mixture along the jet trajectory. As shown in Figure 5.13, the gas phase velocity is above the ambient velocity within the evaporation region, due to the addition of vapor by droplets evaporation as well as the initial injection velocity. The gas velocity reduces quickly along with the jet trajectory by the quick reduction of the evaporation rate. Figure 5.13 also illustrates the effect of solid loadings on the velocity distribution. The higher the solids loading the quicker the velocity reduces. This is because a higher solids loading means more solid particles entrained into the spray evaporation region, which leads to an increased drag force to the gas phase. When the gas velocity decreases to a level below the ambient velocity of gas-solid suspension, the gas velocity in the evaporation region intends to increase due to the effect of momentum transfers across the jet boundary. Consequently, the gas velocity approaches asymptotically to the ambient value.

The gas temperature distribution along with the jet trajectory, at different solid loadings, is shown in Figure 5.14. The temperature dilution effect is reflected in Figure 5.14 by the fact that the gas temperature in the evaporation region is always below the ambient value. The higher the solids loading is the quicker increase is in the gas temperature since the higher solid loading contributes more heat to droplet vaporization and gas-vapor mixture.

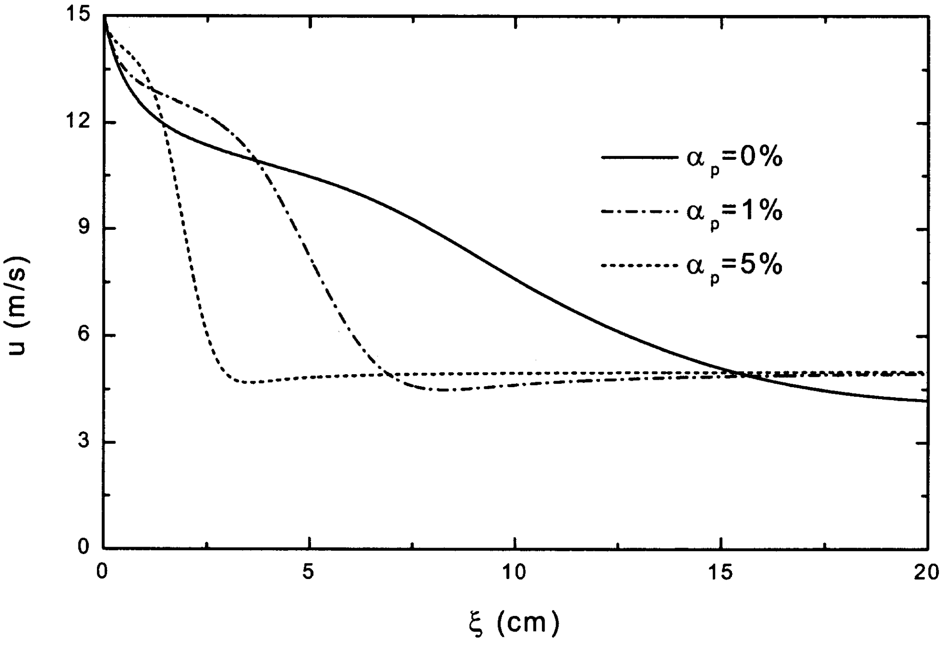

Figure 5.13 Gas velocity distribution along with spray trajectory.

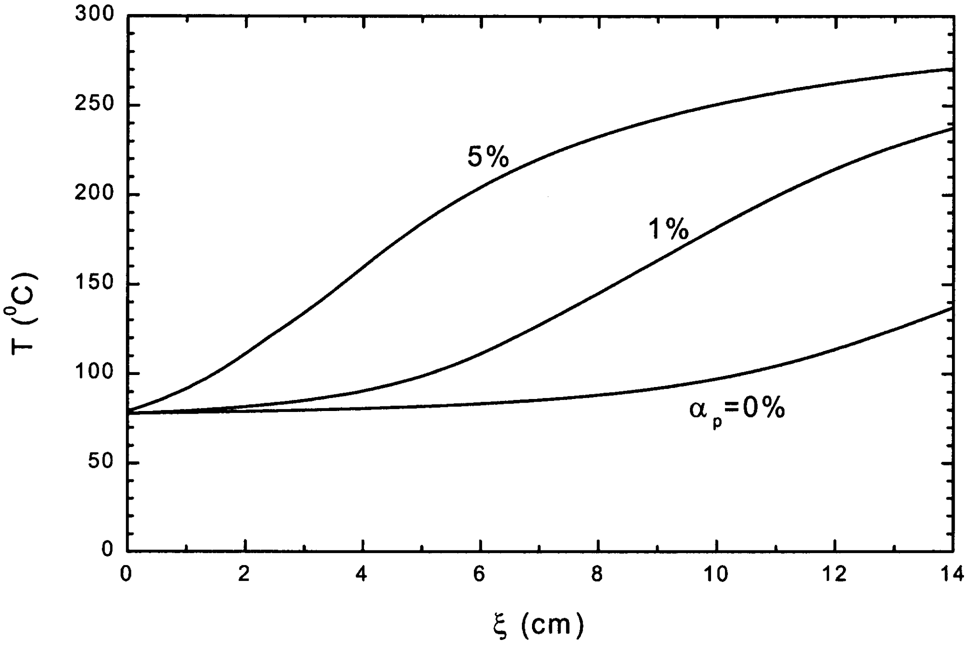

Figure 5.14 Gas temperature distribution along spray tractory.

5.4 Conclusions

A parametric model has been developed for study of evaporating liquid spray jet evaporation in gas-solid suspension flows, which includes all phase interactions with phase changes in the three phases. In order to validate the parametric model, some quantitative comparisons between the measurements and modeling predictions are made for the different spray cases. All of these comparisons show fairly good agreements on the effect of solids volumetric loading, the effect of injection angle, and the effects of some other operating parameters, which to some extent validate the parametric model efforts.

Parametric effects on the mixing characteristics such as penetration length, temperature and velocity of each phase, trajectories, and the phase volume fraction distributions are illustrated. It is found that the penetration length is shortened in the presence of particles in a liquid spray jet of any injection angle. The penetration length decreases with the increase of solids loading. Effects of spray injecting angle, diameter of nozzle tip, and liquid volume fraction at nozzle tip on both spray trajectory and penetration are also illustrated.

CHAPTER 6

DROPLET-PARTICLE COLLISION OVER LEIDENFROST TEMPERATURE

6.1 Introduction

With a large droplet vaporization rate, the transient characteristics of evaporating liquid sprays into gas-solid suspensions plays a dominant role in the determination of phase transport. Many industrial applications call for a study on the transient heating, dynamic motion and vaporization of a droplet during a collision or a series of collisions with hot solid particles. The current methods of estimating the heat transfer and fluid dynamics of sprays impacting on hot surfaces are largely empirically based. In this chapter, an analytical model has been developed to describe the Leidenfrost collision between a droplet and hot solid sphere. Effects of Weber number and solid curvature on droplet collision and evaporation are illustrated. Modeling predictions are partially validated by the comparison with available experimental results.

6.2 Theoretical Development

The analysis of a droplet impinging on a hot solid surface demands a joint consideration of associated hydrodynamics and heat transfer with a deformed interface whose contour in turn depends on the phase transition at the interface. The highly complicated coupling prevents the problem from any practical solutions without simplifications. A number of assumptions therefore are introduced here. As shown in Figure 6.1, a curved disc of liquid is used to simulate the deformed droplet during a Leidenfrost collision.

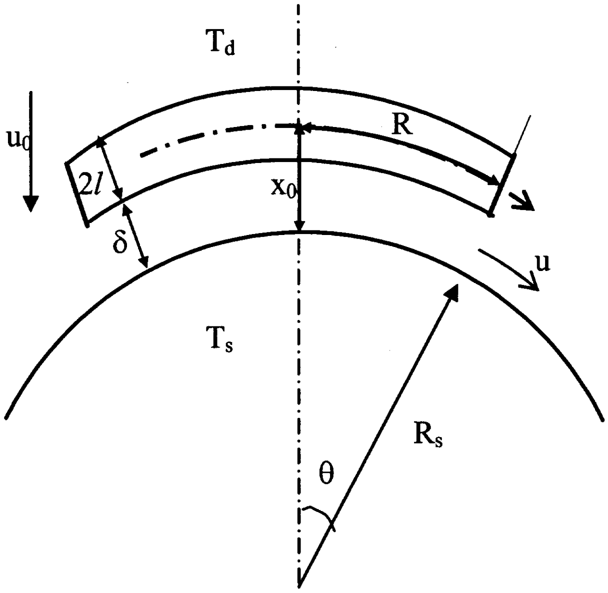

Figure 6.1 Schematic diagram of a droplet impacting spherical surface of a solid particle.

6.2.1 Heat Transfer and Evaporation Rate over Vapor Cushion

In order to analyze the heat transfer within the vapour layer, it is assumed:

(1) Only heat conduction through vapor cushion is considered, while both convective and radiative heat transfer have been neglected.

(2) Vapor cushion thickness δ is uniform and time-dependent. In addition the thickness is much smaller than the radii of the droplet and solid sphere.

(3) Thermal conductivity, k_v, dynamic viscosity, μ, and density, ρ_v, of the vapor are constant throughout the cushion, having values associated with the average vapor layer temperature which is determined as

$$T_v = \frac{T_s + T_d}{2} \tag{6.1}$$

(4) Before collision, the droplet is of the saturation temperature at the atmospheric pressure. Thus all transferred heat is used for droplet evaporation only.

Hence the heat flux from the hot solid to the droplet can be expressed as

$$q = \frac{k_v(T_s - T_d)}{\delta} \tag{6.2}$$

The vapor production rate per unit contact area is expressed in terms of evaporation rate m_v by

$$\dot{m}_v = \frac{k_v(T_s - T_d)}{\delta L} \tag{6.3}$$

Thus, the total evaporation rate is

$$m_v = \dot{m}_v S(\theta) = 2\pi R_s^{\,2}(1-\cos\theta)\frac{k_v \Delta T}{\delta L} \tag{6.4}$$

6.2.2 Governing Equations over Vapor Cushion

1. Momentum conservation

For incompressible and axisymetric flow without any field forces, the Navier-Stokes equations in polar coordinates reduce to

$$\begin{aligned} &\frac{\partial u_r}{\partial t} + u_r\frac{\partial u_r}{\partial r} + \frac{u_\theta}{r}\frac{\partial u_r}{\partial \theta} - \frac{u_\theta^2}{r} = -\frac{1}{\rho_v}\frac{\partial p}{\partial r} + \\ &\qquad \upsilon\left[\frac{\partial^2 u_r}{\partial r^2} + \frac{1}{r^2}\frac{\partial^2 u_r}{\partial \theta^2} + \frac{2}{r}\frac{\partial u_r}{\partial r} + \frac{\mathrm{ctg}\,\theta}{r^2}\frac{\partial u_r}{\partial \theta} - \frac{u_r}{r^2} - \frac{2}{r^2\sin\theta}\frac{\partial(u_\theta \sin\theta)}{\partial \theta}\right] \end{aligned} \tag{6.5}$$

$$\begin{aligned} &\frac{\partial u_\theta}{\partial t} + u_r\frac{\partial u_\theta}{\partial r} + \frac{u_\theta}{r}\frac{\partial u_\theta}{\partial \theta} - \frac{u_r u_\theta}{r} = -\frac{1}{\rho_v}\frac{1}{r}\frac{\partial p}{\partial \theta} + \\ &\qquad \upsilon\left[\frac{\partial^2 u_\theta}{\partial r^2} + \frac{1}{r^2}\frac{\partial^2 u_\theta}{\partial \theta^2} + \frac{2}{r}\frac{\partial u_\theta}{\partial r} + \frac{\mathrm{ctg}\,\theta}{r^2}\frac{\partial u_\theta}{\partial \theta} + \frac{2}{r^2}\frac{\partial u_r}{\partial r} - \frac{u_\theta}{r^2\sin^2\theta}\right] \end{aligned} \tag{6.6}$$

Two more assumptions are introduced to further simplify above momentum equations:

(1) Velocity variation with respect to time is small compared to the velocity variations with respect to spatial coordinates,

(2) Inertial terms are small compared with viscous terms (i.e. low vapor Reynolds number).

Using these assumptions and performing the order of magnitude analysis, Equation (6.5) simplifies to

$$-\frac{1}{\rho_v}\frac{\partial p}{\partial r}=0 \tag{6.7}$$

Therefore, the pressure is uniform across the height of the vapor layer. The order of magnitude analysis is also performed on Equation (6.6) and yields

$$\frac{1}{\mu_v}\frac{1}{r}\frac{dp}{d\theta}=\frac{\partial^2 u_\theta}{\partial r^2} \tag{6.8}$$

Integrating Equation (6.8) gives

$$u_\theta=\frac{1}{\mu_v}\frac{dp}{d\theta}(r\ln r-r)+c_1 r+c_2 \tag{6.9}$$

The integral constants c_1 and c_2 depend on the boundary conditions of the vapor layer. If it is assumed that the vapor radial velocities at both boundaries of the vapor layer are zero (i.e., non-slip conditions on droplet surface and solid surface), the vapor radial velocity is obtained as

$$u_\theta=\frac{1}{\mu_v}\frac{dp}{d\theta}(r\ln\frac{r}{R_s+\delta}+\frac{r-R_s-\delta}{\delta}R_s\ln\frac{R_s}{R_s+\delta}) \tag{6.10}$$

The average radial velocity of vapor at θ is defined by

$$\bar{u}_\theta=\frac{1}{\delta}\int_{R_s}^{R_s+\delta}u_\theta dr=\frac{1}{4\mu_v}\left[2(\frac{R_s}{\delta}+1)R_s\ln\frac{R_s}{R_s+\delta}+2R_s+\delta\right](-\frac{dp}{d\theta}) \tag{6.11}$$

Using the following approximation

$$\ln x = (x-1) - \frac{(x-1)^2}{2} + \frac{(x-1)^3}{3} - \frac{(x-1)^4}{4} + \cdots \quad \text{at } 0<x<2 \tag{6.12}$$

and noting $\frac{\delta}{R_s} << 1$, Equation (6.11) reduces

$$\bar{u}_\theta = \frac{\delta^2}{12\mu_v R_s}(-\frac{dp}{d\theta}) \tag{6.13}$$

2. Mass Conservation

Considering the vapor mass balance in ther vapor layer, the total vapor conservation equation can be given by

$$m_v = \rho_v 2\pi R_s \sin\theta \delta \bar{u}_\theta \tag{6.14}$$

Introducing Equation (6.13) into Equation (6.14) gives

$$m_v = \frac{\pi\delta^3}{6\nu_v}(-\frac{dp}{d\theta})\sin\theta \tag{6.15}$$

The combination of Equations (6.4) and (6.15) gives the pressure gradient along with the θ coordinate

$$-\frac{dp}{d\theta} = \frac{12\nu_v k_v \Delta T}{L}\frac{R_s^{\ 2}}{\delta^4}\frac{1-\cos\theta}{\sin\theta} \tag{6.16}$$

Now, the pressure distribution in the vapor layer is given by

$$\int_{p(0)}^{p(\theta)}(-dp) = 12\frac{\nu_v k_v \Delta T}{L}\frac{R_s^{\ 2}}{\delta^4}\int_0^\theta \frac{1-\cos\theta}{\sin\theta}d\theta \tag{6.17}$$

where p(0) is the pressure at the center of the vapor layer. Equation (6.17) gives

$$p(\theta) - p(0) = 24\frac{\nu_v k_v \Delta T}{L}\frac{R_s^{\ 2}}{\delta^4}\ln\cos\frac{\theta}{2} \tag{6.18}$$

At the boundary of the vapor layer, i.e. $\theta = \theta_m$, the pressure is zero. Thus, the pressure distribution is

$$p(\theta) = 24\frac{\nu_v k_v \Delta T}{L}\frac{R_s^{\,2}}{\delta^4}\ln\frac{\cos\frac{\theta}{2}}{\cos\frac{\theta_m}{2}} \tag{6.19}$$

where θ_m is defined as the maximum angle of the vapor layer.

The force from the vapor on the impinging droplet is

$$F = \int_A p(\theta)\cos\theta dA = 2\pi R_s^{\,2}\int_0^{\theta_m} p(\theta)\cos\theta\sin\theta d\theta \tag{6.20}$$

Substituting Equation (6.19) into Equation (6.20) yields

$$F = 6\pi\frac{\nu_v k_v \Delta T}{L}\frac{R_s^{\,4}}{\delta^4}(1-\cos\theta_m)^2 \tag{6.21}$$

Using $R=R_s\theta_m$, Equation (6.21) can be rewritten

$$F = \frac{3\pi}{2}\frac{\nu_v k_v \Delta T}{L}\frac{R^4}{\delta^4}\frac{\sin^4\left(\frac{\theta_m}{2}\right)}{\left(\frac{\theta_m}{2}\right)^4} \tag{6.22}$$

Note that if the assumption that the solid size is much larger than the droplet size, Equation (6.22) is simplified

$$F = \frac{3\pi}{2}\frac{\nu_v k_v \Delta T}{L}\frac{R^4}{\delta^4} \tag{6.23}$$

This equation was used by Buyevich *et al.* (1995) in their work on droplet impacts on a plate surface.

6.2.3 Energy Balance of Liquid Droplet

It is noted that the total evaporated mass of droplet during a Leidenfrost collision is typically two orders of magnitude smaller than the droplet original mass. Hence, due to the incompressibility of the droplet, the total volume of droplet is approximately conserved during a single Leidenfrost collision process. For a disc-like droplet, the radius and thickness 2*l* are related by

$$V = \frac{4}{3}\pi R_0^3 = 2\pi R^2 l \tag{6.24}$$

In order to simply the problem, the viscous energy dissipation inside the droplet is neglected. The kinetic energy of the droplet includes two parts: one is the whole motion energy, E_{k1}, while the other is the internal flow energy, E_{k2}, due to the droplet deformation. The potential energy of droplet is the energy, E_s of surface tension. The kinetic energy E_{k1} is given by

$$E_{k1} = \frac{1}{2} m_d u_d^2 = \frac{1}{2} m_d (\frac{dx_0}{dt})^2 \tag{6.25}$$

The kinetic energy E_{k2} is given by (Buyevich, *et al.*, 1986)

$$E_{k2} = \frac{1}{2} m_d (1 + \frac{8R_0^6}{3R^6})(\frac{dR}{dt})^2 \tag{6.26}$$

and the surface energy E_s is

$$E_s = (2\pi R^2 + 4\pi Rl)\sigma = 2\pi\sigma R(R + 2l) \tag{6.27}$$

According to the energy conservation law, the following relation is obtained

$$d(E_{k1} + E_{k2} + E_s) = F d\delta \tag{6.28}$$

where F is the force exerted by vapor pressure on the droplet and is given by Equation (6.21). Differentiating Equation (6.25) leads to

$$dE_{k1} = \frac{1}{2} m_d d\left[\left(\frac{dx_0}{dt}\right)^2\right] + \frac{1}{2}\left(\frac{dx_0}{dt}\right)^2 dm_d \tag{6.29}$$

Since $dx_0 = d\delta + dl$, Equation (6.29) becomes

$$\begin{aligned} dE_{k1} = m_d&\left[\left(\frac{d^2\delta}{dt}+\frac{4R_0^3}{R^4}\left(\frac{dR}{dt}\right)^2-\frac{4R_0^3}{3R^3}\frac{d^2R}{dt^2}\right)\left(d\delta-\frac{4R_0^3}{3R^3}dR\right)\right] \\ &-\frac{1}{2}m_v\left[\left(\frac{d\delta}{dt}-\frac{4R_0^3}{3R^3}\frac{dR}{dt}\right)d\delta+\left(\frac{4R_0^3}{3R^3}\right)^2\frac{dR}{dt}dR\right] \end{aligned} \tag{6.30}$$

Similarly, the following two equations can be derived

$$\begin{aligned} dE_{k2} = m_d&\left[\left(1+\frac{8R_0^6}{3R^6}\right)\frac{d^2R}{dt^2}-\frac{8R_0^6}{R^7}\left(\frac{dR}{dt}\right)^2\right]dR \\ &-\frac{1}{2}m_v\left(1+\frac{8R_0^6}{3R^6}\right)\frac{dR}{dt}dR \end{aligned} \tag{6.31}$$

and

$$dE_s = 2\sigma\left(2\pi R-\frac{4\pi R_0^3}{3R^2}\right)dR \tag{6.32}$$

Substitution of Equations (6.30), (6.31) and (6.32) into Equation (6.28) gives

$$\frac{d^2\delta}{dt^2}-\frac{4R_0^3}{3R^3}\frac{d^2R}{dt^2}+\frac{4R_0^3}{R^4}\left(\frac{dR}{dt}\right)^2-\frac{1}{2}\frac{m_v}{m_d}\left(\frac{d\delta}{dt}-\frac{4R_0^3}{3R^3}\frac{dR}{dt}\right)=\frac{F}{m_d} \tag{6.33}$$

$$\begin{aligned} &\left(1+\frac{8}{3}\frac{R_0^6}{R^6}\right)\frac{d^2R}{dt^2}-\frac{8R_0^6}{R^7}\left(\frac{dR}{dt}\right)^2+\frac{2\sigma}{m_d}\left(2\pi R-\frac{4\pi R_0^3}{3R^2}\right) \\ &\qquad -\frac{m_v}{2m_d}\left(1+\frac{8R_0^6}{3R^6}\right)\frac{dR}{dt}-\frac{m_v}{m_d}\frac{2R_0^3}{3R^3}\frac{d\delta}{dt}=\frac{4R_0^3}{3R^3}\frac{F}{m_d} \end{aligned} \tag{6.34}$$

Since $\frac{m_v}{m_d}$ <<1, Equations (6.33) and (6.34) changes to

$$\frac{d^2\delta}{dt^2}-\frac{4R_0^3}{3R^3}\frac{d^2R}{dt^2}+\frac{4R_0^3}{R^4}\left(\frac{dR}{dt}\right)^2=\frac{F}{m_d} \tag{6.35}$$

$$\left(1+\frac{8}{3}\frac{R_0^6}{R^6}\right)\frac{d^2R}{dt^2}-\frac{8R_0^6}{R^7}\left(\frac{dR}{dt}\right)^2+\frac{2\sigma}{m_d}\left(2\pi R-\frac{4\pi R_0^3}{3R^2}\right)=\frac{4R_0^3}{3R^3}\frac{F}{m_d} \tag{6.36}$$

Taking $\overline{R} = \frac{R}{R_0}$, $\overline{\delta} = \frac{\delta}{R_0}$ and $\tau = \frac{t}{\sqrt{\frac{\rho_d R_0^3}{\sigma}}}$, Equations (6.35) and (6.36) can be expressed in a dimensionless form as

$$\frac{d^2\overline{\delta}}{d\tau^2} - \frac{4}{3\overline{R}^3}\frac{d^2\overline{R}}{d\tau^2} + \frac{4}{\overline{R}^4}\left(\frac{d\overline{R}}{d\tau}\right)^2 = \frac{3F}{4\pi\sigma R_0} \tag{6.37}$$

$$\frac{d^2\overline{R}}{d\tau^2} + \frac{2}{\overline{R}^3}\frac{d^2\overline{\delta}}{d\tau^2} + 3\overline{R} - \frac{2}{\overline{R}^2} = \frac{5F}{2\pi\sigma R_0 \overline{R}^3} \tag{6.38}$$

Introducing Equation (6.21) into Equations (6.37) and (6.38) and noting that $R = R_s\theta_m$, gives

$$\frac{d^2\overline{\delta}}{d\tau^2} - \frac{4}{3\overline{R}^3}\frac{d^2\overline{R}}{d\tau^2} + \frac{4}{\overline{R}^4}(\frac{d\overline{R}}{d\tau})^2 = \frac{4.5\nu_v k_v \Delta T}{\sigma R_0 L}\frac{\chi^4}{\overline{\delta}^4}\left(1 - \cos\frac{\overline{R}}{\chi}\right)^2 \tag{6.39}$$

$$\frac{d^2\overline{R}}{d\tau^2} + \frac{2}{\overline{R}^3}\frac{d^2\overline{\delta}}{d\tau^2} + 3\overline{R} - \frac{2}{\overline{R}^2} = \frac{15\nu_v k_v \Delta T}{\sigma R_0 L}\frac{\chi^4}{\overline{\delta}^4\overline{R}^3}\left(1 - \cos\frac{\overline{R}}{\chi}\right)^2 \tag{6.40}$$

where $\chi = \frac{R_s}{R_0}$ is the ratio of the solid particle radius to the droplet radius.

The initial conditions are to be formulated in the following form

$$\overline{R}(0) = 1,\ \left.\frac{d\overline{R}}{d\tau}\right|_{\tau=0} = 0,\ \overline{\delta}(0) = \varepsilon < 1,\ \left.\frac{d\overline{\delta}}{d\tau}\right|_{\tau=0} = -\left(\frac{We}{2}\right)^{1/2} \tag{6.41}$$

The total evaporation flux per collision is calculated by

$$\Delta M_d = \int_0^{t_R} m_v dt = \frac{2\pi k_v \Delta T R_s^2}{L}\sqrt{\frac{\rho_d R_0}{\sigma}}\int_0^{\tau_R}\frac{(1-\cos\theta_m)}{\overline{\delta}}d\tau \tag{6.42}$$

where t_R (or $\tau_R = \frac{t_R}{\sqrt{\frac{\rho_d R_0^3}{\sigma}}}$) is the droplet residence time defined as the time from the moment of collision to the moment of departure from the surface. Apparently, the droplet residence time can be estimated from the fundamental oscillation frequency which Rayleigh (1879) derived for very small deviations from a sphere

$$t_R = \pi\sqrt{\frac{\rho_d R_0^3}{2\sigma}} \tag{6.43}$$

Therefore, the dimensionless residence time is a constant

$$\tau_R = \frac{\pi}{\sqrt{2}} \approx 2.22 \tag{6.44}$$

Thus, the evaporation ratio of the liquid droplet is

$$r_v = \frac{\Delta M_d}{M_{d0}} = \frac{3k_v \Delta T \chi}{2\rho_d L}\sqrt{\frac{\rho_d}{\sigma R_0}}\int_0^{\tau_R}\frac{(1-\cos\theta_m)}{\bar{\delta}}d\tau \tag{6.45}$$

The temperature reduction of solid particle is given by

$$\Delta T_s = \frac{\Delta M_d L}{C_{ps} M_s} = \frac{3k_v \Delta T}{2C_{ps}\rho_s \chi}\sqrt{\frac{\rho_d}{\sigma R_0}}\int_0^{\tau_R}\frac{(1-\cos\theta_m)}{\bar{\delta}}d\tau \tag{6.46}$$

6.3 Experimental Result Validation

As part of the modeling verification process, the theoretical predictions were directly compared with the experimental results from Wachters and Westerling (1966). Figure 6.2 shows the time-dependent radius of the droplet during the impacting process. In their experiments water droplets, having an initial diameter of 2.3 mm, impacted on a flat and polished gold surface whose initial solid surface temperature is 400°C. The correlation between the two results is generally good. This analytical model accurately predicts the oscillation period and overall behavior of the experimental droplet. From Figure 6.2, it is apparent that the prediction is better at low Weber numbers. Furthermore the maximum collision time, defined as the time required for the circular water film to reach the maximum spreading diameter from the moment of collision with surfaces, has also found a good agreement between the theory and experiments.

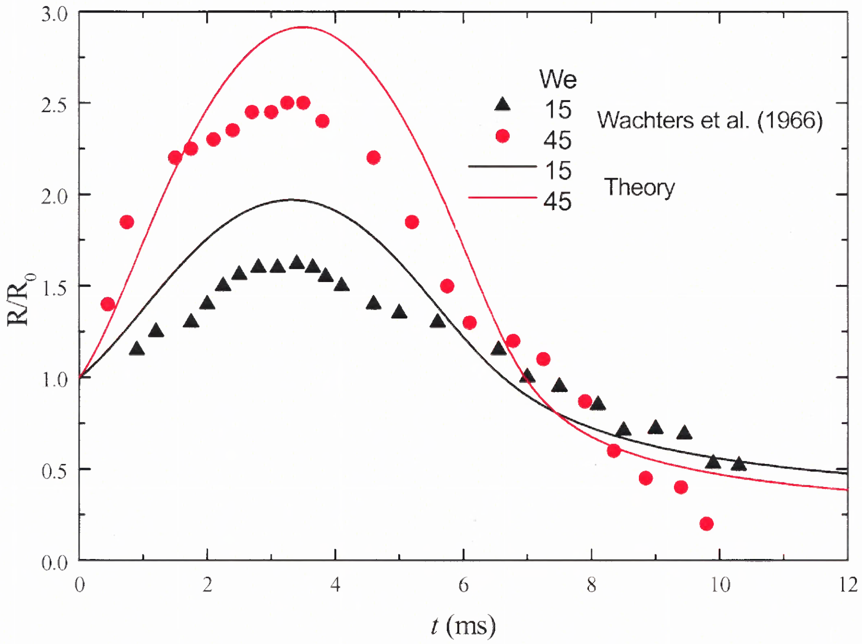

Figure 6.2 Time-dependent radius of the droplet during a Leidenfrost collision.

Hatta *et al.* (1997) proposed the experimental formula capable of predicting the maximum diameter of the droplet on the hot surface as a function of the Weber number alone,

$$R_{\max} / R_0 = 0.093 We^{0.74} + 1 \tag{6.47}$$

This formula has been verified with the reported experimental data obtained by other researchers (Ueda *et al.*, 1979; Akao *et al.*, 1980; Chandra and Avedisian, 1991).

Figure 6.3 shows that the theoretical results ($\chi = 50$) give a good fit to the experimental formula obtained by Hatta *et al.* (1997).

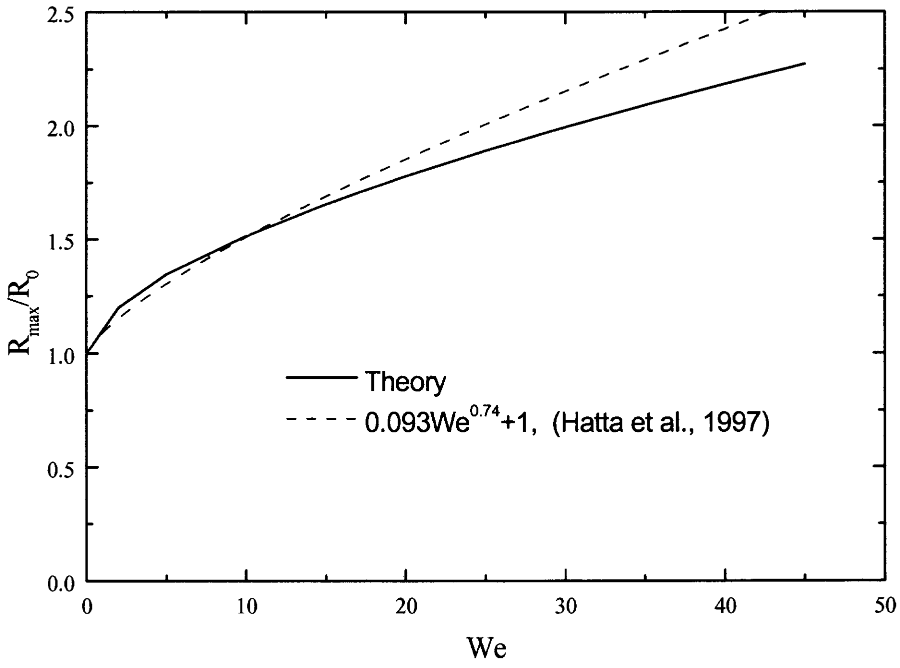

Figure 6.3 Relation between droplet maximum radius and Weber number.

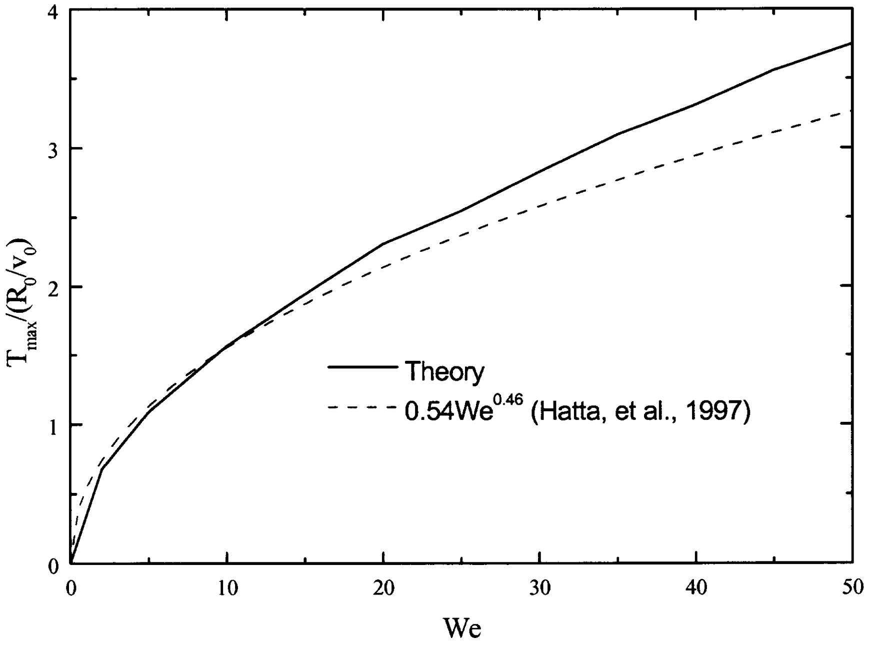

Figure 6.4 Relation between maximum collision time and Weber number.

For the maximum collision time, Hatta *et al.* (1997) also proposed an empirical formula to describe the relation between the maximum collision time and Weber number

$$\frac{T_{\max}}{\frac{R_0}{V_0}} = 0.54We^{0.46} \tag{6.48}$$

Figure 6.4 illustrates the comparison of the maximum collision time against the Weber number between Hatta's empirical formula and the theoretical model in this study. By the way, the solid line in this figure denotes the value estimated by theoretical model and the dash line represents the value calculated by Equation (6.48). The model prediction has also been found in a good agreement with their empirical formula, as seen in Figure 6.4. From these comparisons, the applicability of the collision model is verified.

Figure 6.5 shows the relationship between droplet evaporation ratio and the radius ratio of the particle and the droplet. It is noted that the droplet evaporation ratio increases along with the decrease of the solid size. It is because that when droplet-particle collision, in the convex case, the vapor could be escaped easier than in the flat case, as discussed in Chapter 1. The effect of curvature on particle temperature reduction is shown in Figure 6.6. From the size comparable droplet and particle multiple collisions, the particle temperature reduction is significant.

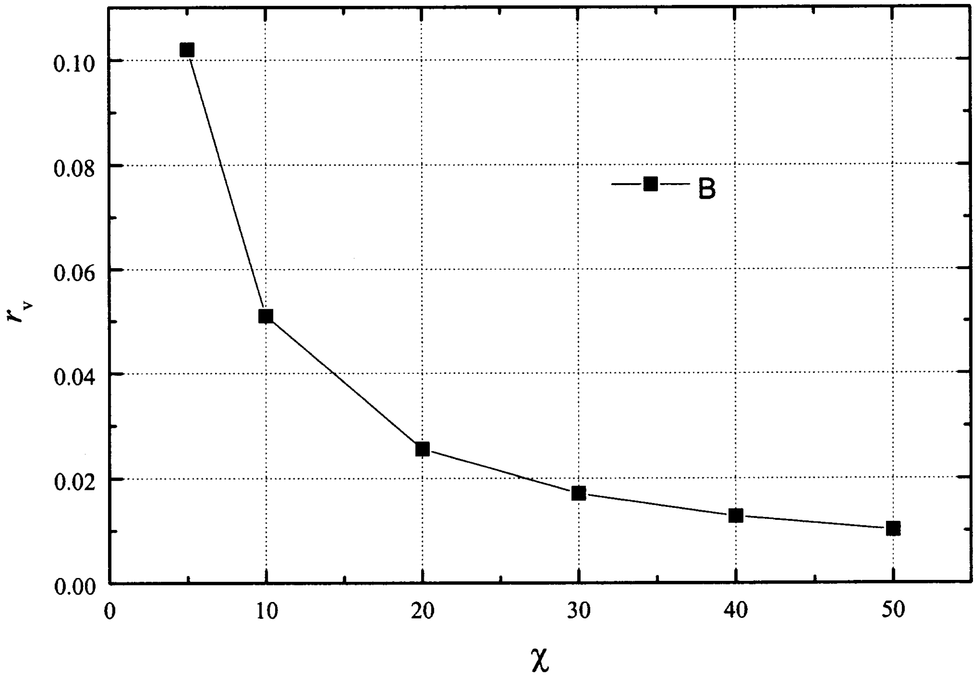

Figure 6.5 Relation between evaporation ratio and curvature ratio.

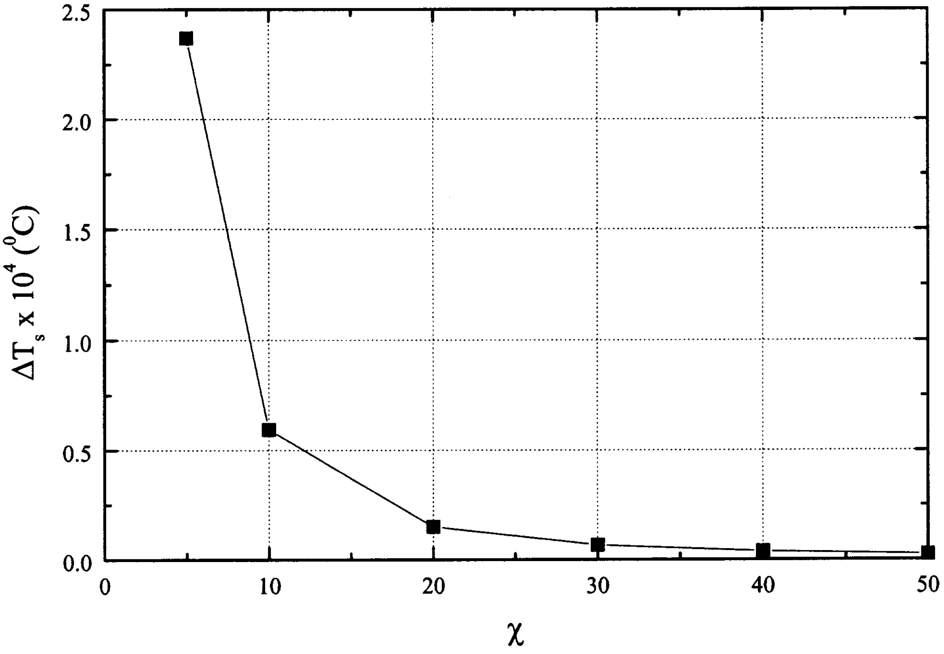

Figure 6.6 Relation between particle temperature reduction and curvature ratio.

6.4 Conclusions

In this chapter, an analytical model has been developed to describe the hydrodynamic and thermodynamic behavior of droplet-particle collision over Leidenfrost temperature. The whole collision process, the maximum collision time, the maximum deformation area, and the evaporation rate are simulated. Effects of solid curvature and Weber number on droplet collision process and droplet evaporation rate are illustrated. Modeling predictions are validated by existed flat experimental data.

CHAPTER 7

SUMMARY AND CONCLUSIONS

7.1 Introduction

A comprehensive study of evaporating spray jets into gas-solid flows has been performed in this study to investigate the fundamental characteristics of gas-liquid-solid three phases mixing including rapid phase change, phase-phase interactions, heat transfer, and mass transfer. The sudden expansion of the evaporated liquid results in an alteration in both gas and solid dynamics such as phase velocity, solid concentration, and solid agglomeration or clustering. Inversely, the introduction of solid particles provides large heat sources promoting evaporation and altering liquid-solid interactions. The liquid condensation and entrainment within the gas-solid flows further complicate the dynamics of three-phase interactions. In this study, both experimental study and theoretical analysis have been carried out to investigate fundamental mechanisms of evaporating spray jets in crossflow gas-solid flows.

In the experimental study, a laboratory-scaled circulating fluidized bed has been built to provide a continuous gas-solid flow. A laser/lamplight-assisted visualization system and a computerized temperature measurement system have been developed, which enables the measurement of spray trajectories and temperature distributions of mixture phases in both dilute and dense gas-solid flows. All the experiments have been performed with FCC particles and well-defined liquid nitrogen sprays. The spray trajectory, spray penetration length, and flow pattern are investigated both experimentally and theoretically. The geometric and operating parameters, such as nozzle type, nozzle size, injection angle, jetting velocity, and solid loading are studied in the experiments.

A fundamental parametric model of an oblique evaporating spray injecting into a gas-solid flow has also been developed, which takes into account of the three-phase interactions with phase changes. The model can predict the effects of spray parameters on the mixing characteristics such as spray penetration length, temperature and velocity of each phase, trajectories, and the phase volume fraction distributions.

Droplet evaporation rate is the most important factor to affect the phase interactions of the spray jets in gas-solid flows. In applications of evaporating sprays injecting into gas-solid suspension flows, the main thermal energy for droplet evaporation comes from collisions between droplets and particles with a temperature beyond the Leidenfrost temperature. An analytical model has been developed to describe the Leidenfrost collision between a droplet and a hot solid sphere. The whole collision process, the maximum collision time, the maximum deformation area, and the evaporation rate are simulated in this model. Effects of solid curvature and Weber number are illustrated.

7.2 Major Contribution and Findings

During and after the study of evaporating spray jets in gas-solid flows, many interesting phenomena came up, such as the effect of solid loading on spray structure, the effect of injection angle on spray structure, and the dilution phenomenon of solid concentration in the spray region.

7.2.1 Evaporating Spray Jets in Gas-Solid Flows

The major contributions and finding of evaporating spray jets in gas-solid flows are:

(1) Visualized behavior of evaporating spray jets in dilute gas-solid flows.

(2) Measured the temperature distribution of three-phase mixture near the spray region, which is exceptionally important for the validation of the fundamental model of spray jets in gas-solid flows.

(3) Combined the visualization technique and temperature measurement technique. The comparison of the visualization images and temperature distribution is coincided.

(4) Developed an extensive parametric model of evaporating liquid spray jet evaporation in gas-solid suspension flows, which includes all phase interactions with phase changes in the three phases. The predictions of theoretical model were found to be in good agreement with the experimental results.

(5) Discovered experimentally, explained and predicted theoretically that solids loading can significantly affect the hydrodynamics of the spray, such as the shortening effect on spray penetration length and the speeding effect on spray evaporation rate.

(6) Parametric effects on the mixing characteristics such as penetration length, temperature and velocity of each phase, trajectories, and the phase volume fraction distributions are illustrated. It is found that the penetration length is shortened in the presence of particles in a liquid spray jet of any injection angle. The penetration length decreases with the increase of solids loading. Effects of

spray injecting angle, diameter of nozzle tip, and liquid volume fraction at nozzle tip on both spray trajectory and penetration are also illustrated in this study

7.2.2 Droplet-Particle Collision over Leidenfrost Temperature

The major contributions and findings in the Leidenfrost collision between a droplet and hot solid sphere are:

(1) Derived a new analytical model to successfully simulate the entire collision process with the consideration of particle curvature and limited particle thermal capacity.

(2) Derived the time dependent bounce force in the vapor layer with the consideration of solid curvature, which can be mathematically reduced to a droplet – plate collision.

(3) Predicted the maximum collision time, the maximum deformation area, droplet evaporation rate, and the solid temperature reduction upon a single collision.

7.3 Suggested Future Research Directions

The fundamental mechanisms of either an evaporating spray in a gas-solid flow or the droplet-particle collision over Leidenfrost temperature are far from being fully understand. Hence, in this section, some research topics are suggested to further study these phenomena. Section 7.3.1 will give some discussion regarding the possible research direction on evaporating sprays in gas-solid flows. Then the suggested future research topics on droplet hot surface collision will be given in Section 7.3.2.

7.3.1 Evaporating Spray Jets in Gas-Solid Flows

There are many unknowns in the study of evaporating spray jets in gas-solid flows, which need extensive experimental investigations. One type of very much desired information is the 3-D distribution of solids concentration, which might be detected by a direct measurement such as isokinetic sampling technique or indirect identification such as sampling and analysis the vapor component. Multiple spray jets interaction encountered in many industrial applications is another interesting research topic. In order to investigate the multiple spray interaction, one of the possible ways is to inject different types of liquids that are easily identified.

In most important chemical processes, the phenomenon of spray jets into gas-solid flows is related to chemical reactions. Therefore including the effect of chemical reaction in the theoretical model of spray jets is extremely important. Furthermore, the parametric model in this study is limited to a circular nozzle tip. Spray jet nozzle structure can significantly affect the spray structure and phase mixing (Srinivasan *et al.*, 1984). In practical applications, many different shaped nozzles are used to achieve different spray structures. Thus, more attentions may be focused for nozzle types during theoretical studies. Finally, the entrainment velocity of particles is definitely different with that of gases. For this slip effect, both experimental measurement and theoretical study should be carried out.

7.3.2 Droplet-Particle Collision over Leidenfrost Temperature

Very useful collision experiments could be performed using water mists and a hot particle collision under the micro-gravity environment. It is noted that the Leidenfrost collision and associated heat and mass transfer processes are greatly complicated by the coupling effects of natural heat convection and the gravitational force affecting the droplet and particle trajectories. Therefore, the development of theoretical models in which the gravity-induced phenomena are neglected calls for unambiguous and adequate experimental data. The microgravity environment provides an ideal opportunity to realize such experiments.

Another suggested research topic is to study the collision of liquid droplet with porous particles. There are lots of applications in various industries, such as FCC process in petroleum industry where the FCC catalysts are porous. If the solid particle is porous, the porous structure will allow some vapor penetration into the solid, hence reducing the thickness of the boiling film and enhancing the evaporation. Thus, with the increased porosity, the Leidenfrost temperature can be significantly elevated.

APPENDIX A

TEMPERATURE REULTS IN 25° INJECTION

The results of 0%, 0.5%, 1.3%, 2.5%, and 3.7% solid volume fraction are shown in Figures A.1 to A.5, respectively.

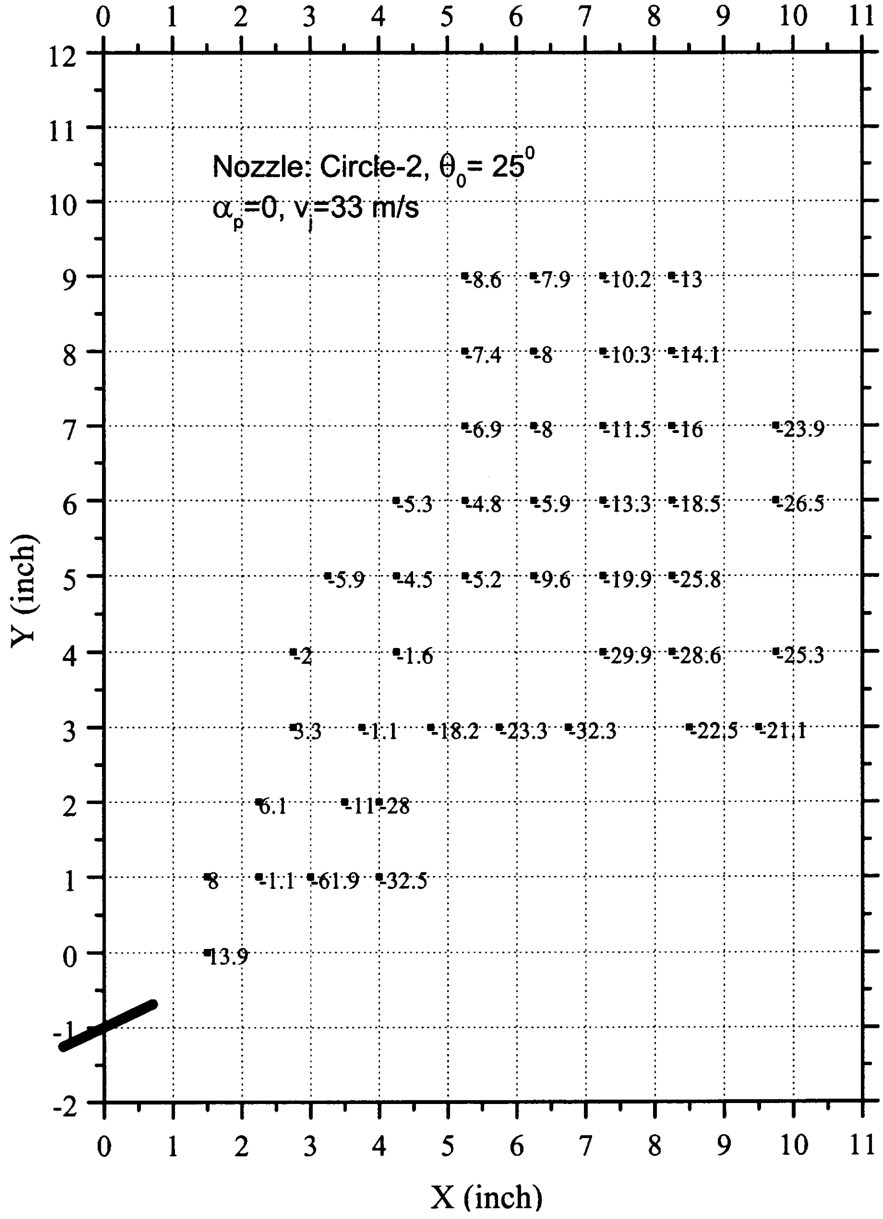

Figure A.1 Temperature distribution of circle-2 nozzle at 0% solid loading.

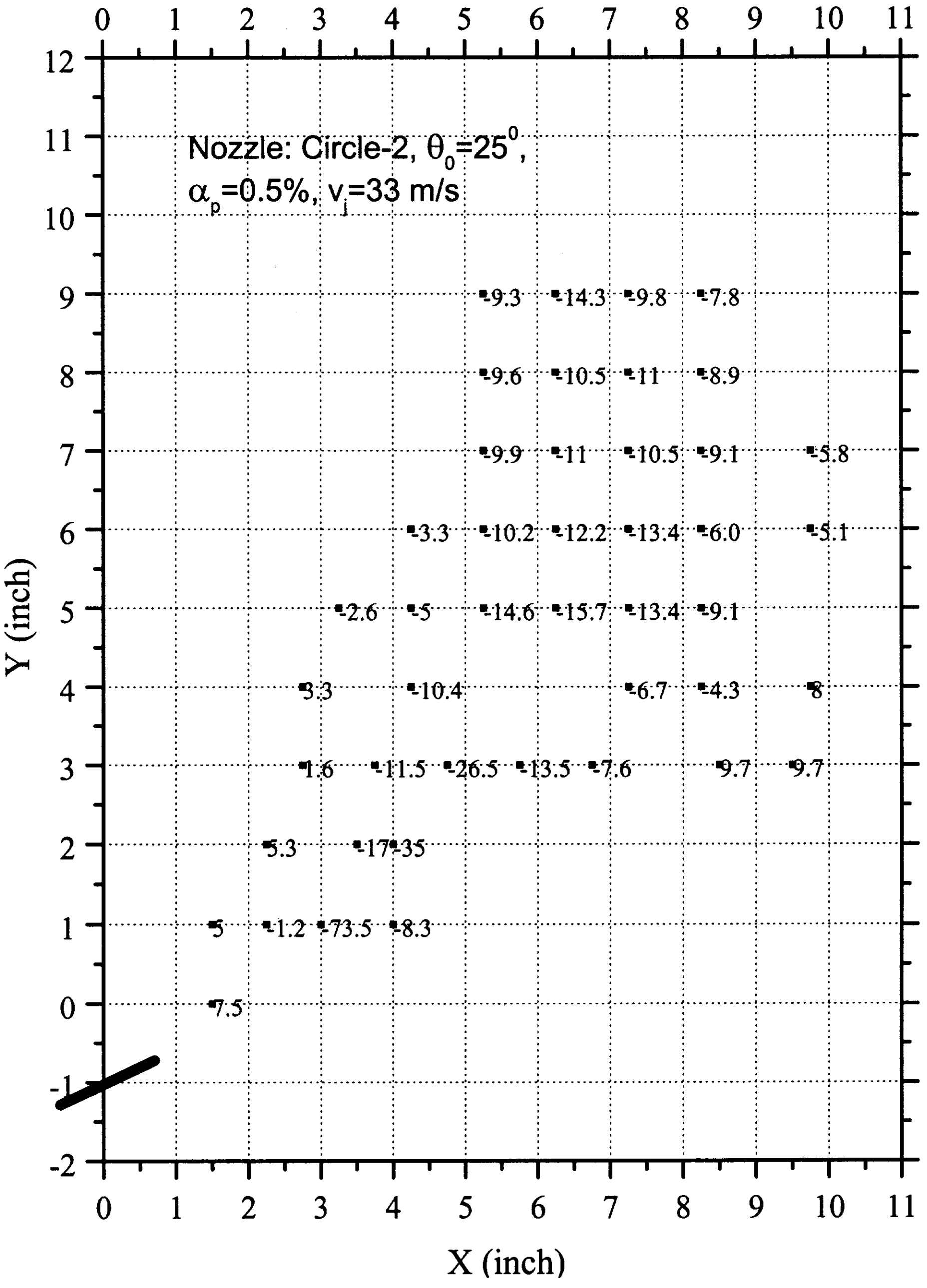

Figure A.2 Temperature distribution of circle-2 nozzle at 0.5% solid loading.

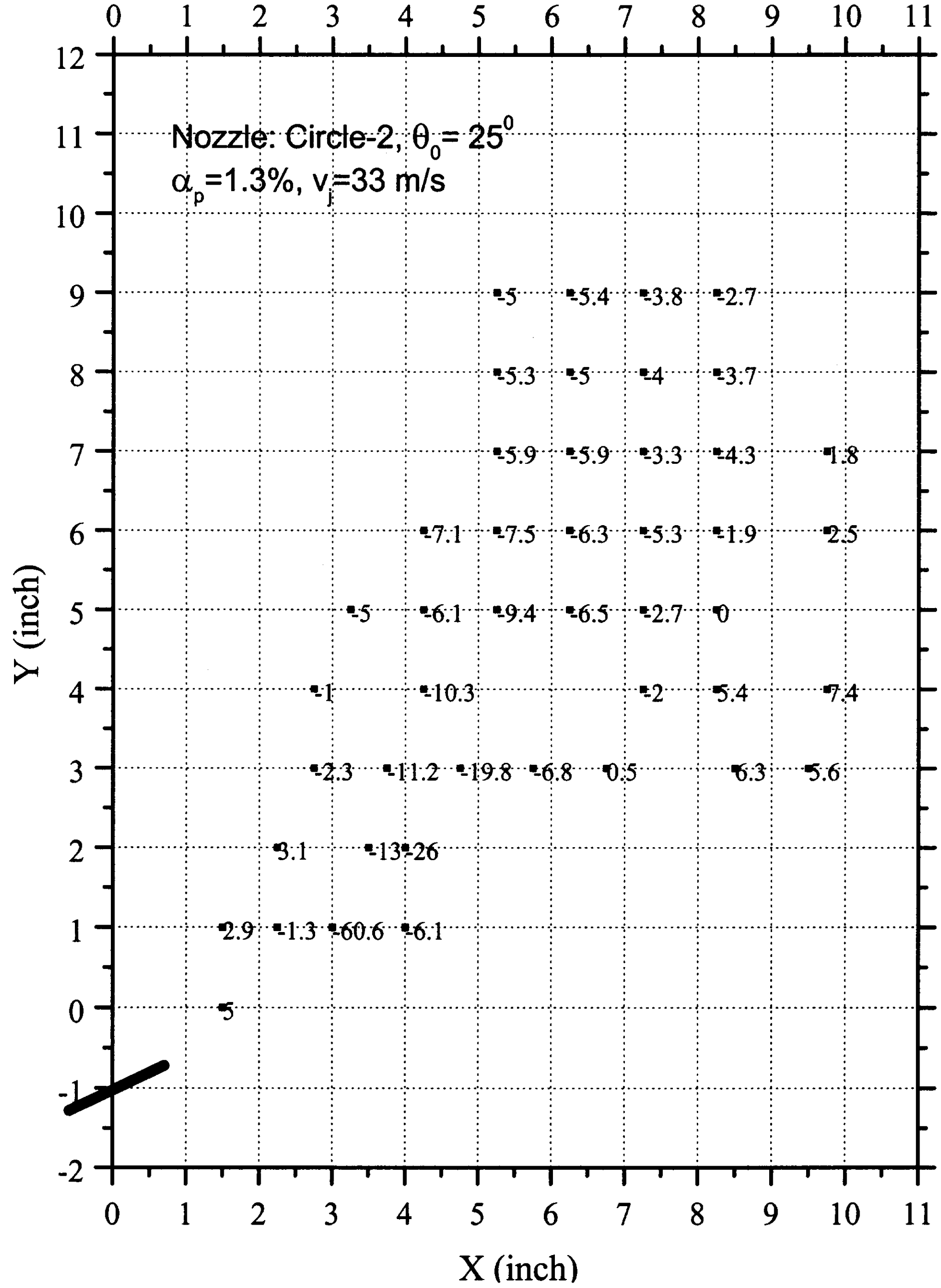

Figure A.3 Temperature distribution of circle-2 nozzle at .3% solid loading.

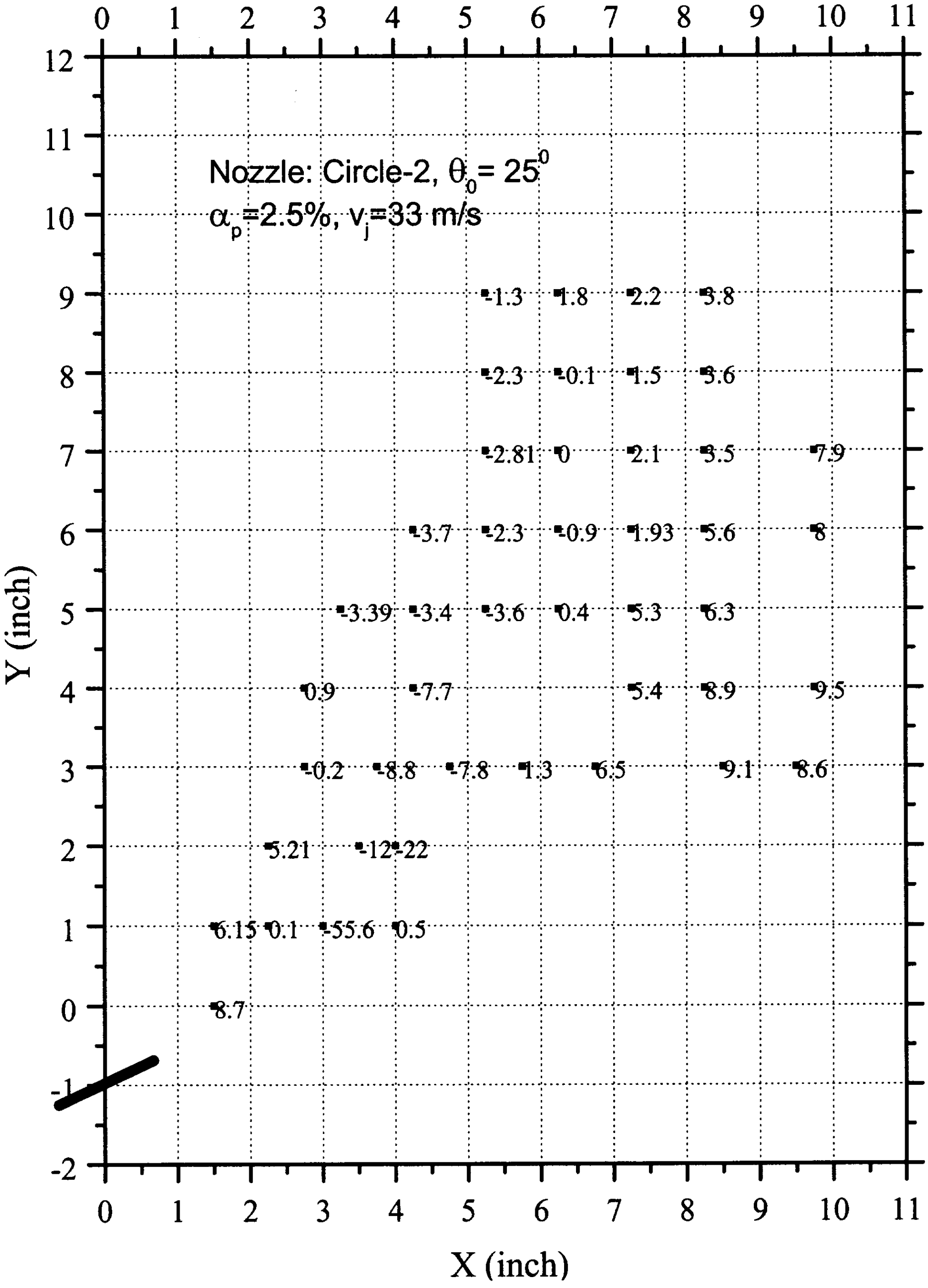

Figure A.4 Temperature distribution of circle-2 nozzle at 2.5% solid loading.

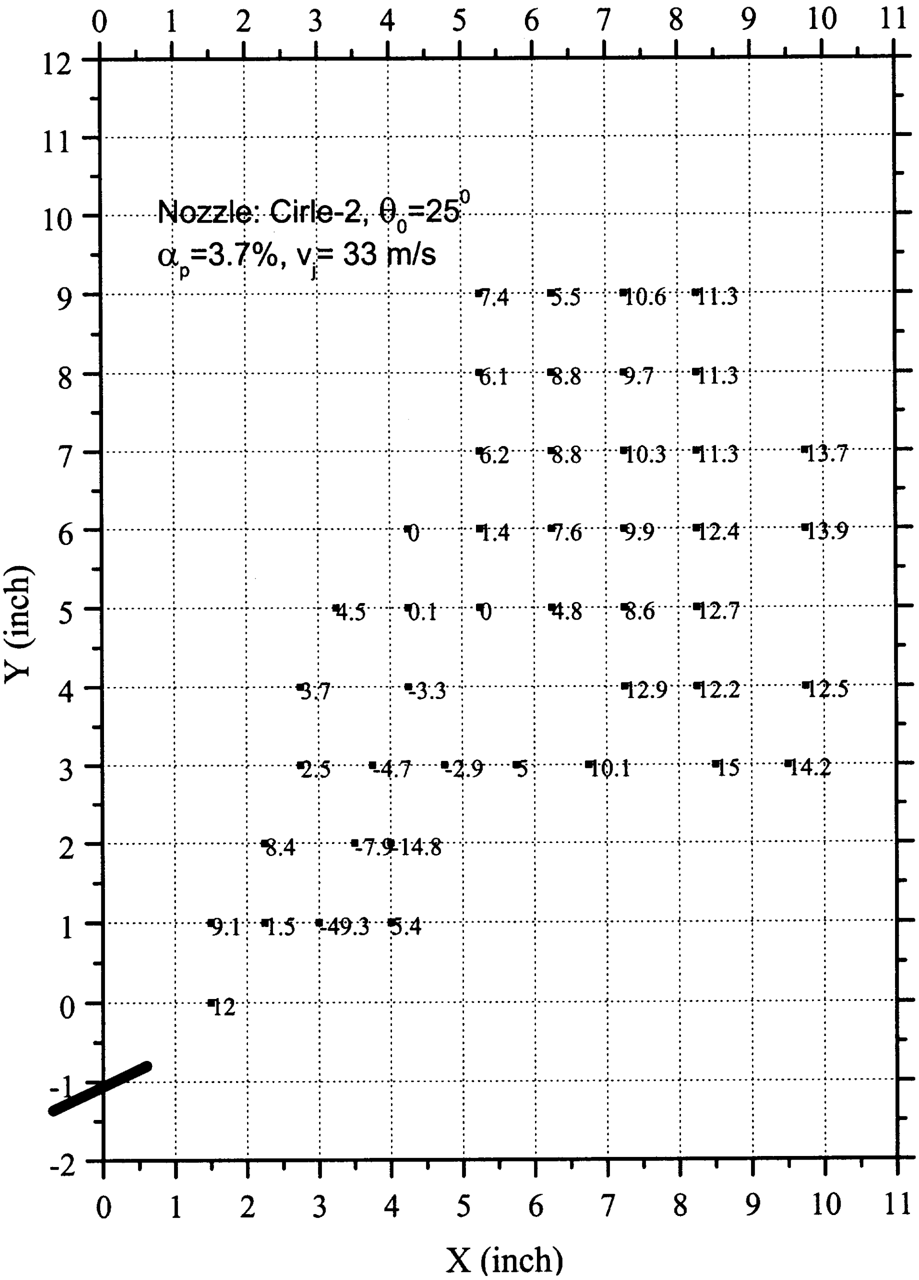

Figure A.5 Temperature distribution of circle-2 nozzle at 3.7% solid loading.

APPENDIX B

TEMPERATURE RESULTS IN -30° INJECTION

The results of 0%, 0.5%, 1.3%, and 2.5% solid volume fraction are shown in Figures B.1 to B.4, respectively.

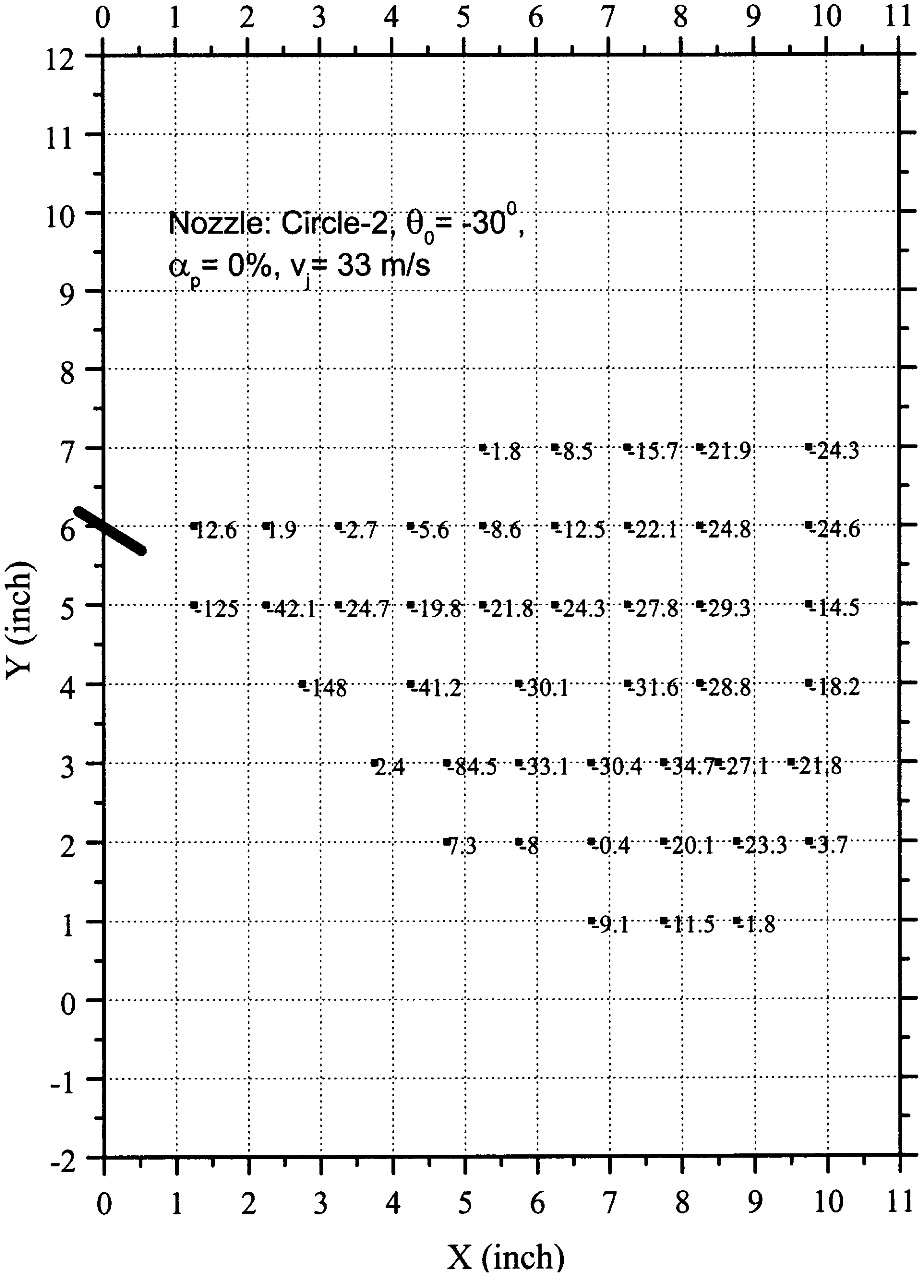

Figure B.1 Temperature distribution of circle-2 nozzle at 0% solid loading.

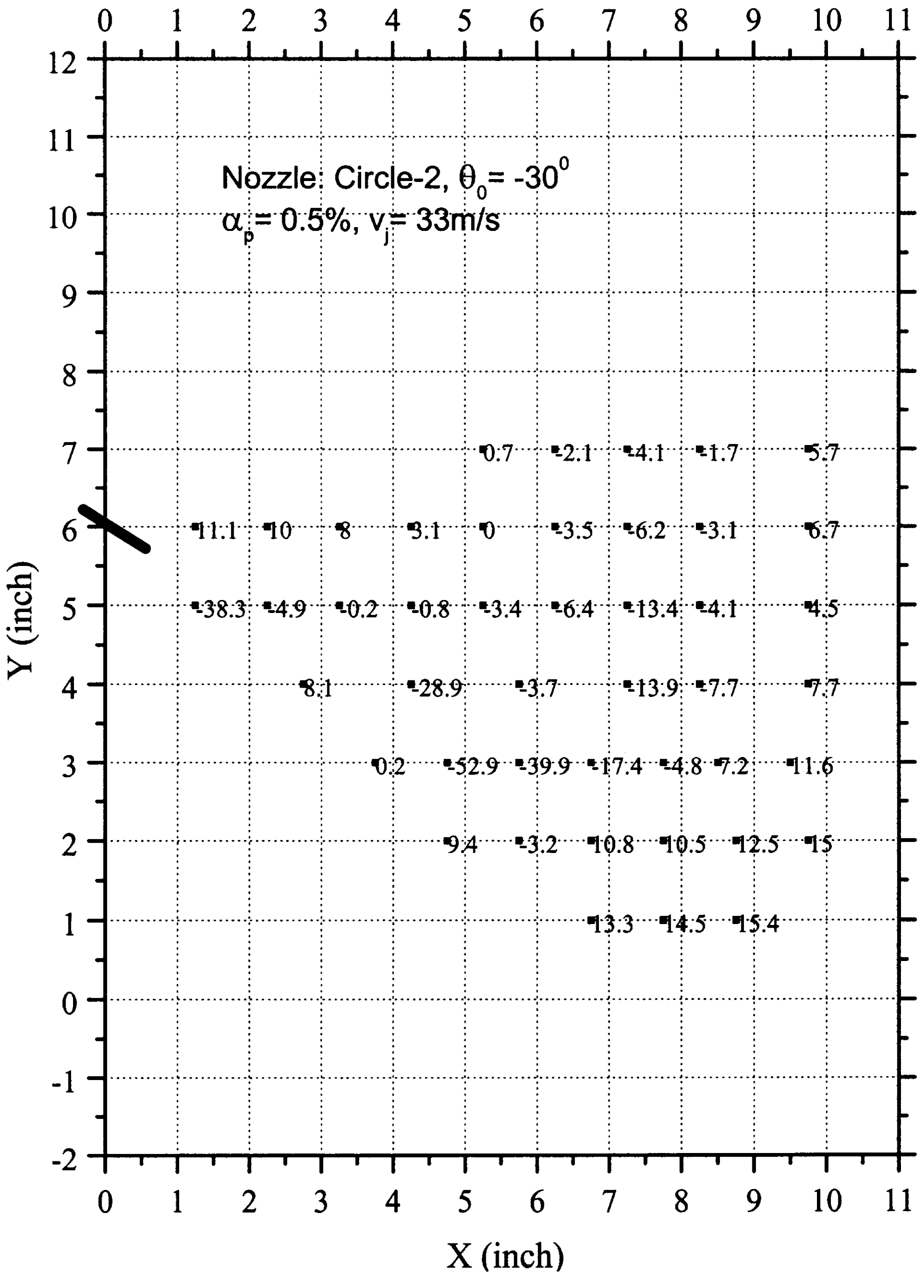

Figure B.2 Temperature distribution of circle-2 nozzle at 0.5% solid loading.

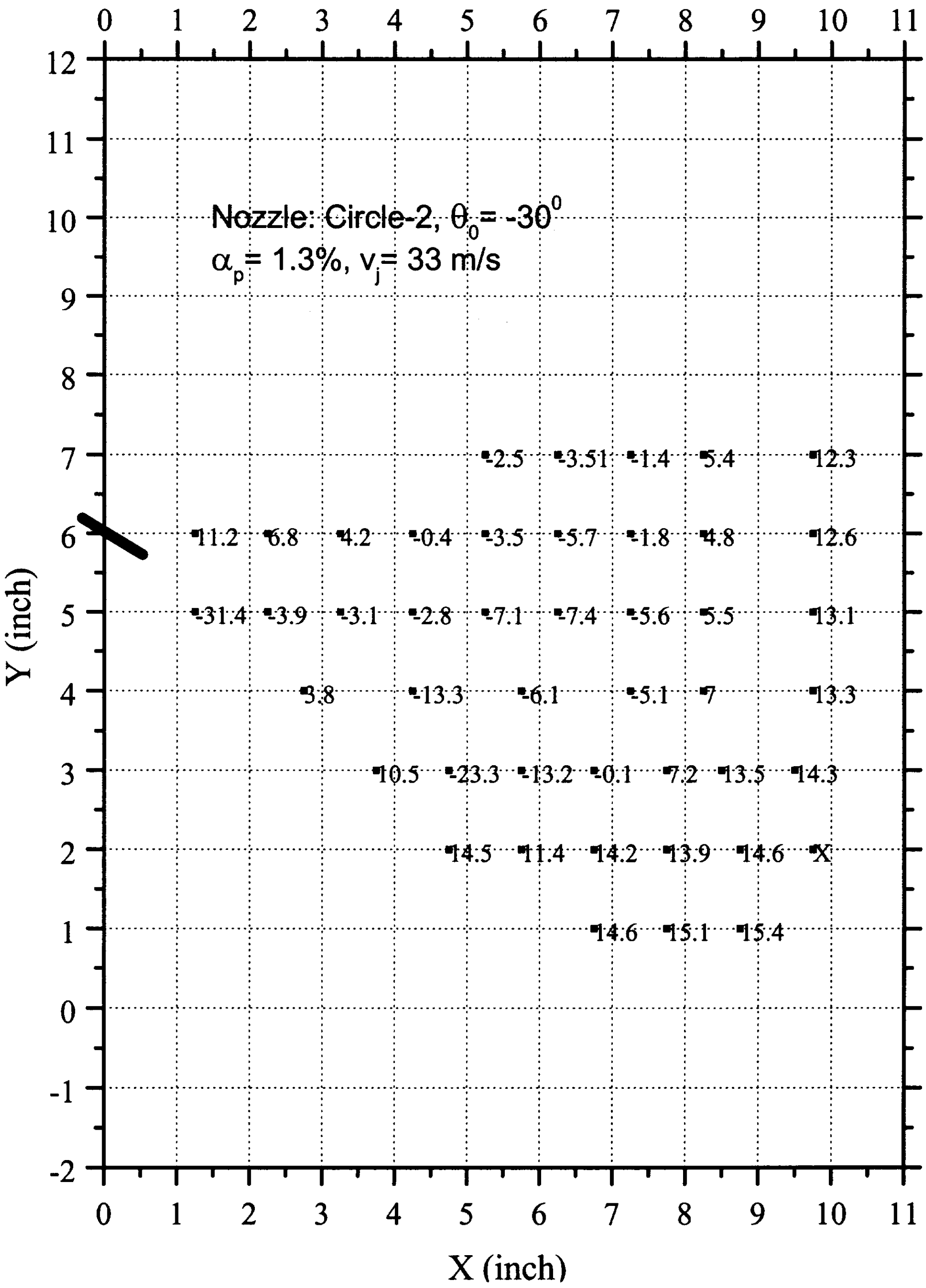

Figure B.3 Temperature distribution of circle-2 nozzle at 1.3% solid loading.

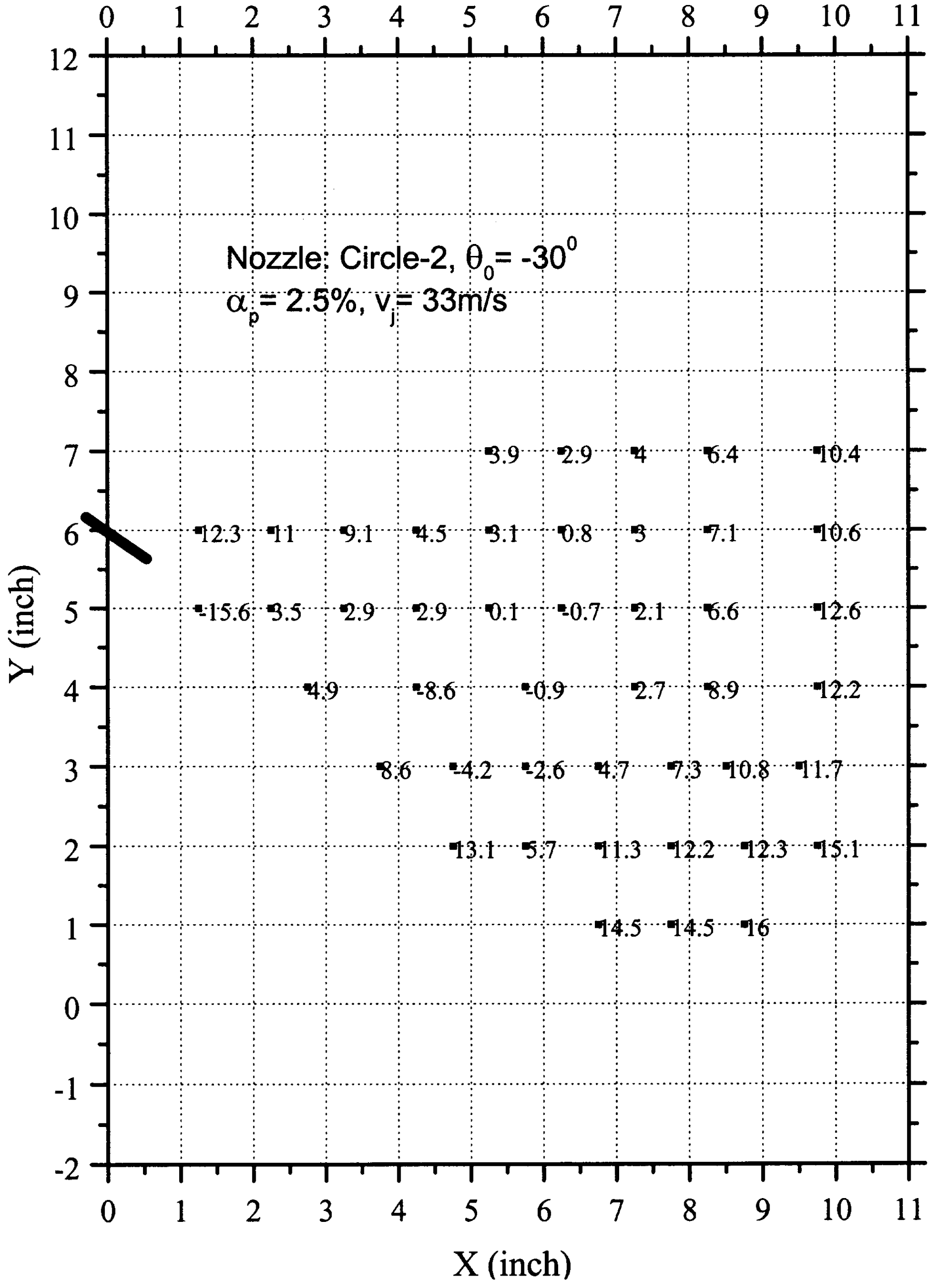

Figure B.4 Temperature distribution of circle-2 nozzle at 2.5% solid loading.

REFERENCES

Abramovich, G.N., 1963. The theory of turbulent jets. M.I.T. Press, MA (English translation).

Akao, E., Araki, K., Mori, S., and Moriyama, A., 1980. Deformation behaviors of a liquid droplet impinging onto hot metal surface. Trans. Int. Steel Inst. Japan, 20, pp. 737-743.

Anders, K., Roth, N., and Frohn A., 1993. The velocity change of ethanol droplets during collision with a wall analyzed by image processing. Experiments in Fluids, 15, pp. 91-96.

Avedisian, C.T. and Koplik, J., 1987. Leidenfrost boiling of methanol droplets on hot porous/ceramic surfaces. International Journal of Heat and Mass Transfer, 30, pp. 379-393.

Bazile, R. and Stepowski, D., 1994. 2D laser diagnostics of liquid methanol for investigation of atomization and vaporization dynamics in a burning spray jet. Symposium on Combustion Proceedings of the 25th Symposium on Combustion, p. 363.

Bernardin, J.D., Stebbins, C.J., and Mudawar, I., 1997. Mapping of impact and heat transfer regimes of water drops impinging on a polished surface. Int. J. Heat Mass Transfer, 40, pp. 247-267.

Bolle, L and Moureau, J.C., 1976. Spray cooling of hot surfaces. Multiphase Science and Technology, Hemisphere, New York, p. 1092.

Bussmann, M., Chandra, S., and Mostaghimi, J., 1997. Droplet impact on arbitray surface geometries. Proceeding of ASME Fluids Engineering, FEDSM97, p. 3073.

Buyevich, YU.A. and Mankevich, V.N., 1995. Interaction of a dilute mist flow with a hot body. Int. J. Heat Mass Transfer, 38, pp. 731-744.

Buyevich, YU.A., Mankevich, V.N., and Polotsky, M.I., 1986. Toward the theory of fall of a droplet onto an overheated surface. Teplofiz. Vysok. Temp., 24, pp. 743-752.

Campbell, J.F. and Schetz, J.A., 1973. Flow properties of submerged heated effluents in a waterway, AIAA Journal, 15, p. 223.

Chandra, S. and Avedisian, C.T., 1991. On the collision of a droplet with a solid surface. Proc. R. Soc. Lond., A 432, pp. 13-41.

Chandra, S. and Avedisian, C.T, 1992. Observations of droplet impingement on a ceramic porous surface. Int. J. Heat Mass Transfer, 35, pp. 2377-2388.

Chang, S. L., Lottes, S.A., Zhou, C.Q., and Petrick, M., 1996. Evaluation of multi-phase heat transfer and droplet evaporation in petroleum cracking flows. Proceeding of ASME Heat Transfer Division, 4, pp. 17-27.

Chang, S. L., Lottes, S.A., Golchert, B., and Petrick, M., 1998. Interaction of multi-phase hydrodynamics, droplet evaporation, and chemical kinetics in FCC riser reactions. AIAA/ASME Joint Thermophysics and Heat Transfer Conference, pp. 261-269.

Chen, T.H., Roe, L.A., and Nejad, A.S., 1994 Multifunction droplet imaging and Velocimetry system for spray jets. J. Propulsion and Power, 10, p. 798.

Chen, J.C. and Hsu, K.K., 1995. Heat transfer during liquid contact on superheated surfaces. Journal of Heat Transfer, 117, pp. 693-697.

Chen, X.-Q. and Pereira, J.C.F., 1995. Prediction of evaporating spray in anistropically turbulent gas flow. Numerical Heat Transfer, Part A, 27, pp. 143-162.

Chen, X.-Q. and Pereira, J.C.F., 1996. Computation of turbulent evaporating sprays with well-specified measurements: a Sensitivity Study on Droplet Properties. International Journal of Heat and Mass Transfer, 39 (3), pp. 441-454.

Dear, J.P. and Field, J.E., 1988. High-speed photography of surface geometry effects in liquid/solid impact. J. Appl. Phys., 63, pp. 1015-1021.

D'souza R. and Forney L. J., 1990. Slow bimolecular reactions in a deflected turbulent jet. Chemical Engineering Journal, 43, pp. 127-136.

Dubrovsky, V.V., Podvysotsky, A.M., and Shraiber, A.A., 1992. Particle interaction in the three-phase polydisperse flows. International Journal of Multiphase Flow, 18 (3), pp. 337-352.

Dwyer, H.A., 1985. Progress Energy Combustion Science, 15, p. 131.

Edelman R.B., Economos, C., and Boccio, J., 1971. Mixing and combustion in two-phase flows with application to the boron-oxygen-hydrogen-nitrogen system. AIAA Journal, 9, p. 1935.

Fan, L.-S. and Zhu, C., 1998. Principles of gas-solid flows. Cambridge University Press, Cambridge, p. 172.

Field, M.A., 1963. Entrainment into an air jet laden with particles. BCURA Inf., p. 273.

Filla M., Massimilla, L., and Vaccaro, S., 1983. Gas jets in fluidized beds: the influence of particle size, shape and density on gas and solids entrainment. Int. J. Multiphase Flow, 9 (3), pp. 259-267.

Forney, L.J., Kwon, T.C., 1979. Efficient single-jet mixing in turbulent tube flow. AIChE Journal, 25 (40), pp. 623-630.

Fujimoto, H. and Hatta, N., 1996. Deformation and rebounding processes of a water droplet impinging on a flat surface above the Leidenfrost temperature. Trans. ASME J. Fluids Eng., 118, pp. 142-149.

Fukai, J., Zhao, Z., Poulikakos, D., Megaridis, C.M., and Miyatake, O., 1993. Modeling of the deformation of a liquid droplet impinging upon a flat surface. Phys. Fluids A5, p. 2588.

Gavalses M, Theodorakakos, A., Bergeles, G., and Breon, G., 1996. Evaluation of the effect of droplet collisions on spray mixing. Proceedings of the Institution of Mechanical Engineers, Part C: Journal of Mechanical Engineering Science, 210 (5), pp. 465-475.

Gawronski, R. and Roszak, J., 1979. Drop sizes in liquid-liquid co-current flow through fluidized beds. Inz. Chem., 9, pp. 88-98.

Gu, W., 1995. Evaporation of liquid droplets in superheated gas/particle flows. Ph.D. Dissertation, Lehigh University.

Han, K.S. and Chung, M.K., 1992a. Numerical simulation of a two-phase gas-particle jet in a cross flow. Aerosol Science Technol., 16, p. 126.

Han, K.S. and Chung, M.K., 1992b. Numerical simulation of a two-phase gas-particle jet in a cross flow, part 2. Free stream velocity gradient and heat transfer mechanism. Aerosol Science Technol., 17, p. 59.

Harlow, F.H. and Shannon, J.P., 1967. The splash of a liquid drop. J. Appl. Phys., 38 (10), pp. 3855-3866.

Hatta, N., Fujimoto H. and Takuda, H., 1993. Numerical analysis of flow pattern of impinging liquid sprays in a cold model for cooling a hot plate. Applied Scientific Research, 50, pp. 129-147.

Hatta, N., Fujimoto H. and Takuda, H., 1995. Deformation process of a water droplet impinging on a solid surface. Trans. ASME J. Fluids Eng., 117, pp. 394-401.

Hatta, N., Fujimoto H. and Takuda, H., 1997. Deformation process of a droplet impinging on a hot oxide-scaled surface above the Leidenfrost temperature. Steel Research, 68 (1), pp. 15-19.

Hatta, N., Fujimoto, H., Kinoshita, K., and Takuda, H., 1997. Experimental study of deformation mechanism of a water droplet impinging on hot metallic surfaces above the Leidenfrost temperature. Journal of Fluids Engineering, 119 (3), pp. 692-699.

Huang L.S. and Yao S.C., 1999. Experimental investigation of the impaction of water droplets on cylindrical objects. International Journal of Multiphase Flow, 25, pp. 1545-1559.

Ibrahim, E.A. and Marshall, S.O., 2000. Instability of a liquid jet of parabolic velocity profile, Chemical Engineering Journal. 76, pp. 17-21.

Inada, S. Miyasaka Y. and Nishida, K., 1985. Transient heat transfer for a water droplet impinging on a heated surface. Bull. JSME, 28, pp. 2675-2681.

Jenkins J.M., Jones, R.L., Jones, T.M., and Beret, S., 1986. Method for fluidized bed polymerization. U.S. Patent 4,588,790.

Johnsson H. and Johnsson, F., 2001. Measurements of local solids volume-fraction in fluidized bed boiler. Powder Technology, 115, pp. 13-26.

Karl, A., Rieber, M., Schelkle, M., Anders, K., and Frohn, A., 1996. Comparison of new numerical results for droplet wall interactions with experimental results. Proceedings of the ASME Fluids Engineering Summer Meeting, 236, pp. 201-206.

Karl, A. and Frohn, A., 2000. Experimental investigation of interaction processes between droplets and hot walls. Physics of Fluids, 12, pp.785-796.

King D., 1992. Fluidized catalytic crackers: an engineering review, in: D. Potter, D. Nicklin (Eds.), Fluidization VII. Engineering Foundation, New York.

Kouremenos D., Pantzas, C., Panagakls, G., and Krikkls, R., 1995. Vaporization behaviour of fuel droplets in a gas turbine combustor. Thermodynamics and the Design, Analysis, and Improvement of Energy Systems, 35, pp. 261-273.

Lasheras J. C., Villermaux, E., and Hopfinger, E. J., 1998. Break-up and atomization of a round water jet by a high-speed annular air jet. J. Fluid Mech., 357, pp. 351-379.

Lee, L.Y.W., Chen, J.C., and Nelson, R.A., 1985. Liquid-solid contact measurements using a surface thermocouple temperature probe in atmospheric pool boiling water. Int. J. Heat Mass Transfer, 28, pp. 1415-1423.

Leidenfrost, J.G., 1756. *De aquaea communis nonnullis qualitatibus tractatus.*

Levin, A. and Hobbs, P.V., 1971. Splashing of water drops on solid and wetted surfaces: Hydrodynamics and charge separation, Phil. Trans, R. Soc. London A, 269, pp. 555-585.

Levy, Y. and Lockwood, F.C., 1981. Velocity measurements in a particle laden turbulent free jet. Combustion and Flame, 40, p. 333.

Lew, J.K., Montague, D.C., Pruppacher, H.R., and Rasmussen, R.M., 1986. A wind tunnel investigation on the riming of snow flakes. Part I: Porous disks and large stellars. J. Atmos. Sci., 43, pp. 2392-2409.

Li, H.S. and Karagozian, A.R., 1990. Breakup of a liquid jet in supersonic crossflow. AIAA Journal, 30 (7), pp.1919-1921.

Liu, H., Lavernia, E.J., and Rangel, R.H., 1993. Numerical simulation of substrate impact and freezing of droplets in plasma spray processes. J. Phys. D Appl. Phys., 26, p. 1900.

Makino, K. and Michiyoshi, I., 1984. The behavior of a water droplet on heated surfaces. Int. J. Heat Mass Transfer, 27, pp. 781-791.

Makino, K. and Michiyoshi, I., 1987. Discussion of transient heat transfer to a water droplet on heated surfaces under atmospheric pressure. Int. J. Heat Mass Transfer, 30, pp. 1895-1905.

Memmot, V. J. and Smoot, L. D., 1978. Cold flow mixing rate data for pulverized coal reactors. AICHE Journal, 24, pp. 466-473.

Naber, J.D. and Farrell, P.V., 1993. Hydrodynamics of droplet impingement on a heated surface. SAE technical paper, 930919.

Newton D., 1998. How BP makes use of its X-ray imaging facility to support developments in fluidized bed processes. Proc. AIChE Annu. Meeting, p. 221.

Pedersen, C.O., 1970. An experimental study of the behavior and heat transfer characteristics of a water droplet impinging upon a heated surface. Int. J. Heat Mass Transfer, 13, pp. 369-381.

Peter E.M., Takimoto, A., and Hayashi, Y., 1994. Flashing and shattering phenomena of superheated liquid jets. JSME International Journal, Series B, 37(2), pp. 313-321.

Platten J. L. and Keffer, J. F., 1968. Entrainment in deflected axisymmetric jets at various angles to the stream. Tech. Rep. 6808, Department of Mechanical Engineering, Univ. of Toronto.

Putnam, A., 1961. Integrable form of droplet drag coefficient. ARS Journal, 31, pp. 1467-1468.

Rajaratnam N., 1976. Turbulent jets (Chapter 9). Elsevier Science.

Ricou, F.P. and Spalding, D.B., 1961. Measurements of entrainment by axisymmetrical turbulent jets. Journal of Fluid Mechanics, 11, pp. 21-32.

Rudinger, G., 1975. Some aspects of gas-particle jets in a cross flow. ASME Paper 75-WA/HT-5.

Salzman, R.N. and Schwartz, S.H., 1978. Experimental study of a solid-gas jet issuing into a transverse stream. J. Fluids Eng., 100, p. 333.

Senda, J. Yamada, K., Fujimoto, H., and Miki, H., 1988. The heat transfer characteristics of a small droplet impinging upon a hot surface. JSME Int. J., 31, pp. 105-111.

Shinichi, Yuu, Yasukouchi, N., Hirosawa, Y., and Jotaki, T., 1978. Particle turbulent diffusion in a dust laden round jet. AIChE J., 24, p. 509.

Shoji, M., Wakunaga, T., and Kodama, K., 1984, Trans. JSME 50B, p. 716.

Silverman, I. and Sirignano, W.A., 1994. Multi-droplet interaction effects in dense sprays. International Journal of Multiphase Flow, 20(1), pp. 99-116.

Sirignano, W.A., 1999. Fluid Dynamics and Transport of Droplets and Sprays. Cambridge University Press.

Skouby, D. C., 1998. Hydrodynamics Studies in a 0.45-m Riser with Liquid Feed Injection. Proc. AIChE Annu. Meeting, p. 238.

Srinivasan, R., Coleman, E., and Johnson, K., 1985. Dilution jet mixing program phase II report. NASA CR-174624.

Sommerfeld, M. and Qiu, H.-M., 1995. Particle concentration measurements by Phase-doppler Anemometry in complex disperesed two-phase flows. Experiments in Fluids, 18(3), pp. 187-198.

Subramanian, V., 1982. Entrainment by a concentric jet with particles in the primary stream. Letters in Heat and Mass Transfer, 9, pp. 277-290.

Subramanian, V., 1982. Entrainment by a concentric jet with particles in the secondary stream. The Canadian Journal of Chemical Engineering, 60, pp. 589-592.

Subramanian, V. and Raman, N., 1983. The fully developed region of a two-phase jet. Int. Comm. Heat Mass Transfer, 10, pp. 413-420.

Subramanian, V. and Ganesh, R., 1984. Influence of free stream velocity on the entrainment by single- and two-phase axisymmetric jets. AICHE Journal, 30 (8), pp. 1010-1013.

Subramanian, V. and Raman, N., 1984. Measurement of velocity and concentration for a two-phase turbulent jet. The Canadian Journal of Chemical Engineering, 62, pp. 314-318.

Subramanian, V. and Venkatram, S., 1985. Particle entrainment by axisymmetric jets. The Canadian Journal of Chemical Engineering, 63, pp. 853-855.

Tamura, Z. and Tanasawa, Y., 1959. Evaporation and combustion of a drop contacting with a hot surface. 7th Intl Symp. on Combustion, pp. 509-522.

Tatterson, D.F., Marker, T.L., and Forgac, J.M., 1987. Particle effects on free jet entrainment. The Canadian Journal of Chemical Engineering, 65, pp. 361-365.

Ted, G., 1998. Landmark Reactor: Exxon's Baton Rouge refinery is home to the world's first fluid catalytic cracking units, which revolutionized the oil industry, The Advocate, November 8.

Tsuji, Y., Morikawa, Y., Tanaka, T., and Karimine, K., 1988. Measurement of an axisymmetric jet laden with coarse particles. Int. J. Multiphase Flow, 14 (5), pp. 565-574.

Tsurutani, K., Yao, M., Senda, J., and Fujimoto, H., 1990. Numerical analysis of the deformation process of a droplet impinging upon a wall. JSME Int. J. Ser. II, 33, p. 555.

Ueda, T., Enomota, T., and Kanetsuki, M., 1979. Heat transfer characteristics and dynamic behavior of saturated droplets impinging on a heated vertical surface. Bulletin of the JSME, 22, pp. 724 -732.

Wachters, L.H.J. and Westerling, N.A.J., 1966. The heat transfer from a hot wall to impinging water drops in the spheroidal state. Chem. Eng. Sci., 21, pp. 1047-1056.

Wall, T.F., Subramanian, V., and Howley, P., 1982. An experimental study of the geometry, mixing and entrainment of particle laden jets up to 10 diameters from the nozzle. Trans. Chem. Eng., 60, pp. 231-239.

Wang, A.B., Lin, C.H., and Chen, C.C., 2000. The critical temperature of dry impact for tiny droplet impinging on a heated surface, Physics of Fluids, 12, pp. 1622-1625.

Wang, C.H., Sun, C.J. and Kuo, H.C., 1997. An experimental investigation of heat transfer of a droplet impinging upon a hot surface. Int. Comm. Heat and Mass Transfer, 24(1), pp. 65-78.

Warsito, W. and Fan, L.-S., 2001b. Neural network based multi-criteria optimization image reconstruction technique for imaging two- and three-phase flow systems using electrical capacitance tomography. Instrumentation Technique, submitted.

Wiesendorf, V. and Werther, J., 2000. Capacitance probes for solid volume concentration and velocity measurements in industrial fluidized bed reactors. Powder Technology, 110, pp. 143-157.

Wu, P.K., Kirkendall, K.A., and Fuller, R.P., 1998. Particle effects on free jet entrainment. J. Propulsion and Power, 14, pp. 173-182.

Xiong, T.Y., and Yuen, M.C., 1991. Evaporation of a liquid droplet on a hot plate. Int. J. Heat Mass Transfer, 34, pp. 1881-1894.

Yang Y., Arastoopour, H., and Hariri, M.H., 1993. Agglomeration of polyolefin particles in a fluidized bed with a central jet, Part2- Theory. Powder Technology, 74, pp. 239-247.

Yao, S.C. and Cai, K.Y., 1988. The dynamics and Leidenfrost temperature of drops impacting on a hot surface at small angles. Exp. Therm. Fluid Sci. 1, pp. 363-371.

Yao, S.C., Hochreiter, L.E., and Cai, K.Y., 1988. Dynamics of droplets impacting on thin heated strips. J. Heat Transfer, 110, pp. 214-220.

Zavadsky, V.A., 1982. Study of motion of a single solid particle with variable mass in a frame of sprayed liquid. In Teplo- I Massoperenos v Dispersnyh Sistemah, pp. 136-149.

Zhu, C., 2000. Wet rotating granular filter for fine particulate filtration. Progress report to NJCST-PPRC.

Zhu, C., Slaughter, M.C., and Soo, S.L., 1991. Measurement of velocity of particles in a dense suspension by cross correlation of dual laser beams. Review of Scientific Instruments, 62, p. 2036.

Zhu, C., Wang, X., and Fan, L.-S, 2000. Effect of solids concentration on evaporative liquid jets in gas-solid flows. Powder Technology, 111, p. 79.

Zhu, C., Liu, G., Wang, X., and Fan, L.-S., 2001. A similarity model of evaporating liquid spray jets in concurrent gas-solid flows. Powder Technl., 119, pp. 292-297.

Zhu, C., Liu, G., Wang, X., and Fan, L.-S., 2002. A parametric model for evaporating liquid jets in gas-solid flows. Int. J. Multiphase Flow, 28, pp. 1479-1495.

Zuev Yu. V., and Lepeshinskii, I.A., 1995. Two-phase multicomponent turbulent jet with phase transitions. Fluid Dynmics, 30, pp. 750-757.